POLITECNICO
MILANO 1863

SCUOLA DI INGEGNERIA INDUSTRIALE
E DELL'INFORMAZIONE

High-Speed Label-Free 3D Biomedical Imaging through Multiphoton and Broadband CARS Microscopy

Tesi di Laurea Magistrale in
Physics Engineering - Ingegneria Fisica

Author: **Matteo Mandelli**

Student ID: 975935
Advisor: Prof. Dario Polli
Co-advisors: Federico Vernuccio Ph.D.
Academic Year: 2022-23

Abstract

Label-free vibrational imaging techniques play a crucial role in generating detailed chemical maps of cells and tissues, with Spontaneous Raman (SR) standing as the benchmark method due to its chemical specificity. However, it suffers from a low scattering cross-section that hampers imaging speed, hence the need for Coherent Raman Scattering techniques (CRS) like Coherent Anti-Stokes Raman Scattering (CARS). CARS overcome the limitations of SR by exploiting the third-order non-linear optical response of the sample.

Narrowband CARS is its simplest implementation it employs a pair of narrowband pulses to probe a single vibrational mode at a time. A vibrational mode is coherently excited when the frequency difference between the two beams matches the mode resonance frequency. A second interaction with the pump then probes the vibrational mode generating a stronger anti-Stokes signal compared to SR. However, this configuration reveals only one vibrational mode at a time instead of multiple modes as SR does. Broadband CARS (BCARS) addresses this limitation by combining the acquisition speed of single-frequency CARS with the chemical specificity of SR. Indeed it combines narrowband pump pulses with broadband Stokes pulses that allow the excitation and probing of broader vibrational spectrum.

This thesis presents and improves an innovative BCARS setup converting it into a versatile multimodal microscope and proving its capabilities. Chapter 1 introduces the theory behind the CARS and B-CARS processes. Chapter 2 meticulously describes the BCARS setup, discussing its evolution into a multimodal microscope. Chapter 3 focuses on the acquisition and post-processing pipeline for CARS spectroscopy and imaging. Chapter 4 presents the experimental outcomes, including the analysis of standardized samples, 3D sectioning of spheroids, imaging of tumoral breast tissue and resonant response of crystals. It also discusses the use of second harmonic generation (SHG) and three-photon excited fluorescence (3PEF) in conjunction with CARS. These experiments highlight the incredible potential of BCARS microspectroscopy as a standalone technique and even more in a multimodal microscope.

Keywords: Broadband CARS, microscopy,3D sectioning, spectroscopy, High-speed imag-

ing, Multichannel colocalized detection, Post-processing algorithms.

Abstract in lingua italiana

Le tecniche di imaging vibrazionale label-free sono cruciali per la generazione di mappe chimiche di cellule e tessuti e il Raman Sponaneo (SR) si pone come metodo di riferimento grazie alla sua specificità chimica. Tuttavia la ridotta sezione d'urto di scattering ne limita la velocità di imaging, da qui la necessità di tecniche di Scattering Raman Coerente (CRS) come il Coherent Anti-Stokes Raman Scattering (CARS). Il CARS supera le limitazioni del SR sfruttando la risposta ottica non lineare di terzo ordine del campione.

Il CARS narrowband è la più semplice implementazione di questa tecnica, sfrutta una coppia di impulsi narrowband per misurare un singolo modo vibrazionale. Un modo vibrazionale viene eccitato coerentemente quando la differenza di frequenza tra i due fasci combacia con la frequenza vibrazinale del modo. Successivamente una seconda interazione con la pompa sonda il modo vibrazionale generando un segnale anti-Stokes più forte rispetto al SR. Tuttavia, questa configurazione rivela solo un modo vibrazinale alla volta.

Broadband CARS (BCARS) affronta questa limitazione combinando la velocità di acquisizione del CARS a singola frequenza con la specificità chimica del SR. Infatti combina impulsi di pompa a banda stretta con impulsi Stokes a banda larga che consentono di eccitare e misurare uno spettro vibrazionale più ampio.

Questa tesi presenta e migliora un setup BCARS trasformandolo in un versatile microscopio multimodale. Il Capitolo 1 introduce la teoria relativa a CARS e B-CARS. Il Capitolo 2 descrive il setup e la sua evoluzione. Il Capitolo 3 si concentra sulla processo di acquisizione e elaborazione dati. Il Capitolo 4 presenta i risultati sperimentali, tra cui l'analisi dei campioni standardizzati, is sezionamento in 3D di sferoidi, l'imaging di tessuto tumorale mammario e la risposta risonante nei cristalli. Discute anche l'uso della generazione di secondo armonica (SHG) e della fluorescenza a tre fotoni (3PEF) in concomitanza con il CARS utilizzando il canale di acquisizione aggiunto. Questi esperimenti mostrano potenziale della microscopia BCARS come tecnica assestante e ancor di più insieme a altri strumenti in un microsopio multimodale.

Parole chiave: Broadband CARS, Microscopia, Sezionamento 3D, Spettroscopia, Acquisizione immagini a alta velocita, Acquisizione multi-canale colocalizzata, Algoritmi di

elaborazione dati

Contents

1 | Introduction

The most common and affirmed tool for Biomedical Imaging is Optical microscopy as it can achieve resolutions up to the sub-micrometre scale [1]. Among the different optical microscopy techniques, fluorescence microscopy and vibrational microscopy are the common ones that also provide chemical information.

Fluorescence microscopy is well-known and widely adopted due to its incredible sensitivity and the variety of fluorescent markets developed by biologists over the years. These markers can be divided into two categories: endogenous (e.g. fluorescent proteins)when naturally present in the sample [2] or exogenous (e.g. dyes or semiconductor quantum dots) [3] when added externally. However endogenous markers are finite and are not enough to fully study cells and tissues, and exogenous markers may lead to sample perturbation. Another limitation to deal with when working with fluorescent markers is the number of times a given area of the sample can be imaged due to photobleaching or the limited amount of markers "colours" we can distinguish at once. Indeed, since fluorescent proteins have broad emission spectra their signals start to overlap soon when trying to distinguish too many structures [4–6]. These are the reasons why the other common technique to retrieve chemical information from biological samples is vibrational microscopy, which is a label-free technique.

Vibrational [7] microscopy indeed is a technique whose strength is its non-invasiveness thanks to its label-free nature. Indeed, instead of using markers, it analyzes the characteristic vibration spectrum of biomolecules. Note also that all molecules in a biological sample have a unique vibrational spectrum that allows its identification, therefore this technique has also higher chemical specificity compared to the use of markers.
One approach to vibrational microscopy is vibrational absorption microscopy [7] which measures the absorption or reflection of mid-infrared (MIR) light coming from a sample to generate an image and retrieve the sample chemical composition. However, this technique has limited spatial resolution due to the wavelengths used, and limited penetration depth due to water absorption. These issues make this technique not suitable for imaging small features of biological samples.

Raman microscopy instead uses near-infrared (NIR) light which overcomes these limitations. It has a much deeper penetration depth and higher spatial resolution making it an ideal technique for biological applications, such as imaging cells and tissues [8, 9]. The most straightforward and commonly used method in this field is referred to as Spontaneous Raman (SR) [9]. SR utilizes a quasi-monochromatic visible or Near Infrared (NIR) pump laser beam with frequency ω_p. The vibrational information is encoded in the spontaneously emitted inelastically scattered Stokes or anti-Stokes components, with frequencies $\omega_S = \omega_p - \Omega$ and $\omega_{aS} = \omega_p + \Omega$, respectively. With, Ω representing the vibrational resonance of the sample.
These components can be found in the red-shifted spectral region (for the Stokes) and blue-shifted spectral region (for the anti-Stokes), and can be conveniently collected using a spectrometer after the pump radiation has been adequately filtered out.
In the context of life sciences applications, SR techniques typically capture the Stokes component, which is more intense than the anti-Stokes component at room temperature. Due to its chemical specificity, there are already plenty of applications where SR is used in the biomedical field, and especially for cancer diagnosis [10, 11]. However, despite offering extensive chemical information about the investigated sample, SR is not the ideal technique for tasks like imaging where fast acquisition speeds are mandatory. Indeed, since it suffers from a low scattering cross-section, it requires long integration times(ranging from approximately 100 ms to 1 s)for the acquisition of a single-pixel vibrational spectrum, precluding the possibility of rapid imaging.

The limitations of Spontaneous Raman (SR) can be overcome with Coherent Raman Scattering (CRS) techniques [12, 13], which are a form of third-order nonlinear optical microscopy. CRS uses light pulses to create and detect a vibrational coherence within the molecules in the laser focus.
By using two spatially and temporally synchronized pulses, the pump at frequency ω_p and the Stokes at frequency ω_s, a collective molecular oscillation is induced. This results in all molecules vibrating in phase when the difference between pump and Stokes frequencies matches a characteristic vibrational frequency γ, that is, $\omega_p - \omega_s = \Omega$ [14, 15]. This vibrational coherence significantly enhances the Raman response compared to the incoherent SR process. Furthermore, as a non-linear microscopy technique, CRS generates signal only in the focal volume exhibiting 3D sectioning capabilities without the need for confocal apertures [16]. CRS also maintains the other advantages of NIR label-free techniques mentioned before, such as not needing fluorophores, no photobleaching, no phototoxicity and high penetration depth using NIR light.
The two most commonly employed CRS implementations are stimulated Raman scatter-

ing (SRS) [17–19] and coherent anti-Stokes Raman scattering (CARS) [20–22]. Stimulated Raman Scattering (SRS) measures either the intensity gain of the Stokes beam (referred to as stimulated Raman gain) or the intensity loss of the pump beam (known as stimulated Raman loss). On the other hand, Coherent Anti-Stokes Raman Scattering (CARS) detects the at the anti-Stokes frequency $\omega_{aS} = \omega_p + \Omega$ with intensities up to 6-7 orders of magnitude greater than SR signals.
However, this implementation of CARS (called single-frequency or narrowband CARS) has a major limitation, it is fast compared to SR but it also only probes one vibrational mode at a time so it has limited information content. Broadband CARS instead addresses this issue by combining narrowband pump pulses with broadband Stokes pulses to generate a broadband anti-Stokes component, all while maintaining much higher acquisition speeds compared to SR.

A typical spectrum obtained with these techniques can be divided into three intervals depending on the type of chemical information that can be found in each one, as reported in figure 1.1.
The first region known as fingerprint region goes from 400 to 1800 cm^{-1}. It owes its name from the fact that it is the region with the most amount of relevant peaks, as we can see from the focus on this region in figure 1.1. It contain relevant peaks for the four major biological molecules: lipids, porteins, carbohydrates and nucleic acids. These peaks are usually related to stretching, bending, scissoring motions of $C-N$, $C-H$ and $C-C$ bounds.
The second region instead ows it's name to the lack of significant biological peaks from 1800 to 2700 cm^{-1}.
Finally the third region is the CH-stretching region, it's the region that includes the highest energy vibrational modes and goes from 2700 to 3100 cm^{-1}. The peaks we find here are usually associated with CH, CH_2 and CH_3 symmetric and antisimmetric stretching. Due to the abundance of this kind of oscillators these signals are also stronger and they are also related to relevant biological molecules like lipids, proteins and DNA.

This master's thesis will present broadband CARS from its theory to the experimental used, the data processing pipeline and the experimental results obtained. My contribution in particular focused on transforming the setup into a multimodal microscope and further developing the data processing pipeline.
In the next chapter, chapter 2, I will present the theoretical foundation of spontaneous and coherent Raman scattering focusing on broadband CARS.
Then in Chapter 3, I will describe the experimental setup, focusing on the addition of a photomultiplier tube and data acquisition (DAQ) system necessary for the second chan-

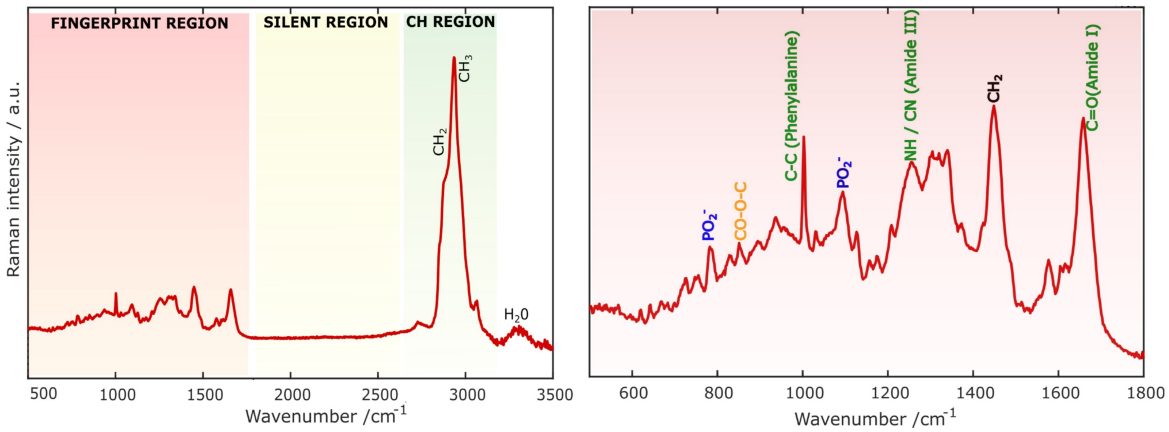

Figure 1.1: Spontaneus Raman spectrum of a cell divided into its three main intervals. Peak assignments refer to the most abundant chemical bonds in biological samples and identify the four major biological molecules: lipids (black), proteins (green), carbohydrates (yellow) and nucleic acids (blue). Adapted from [23]

nel.

In Chapter 4, I will discuss the acquisition and data processing procedure, where the data processing consists of three major steps: calibration, denoising and spectral unmixing. My contribution here mainly revolved around the acquisition, where I added the possibility of creating large stitched images in Brightield, and denoising, where I added white noise removal and directional denoising to the technique already present.

In Chapter 5, I show the experimental results obtained to showcase the capabilities of this setup. Experiments range from test samples to assess the system performance and reliability to more complex measures of biological samples and even spectroscopic measures of crystals.

2 | Theory

2.1. Introduction to Ultrafast Optics

To effectively analyze and understand the processes of Spontaneous and Coherent Raman scattering, as well as specific techniques like broadband CARS, a model to study the interaction between electromagnetic waves and matter must be developed. In particular, we will start with a simple yet powerful model for electromagnetic waves: The harmonic oscillator.

2.1.1. Harmonic Oscillator

The simplest way to describe a molecule interacting with an electromagnetic field is to start by modelling the molecule as a mass attached to a spring characterized by stiffness k, as depicted in figure 2.1. Not only that, but through this picture it is also possible to give an intuitive explanation of Raman Scattering [24].

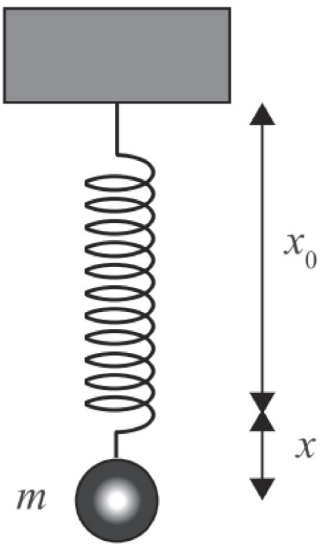

Figure 2.1: mass-spring system with x_0 being the equilibrium position and x the relative displacement. Adapted from [24].

The system described above is a harmonic oscillator, which ideally is an object whose temporal oscillation is a sine wave with constant amplitude and with a frequency that is solely dependent on the system parameters. We consider a mass attached to a spring, set vertically and subjected only to gravity. At equilibrium, we can write the equation describing its centre of mass as follows:

$$mq - kx_0 = 0, \tag{2.1}$$

where x_0 represents the equilibrium position. Using the principle of energy conservation it is possible to study the displacement x of the centre of mass concerning x_0, and the following expression is found:

$$\frac{d^2x}{dt^2} + \omega_0^2 x = 0, \tag{2.2}$$

With $\omega_0 = k/m$ resonant frequency of the system. Now a damping force applied to the mass can be introduced, it will be directly proportional to the mass velocity and to a damping coefficient γ. Adding this term to eq.(2.2) we find:

$$\frac{d^2x}{dt^2} + 2\gamma\frac{dx}{dt} + \omega_0^2 x = 0, \tag{2.3}$$

Then Since we would like to model the interaction with the electromagnetic field, we need to introduce a driving force oscillating periodically. Hence we define $F(t) = F_0 cos(\omega t)$, with the amplitude represented by F_0 and the angular frequency by ω. With the addition of this driving force eq.(2.3) becomes:

$$\frac{d^2x}{dt^2} + 2\gamma\frac{dx}{dt} + \omega_0^2 x = \frac{F(t)}{m}, \tag{2.4}$$

This can be also expressed using the complex exponential notation, where $F(t) = F_0 e^{-i\omega t}$. Therefore, we can simplify the calculus of temporal derivatives by looking at solutions of the form $x(\omega, t) = x(\omega)e^{-i\omega t}$. So plugging this expression in eq. (2.4) we find:

$$(-\omega^2 - 2i\gamma\omega + \omega_0^2 x = \frac{F(t)}{m}, \tag{2.5}$$

And from eq. (2.5) we find the solution $x(\omega)$:

$$x(\omega) = \frac{(F_o/m)}{\omega_0^2 - \omega^2 - 2i\gamma\omega} \tag{2.6}$$

Which is close to resonance and for small damping ($\omega \approx \omega_0$ and $\gamma \ll \omega_0$) the solution of eq. (2.6) will be approximated by a Lorentzian function [24]:

$$x(\omega) = \frac{-F_0/(2m\omega_0)}{(\omega - \omega_0) + i\gamma} \tag{2.7}$$

2.1.2. Vibrational modes

Previously we modelled a simple molecule as a single mass attached to a spring, reducing it to a harmonic oscillator. Doing so we also found the relation which describes the movement of the mass varying the frequency of the driving force. However, the model can be generalized in order to describe all the intramolecular vibrations of a molecule which are called "modes" and are either vibrational or rotational. A vibrational mode can be defined as a periodic motion of the atoms of a molecule relative to each other, with the centre of mass remaining still. Each mode is then characterized by a unique resonant frequency Ω_R, which is dictated by the atomic mass, the atomic species, the number of involved chemical bonds, the molecule geometry and symmetry, and the presence of possible hydrogen bonds. We can also define simple rules to find how many modes a given molecule will sustain. For example, a non-linear molecule formed by n molecules can sustain $3n-6$ modes, while linear ones have $3n-5$ modes. Thus, a diatomic molecule ($n = 2$) has only one normal vibrational mode and a water molecule ($n = 3$) being non-linear has three as reported in figure 2.2.

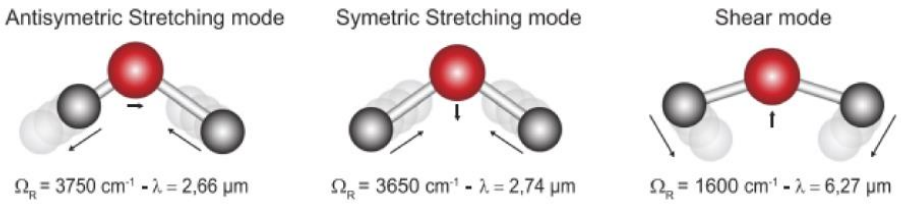

Figure 2.2: Vibrational modes of water with the related wavenumbers. Adapted from [25]

Let's study the simplest case, a diatomic molecule, which can be modelled according to the mass-spring model previously presented as a system made of two point masses, respectively m_1 and m_2 connected by a spring. For this system, we will assume that the equilibrium distance between the point masses is x_0 and the resonant frequency is Ω_R. We will also assume that the diatomic molecule taken into account is polar and presents

an asymmetric distribution of charges, with the atom m_1 presenting a positive charge $+q$ and the atom m_2 a negative charge $-q$. The model is shown in figure 2.3.

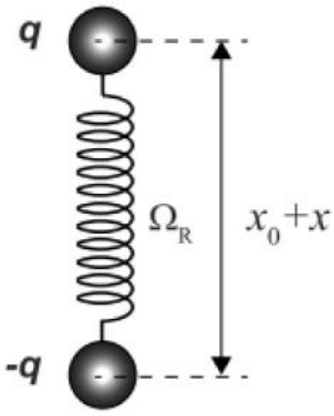

Figure 2.3: Model of a diatomic molecule composed of two charged masses attached to a spring. Adapted from [25]

Let us consider the interaction with an electric field $E(t)$, characterized by an angular frequency ω. The field will generate a Lorentz force $F_{Lorentz} = qE_0e^{-1\omega t}$ on the atoms of the molecule. We can write a formula analogous to (2.4):

$$\frac{d^2x}{dt^2} + 2\gamma\frac{dx}{dt} + \omega_R^2 x = \frac{F_{Lorentz}(t)}{\mu}, \tag{2.8}$$

In which μ is the reduced mass: $\mu = m_1m_2/(m_1 + m_2)$, and where the damping term γ represents the radiation loss of the oscillating dipole. The above equation can be solved as we solved (2.4), finding the approximated solution:

$$x(\omega) = \frac{-F_{Lorentz}/(2\mu\Omega_R)}{(\omega - \Omega_R) + i\gamma} \tag{2.9}$$

The presence of an asymmetric distribution of charges in the molecule induces a dipole moment $\mathbf{p}$, which can be expressed as $\mathbf{p} = q\mathbf{d}$, where $\mathbf{d}$ is the vector displacement between the atoms, directed from the negative to the positive charge. If we consider a macroscopic medium, constituted by an ensemble of N diatomic molecules modelled as above, all subjected to the same electric field $E(t)$, the charge displacement of every molecule will contribute to the total polarization of the medium, which can be calculated as the sum of all the single dipole moments:

$$P(\omega) = Nqx(\omega), \tag{2.10}$$

We can now define the linear electronic susceptibility as:

$$P(\omega) = \epsilon_0 X^{(1)}(\omega) E(\omega), \tag{2.11}$$

So comparing eq. (2.10) with eq. (2.11), and plugging into eq. (2.9) we find the expression of the linear susceptibility $X^{(1)}(\omega)$:

$$X^{(1)}(\omega) = \frac{-(Nq^2)/(2\epsilon_0 \mu \Omega_R)}{(\omega - \Omega_R) + i\gamma} \tag{2.12}$$

This expression describes the vibrational contribution from the molecule to the susceptibility of the medium. Where the real part is related to the medium dispersion, while the imaginary part is related to the medium absorption. Furthermore, the first one has an anti-symmetric distribution with respect to frequency while the second one follows a Lorentian profile centred at the resonant frequency with the width of the Lorentzian peak $\mathcal{F}\{X^{(1)}\}$ directly proportional to the damping constant γ. The real and imaginary parts are schematically represented in figure 2.4

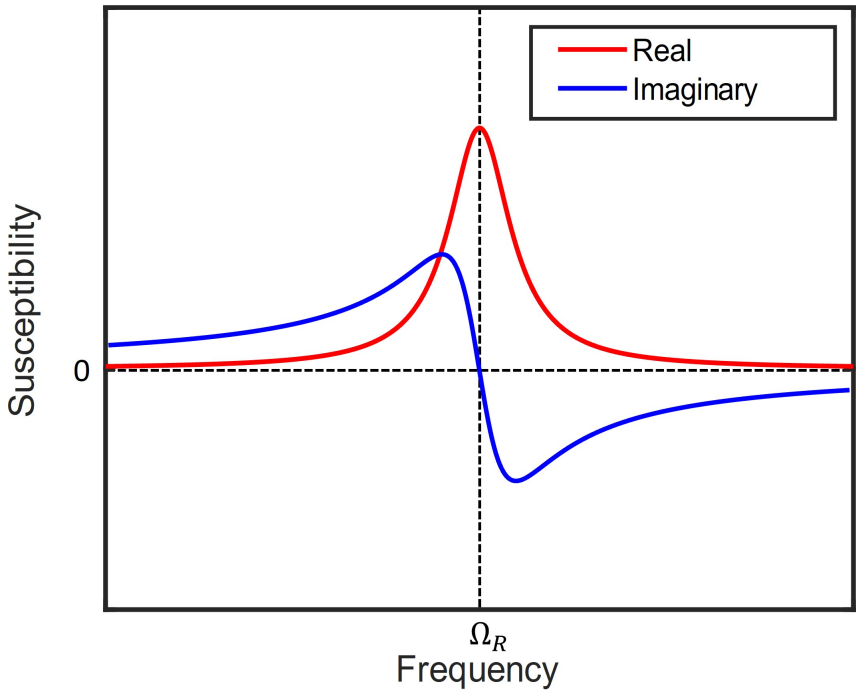

Figure 2.4: Plot of the real and imaginary parts of the linear susceptibility.

We will now limit ourselves to the case of diluted media, where the refractive index can be calculated from the real part of X as follows:

$$n(\omega) = n_0 - \frac{Re[X^{(1)}(\omega]}{2n_0} \tag{2.13}$$

Here n_0 is the mean refractive index of the medium. While the absorption coefficient $\alpha(\omega)$, which instead is linked to the imaginary part of X, can be expressed as:

$$\alpha(\omega) = \frac{2\pi}{\lambda_0 n_0} Im[X^{(1)}(\omega)] \tag{2.14}$$

The absorption coefficent $\alpha(\omega)$, which is expressed in $cm-1$, is also an important parameter in the Lambert-Beer law:

$$I(L) = I_0 exp(-\alpha L), \tag{2.15}$$

This law describes the attenuation of light intensity as it passes through a media of thickness L and it can be exploited to measure the resonance frequencies of vibrational modes and perform spectroscopy of the analyzed medium. The technique is known as infrared (IR) absorption spectroscopy and it enables the identification and quantification of absorption bands associated with various molecular species in a sample. However, IR spectroscopy struggles to achieve high penetration depth or high spatial resolution.

2.1.3. Spontaneous Raman Scattering

To overcome the limitations of IR absorption spectroscopy, SR can be employed to analyze the samples' vibrational modes using visible or NIR quasi-monochromatic laser light, which enables greater penetration depth and spatial resolution. At thermal equilibrium, the interaction between light and matter is primarily driven by absorption (molecules retain the light) and elastic scattering processes, also known as Rayleigh scattering (the light changes direction while maintaining the same frequency). However, a smaller portion of incident light may undergo inelastic scattering, which results in a shift to different frequencies. This phenomenon is referred to as the "Raman effect".

The Raman effect is composed of two main phenomena: Stokes Raman scattering and Anti-Stokes Raman scattering. In the first, the light is scattered at a red-shifted frequency with respect to the impinging one, while in the latter the scattered light is at a blue-shifted frequency. These processes are depicted in Figure 2.6.

To further understand this phenomenon we can consider the diatomic molecule introduced before, which is not necessarily polar this time, but its polarizability α depends on

the intramolecular distance x. This distance fluctuates at the resonant molecular bond frequency Ω_R with $x(t) = x_f cos(\Omega_R t)$, where x_f is the amplitude of the fluctuation. For displacements small enough, it is possible to perform a Taylor expansion of the polarizability $\alpha(t)$ near its initial value

$$\alpha(t) = \alpha_0 + (\frac{\partial \alpha}{\partial x}_0 x(t)), \tag{2.16}$$

The dipole moment induced by an electric field oscillating at ω_p, $E(t) = E_0 cos(\omega_p t)$, can be calculated as:

$$p = \epsilon_0 \alpha(t) E(t), \tag{2.17}$$

let us now plug the expression of the polarizability (2.17) in (2.16):

$$p = \epsilon_0 \left[\alpha + \left(\frac{\partial \alpha}{\partial x}\right) x_f cos(\Omega_R t)\right] E_0 cos(\omega_p t), \tag{2.18}$$

We can proceed with the calculation from (2.18) finding:

$$p = \epsilon_0 \alpha_0 E_0 cos(\omega_p t) + \frac{\epsilon_0 \left(\frac{\partial \alpha}{\partial x}\right)_0 E_0 x_f}{2} cos[(\omega_p - \Omega_R)t] + \frac{\epsilon_0 \left(\frac{\partial \alpha}{\partial x}\right)_0 E_0 x_f}{2} cos[(\omega_p + \Omega_R)t], \tag{2.19}$$

Further analyzing this last equation we can see three major terms.

- The first describes Rayleigh scattering and oscillates at the same frequency as the incoming field. In this case, photons are simply scattered by the molecule without any energy exchange.
- The second is oscillating at angular frequency $\omega_S - \omega_P = \Omega_R$ and describes a red-shifted scattering known as Raman Stokes scattering. In this case, the molecule absorbs part of the energy of the light and is promoted from a ground state to a vibrationally excited state. The emitted photons in this case present a lower energy with respect to the incoming ones.
- The third term represents the Raman anti-Stokes scattering and oscillates at $\omega_{AS} = \omega_P + \Omega_R$. In this case, the molecule goes from the excited state to the ground one, releasing energy. The emitted photons have higher energy with respect to the

incoming ones, and indeed they are blue-shifted in frequency.

These types of scattering are schematically represented in Figure 2.5 through their Jablonsky diagrams.

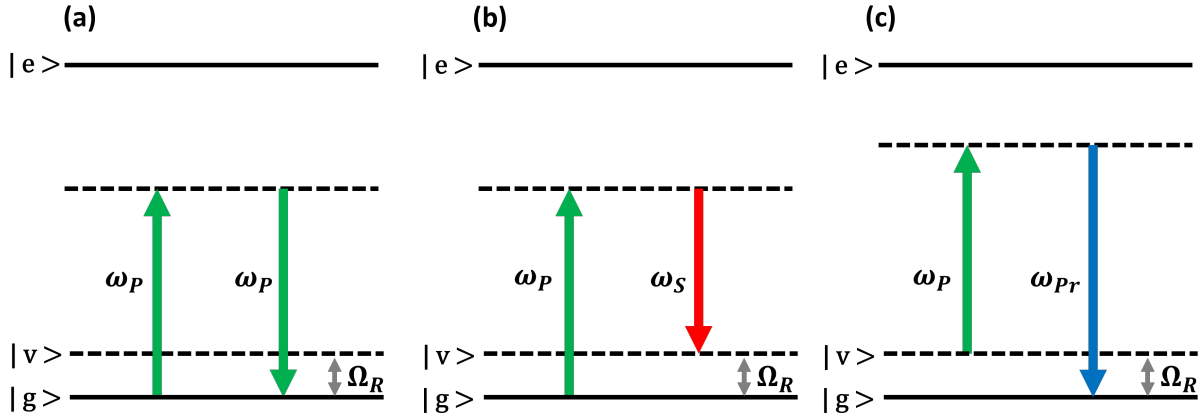

Figure 2.5: Jablonsky diagrams of (a) Rayleigh scattering, (b) Stokes Raman scattering, (c) anti-Stokes Raman scattering. Solid lines represent the fundamental or ground state $|g\rangle$, the vibrational state $|v\rangle$, and the excited state $|e\rangle$, while the dashed line is a virtual state. $|g\rangle$ and $|v\rangle$ are separated by the resonance frequency Ω_R.

Most SR spectroscopy experiments detect the Raman Stokes component as the anti-Stokes scattered intensity is lower compared to the Stokes one. Indeed, at thermal equilibrium, atomic level populations are described by the Boltzmann distribution (2.20). This distribution gives the probability of a system being in the i-th state, depending on the energy of the level ϵ_i the number of particles and the system's temperature.

$$p_i \propto e^{-\epsilon_i/kT} \tag{2.20}$$

Therefore, the population of the excited level is lower than the one at the ground state, and they become equal at infinite temperatures. Therefore, anti-Stokes scattering will produce a smaller signal with respect to Stokes scattering since it requires the molecule to be in the exited state instead of the ground state. For the same reason only at high temperatures the two signals can become comparable.

Besides the strength of the signal, not all vibrational modes are Raman active. Indeed, in order to be Raman active, a vibrational mode has to affect the polarizability, thus the selection rule is the following: $\left(\frac{\partial \alpha}{\partial x}\right)_0 \neq 0$.

Similar to IR absorption spectroscopy, Raman spectroscopy allows us to identify the vibrational levels and measure their energy by analysing the spectral distance of the Raman peaks with respect to the Rayleigh scattering peak, as shown in the figure 2.6.

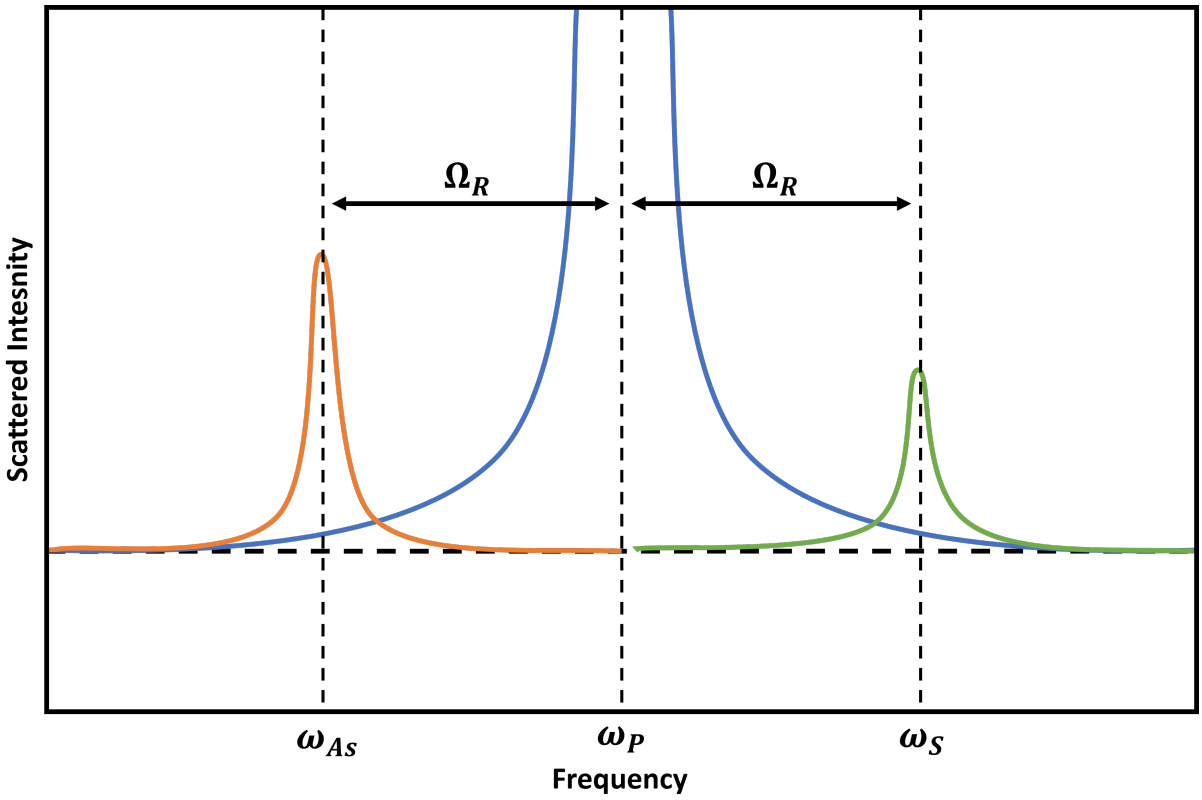

Figure 2.6: Scattered light from a molecule with a single vibrational mode at frequency Ω_R. The Stokes, Rayleigh and anti-Stokes scattering can be seen from the left to the right.

If a molecule presents inversion symmetry, its modes can be either Raman active and not IR active or vice-versa. In particular, symmetric modes with respect to the inversion symmetry are only Raman active, while anti-symmetric ones are only IR active. The main advantage of Raman spectroscopy with respect to IR absorption spectroscopy is that the former allows to reach sub-micron resolution since shorter wavelengths can be used to excite Raman scattering. However, a major limitation is the cross-section of Raman scattering which is rather small: the order of magnitude is around $10 - 30cm^2$.

2.1.4. Coherent Raman Scattering

In the previous section, we understood that the main limitation of Spontaneous Raman spectroscopy is the relatively small cross-section. Therefore, the acquisition of a vibrational spectrum requires a considerable amount of time to achieve an acceptable

signal-to-noise ratio.

Instead Coherent Raman Scattering (CRS) allows us to overcome this problem, with an efficiency factor of 10^7 compared to spontaneous Raman scattering.

The better efficiency that CRS provides allows for higher imaging speed than SR thanks to the nonlinear nature of the processes involved during the interaction of the electric fields and the sample. In this section, we will describe the physics behind CRS processes and then focus on CARS and SRS processes.

We start considering the composite field resulting from the interaction of two waves, pump and stokes, with frequency ω_P and ω_S respectively:

$$E(z,t) = A_P e^{i(\omega_P t - k_P z)} + A_S e^{i(\omega_S t - k_S z)} + \text{c.c.}, \tag{2.21}$$

A beating frequency is generated from the interference between the two fields at $\Omega = \omega_P - \omega_S$. If this beating frequency Ω matches the frequency of a vibrational mode, $\Omega_R = \Omega$, then the normal mode enters in resonance with the wave beating.

We will now go back to the harmonic oscillator model for the diatomic molecule. In this case the energy W necessary to create a dipolar moment $\mathbf{p}(t) = \epsilon_0 \alpha(t)\mathbf{E}(t)$ can be written as:

$$W = \frac{1}{2}\langle \mathbf{p}(z,t) \cdot \mathbf{E}(t) \rangle = \frac{1}{2}\epsilon_0 \alpha(t) \langle E^2(z,t) \rangle \tag{2.22}$$

Where $\langle\rangle$ represents the time average over one optical period. We can now calculate the excitation force as the derivative of the energy with respect to the intermolecular distance as follows:

$$F(t) = \frac{dW}{dx} = \epsilon_0 \frac{\partial \alpha}{\partial x}_0 A_P A_S^* e^{i(\Omega t - Kz)} + \text{c.c.} \tag{2.23}$$

Let us plug this equation into the expression of the driven harmonic oscillator (**??**) and look for a solution of the form:

$$x(z,t) = x(\Omega) e^{i(\Omega t - Kz)} + \text{c.c.} \tag{2.24}$$

Close to resonance, the molecular vibration amplitude will be:

$$x(\Omega) = \frac{-(\frac{\epsilon_0}{2\mu\Omega_R})(\frac{\partial\alpha}{\partial x}_0)A_P A_S^*}{(\Omega - \Omega_R) + i\gamma} \tag{2.25}$$

Therefore, if the beating frequency Ω gets close to the resonance frequency Ω_R, the vibration amplitude of the molecule $x(\Omega)$ get amplified, inducing non-linear polarization specific to the molecular resonance.

Let us now calculate the induced polarization as the sum of the induced dipole moments in the medium:

$$P(z,t) = Np(z,t) = N\epsilon_0 \left[\alpha_0 + \frac{\partial\alpha}{\partial x}_0 x(z,t)\right] E(z,t) \tag{2.26}$$

We can distinguish two terms from (2.26):

- The linear polarization $P^{(L)}$, oscillating at the same frequency of the electric field and directly proportional to it: $P^{(L)} = N\epsilon_0\alpha_0 E(z,t)$
- The non-linear polarization:
  $P^{(NL)} = P(\omega_{as})e^{-i\omega_{as}t} + P(\omega_{cs})e^{-i\omega_{cs}t} + P(\omega_p)e^{-i\omega_p t} + P(\omega_s)e^{-i\omega_s t} + \text{c.c.}$ where $\omega_{as} = 2\omega_p - \omega_s = 2\omega_s - \omega_p$.

The non-linear term is particularly relevant as it is the sum of four terms associated with different processes. In particular, the terms $P(\omega_{as})$ and $P(\omega_{cs})$ are used in Coherent anti-stokes Raman scattering (CARS) and Coherent Stokes Raman Scattering (CSRS) respectively. Instead, the terms $P(\omega_p)$ and $P(\omega_s)$ are used for Stimulated Raman scattering (SRS). However, note that CSRS is not considered when dealing with CRS techniques since ω_{cs} is in the IR where most of the detectors are noisy and have lower quantum efficiency.

Here are the expressions of each polarization term individually:

$$\begin{aligned}
P(\omega_{as}) &= N\epsilon_0 \frac{\partial\alpha}{\partial x} x(\Omega) A_p e^{i(2k_p - k_s)z} \\
P(\omega_{cs}) &= N\epsilon_0 \frac{\partial\alpha}{\partial x} x(\Omega) A_s e^{i(2k_s - k_p)z} \\
P(\omega_p) &= N\epsilon_0 \frac{\partial\alpha}{\partial x} x(\Omega) A_s e^{ik_p z} \\
P(\omega_s) &= N\epsilon_0 \frac{\partial\alpha}{\partial x} x(\Omega) A_p e^{ik_s z}
\end{aligned} \tag{2.27}$$

These expressions of the polarization suggest that CRS processes arise from the third-

order nonlinear optical interaction since the interaction among three electric fields is required to give rise to the nonlinear signal. Therefore, CRS processes are four-wave mixing phenomena mediated by the third-order nonlinear susceptibility of the medium $\chi^{(3)}$.

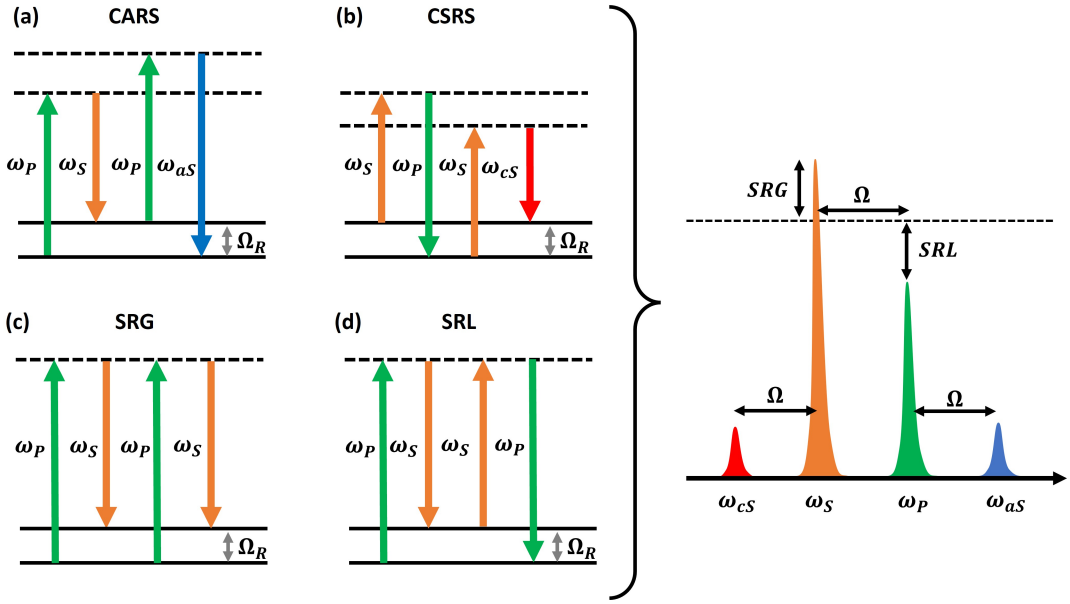

Figure 2.7: (a) Input Stokes and pump pulses in CRS processes. Jablonsky diagrams of (b) Coherent anti-Stokes Raman scattering (CARS), (c) Coherent Stokes Raman scattering (CSRS), (d) Stimulated Raman Gain (SRG). (e) Stimulated Raman Loss (SRL). (f) Output fields and generated signals (not in scale).

2.1.5. Third order non-linear optical processes

In order to describe third-order nonlinear optical phenomena, third-order polarization should be taken into account. It can be written as:

$$P_i^{(3)}(t) = \epsilon_0 \int_{-\infty}^{+\infty} dt' \int_{-\infty}^{+\infty} dt'' \int_{-\infty}^{+\infty} dt''' \chi_{ijkl}^{(3)}(t', t'', t''') \\ E_j(t-t')E_k(t-t'-t'')E_l(t-t'-t''-t''') \tag{2.28}$$

We can simplify the equation above with a few approximations obtaining:

$$P^{(3)} = \epsilon_0 \chi^{(3)} E^3(t) \tag{2.29}$$

Let us now introduce an incoming electric field defined as:

$$E(t) = A_1 \cos(\omega_1 t + \phi_1) + A_2 \cos(\omega_2 t + \phi_2) + A_3 \cos(\omega_3 t + \phi_3) \tag{2.30}$$

The third-order non-linear polarization could be calculated by substituting this last equation in (2.29), finding:

$$P^{(3)} = \epsilon_0 \chi^{(3)} [A_1 \cos(\omega_1 t + \phi_1) + A_2 \cos(\omega_2 t + \phi_2) + A_3 \cos(\omega_3 t + \phi_3)]^3 \tag{2.31}$$

Performing the calculations, we find 22 different terms oscillating at different frequencies. These polarization terms act as new sources giving rise to radiation at the same frequency. The 22 terms can be classified in the following way:

- 3 terms at the original frequencies ω_1, ω_2 and ω_3, which give rise to the Optical Kerr effect (self-phase modulation and self-focusing)
- 3 terms at the third harmonics $3\omega_1$, $3\omega_2$ and $3\omega_3$, which is called Third Harmonic Generation (THG),
- 6 terms at $2\omega_i + \omega_j$, with $i \neq j$,
- 6 terms at $2\omega_i - \omega_j$, with $i \neq j$,
- 1 term at $\omega_1 + \omega_2 + \omega_3$,
- 3 terms at $\omega_i + \omega_j - \omega_k$, with $i \neq j \neq k$,

Therefore, a wave at a different frequency is obtained as an output. The whole process could be seen as an interaction among four waves 2.8. For this reason, third-order phenomena are also called Four Wave Mixing (FWM) processes [26].

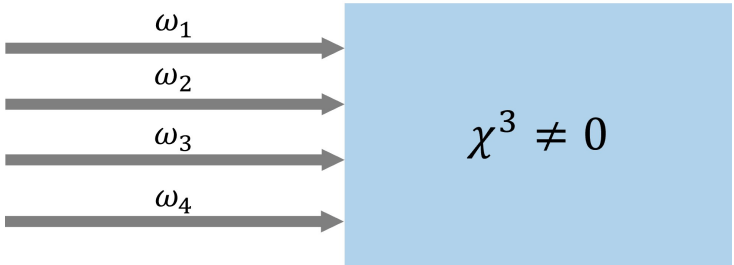

Figure 2.8: Conceptual scheme of the interaction between light and matter for third-order non-linear optical phenomena.

2.1.6. Four-Wave Mixing

Starting from Maxwell equations and considering the propagation in nonlinear optical media, it is possible to derive, under the slowly varying envelope approximation and the plane wave approximation, the envelope propagation equation for short laser pulses in nonlinear media that, if we neglect the dispersions, reads:

$$\frac{\partial A}{\partial z} + \frac{1}{v_g(\omega_0)}\frac{\partial A}{\partial t} = -\frac{i\mu_0\omega_0 c}{2n(\omega_0)}e^{-i\Delta k z}B \tag{2.32}$$

where A and B are the envelopes of the electric field and of the nonlinear polarization ($E(z,t) = \Re\{A(z,t)e^{i(\omega_0 t - k_0 z)}\}$ and $P^{(NL)}(z,t) = \Re\{B(z,t)e^{i(\omega_0 t - k_p z)}\}$), v_g is the group velocity and Δk is the wavevector mismatch. We would like to use this equation for the FWM phenomena.

Let us define the incoming electric field in the exponential form:

$$\begin{aligned} E(t,z) = \frac{1}{2}\Big[&A_1(t,z)e^{i(\omega_1 t - k_1 z)} + A_2(t,z)e^{i(\omega_2 t - k_2 z)} \\ &+ A_3(t,z)e^{i(\omega_3 t - k_3 z)} + A_4(t,z)e^{i(\omega_4 t - k_4 z)} + c.c.\Big] \end{aligned} \tag{2.33}$$

where the expression *c.c.* stands for complex conjugate.

Let us now assume $\omega_1 + \omega_3 = \omega_2 + \omega_4$, and let us focus on the terms oscillating at the same frequencies as the incoming waves. Substituting (1.38) in (1.37) we find, after some calculations, that the third order polarization term oscillating at frequency ω_1, namely $P^{(3)}_{\omega_1}$ reads:

$$P^{(3)}_{\omega_1}(t,z) = \epsilon_0\chi^{(3)}\frac{4}{3}A_2(t,z)A_4(t,z)A_3^*(t,z)e^{i[(\omega_2-\omega_3+\omega_4)t-(k_2+k_4-k_3)z]} + c.c. \tag{2.34}$$

The same reasoning could be applied to all the other terms oscillating at the original frequencies, obtaining:

$$\begin{aligned} P^{(3)}_{\omega_1}(t,z) &= \epsilon_0\chi^{(3)}\frac{3}{4}A_2(t,z)A_4(t,z)A_3^*(t,z)e^{i[\omega_1 t-(k_2+k_4-k_3)z]} + c.c. \\ P^{(3)}_{\omega_2}(t,z) &= \epsilon_0\chi^{(3)}\frac{3}{4}A_1(t,z)A_3(t,z)A_4^*(t,z)e^{i[\omega_2 t-(k_1+k_3-k_4)z]} + c.c. \\ P^{(3)}_{\omega_3}(t,z) &= \epsilon_0\chi^{(3)}\frac{3}{4}A_2(t,z)A_4(t,z)A_1^*(t,z)e^{i[\omega_3 t-(k_2+k_4-k_1)z]} + c.c. \\ P^{(3)}_{\omega_4}(t,z) &= \epsilon_0\chi^{(3)}\frac{3}{4}A_1(t,z)A_3(t,z)A_2^*(t,z)e^{i[\omega_4 t-(k_1+k_3-k_2)z]} + c.c. \end{aligned} \tag{2.35}$$

From (2.34), we found that the envelope of $P^{(3)}_{\omega_1}$ can be written as:

$$B(t,z) = \epsilon_0 \chi^{(3)} \frac{3}{4} A_2(t,z) A_4(t,z) A_3^*(t,z) \tag{2.36}$$

We can now plug (2.36) in (2.32) and develop the calculation for the wave at frequency ω_1. Therefore, the propagation equation becomes:

$$\frac{\partial A_1}{\partial z} + \frac{1}{v_g(\omega_1)} \frac{\partial A_1}{\partial t} = -i \frac{3\omega_1 \chi^{(3)}}{8cn(\omega_1)} A_2 A_4 A_3^* e^{-i(k_2+k_4-k_3-k_1)z} \tag{2.37}$$

Let us define $k_p \equiv k_2 + k_4 - k_3$, and $\Delta k = k_1 - k_p$. We can proceed by rewriting the equation above as:

$$\frac{\partial A_1}{\partial z} + \frac{1}{v_g(\omega_1)} \frac{\partial A_1}{\partial t} = -i f_1 A_2 A_4 A_3^* e^{i\Delta k z} \tag{2.38}$$

where we exploited the relation $\epsilon_0 \mu_0 = \frac{1}{c^2}$. Plugging the envelope of the polarization written in (2.35) and proceeding with analogous calculation we find:

$$\begin{aligned}
\frac{\partial A_1}{\partial z} + \frac{1}{v_g(\omega_1)} \frac{\partial A_1}{\partial t} &= -i f_1 A_2 A_4 A_3^* e^{i\Delta k z} \\
\frac{\partial A_2}{\partial z} + \frac{1}{v_g(\omega_2)} \frac{\partial A_2}{\partial t} &= -i f_2 A_1 A_3 A_4^* e^{-i\Delta k z} \\
\frac{\partial A_3}{\partial z} + \frac{1}{v_g(\omega_3)} \frac{\partial A_3}{\partial t} &= -i f_3 A_2 A_4 A_1^* e^{i\Delta k z} \\
\frac{\partial A_4}{\partial z} + \frac{1}{v_g(\omega_4)} \frac{\partial A_4}{\partial t} &= -i f_4 A_1 A_3 A_2^* e^{-i\Delta k z}
\end{aligned} \tag{2.39}$$

where we made use of f_i, defined as $f_i \equiv \frac{3\omega_i \chi^{(3)}}{8cn(\omega_i)}$. It is possible to observe that the set of equations above represents the propagation equation for four-wave mixing phenomena (neglecting dispersion for simplicity), which are characterized by the direct dependence on the term $\chi^{(3)}$, which will be analyzed in details in the following sections.

2.2. CARS

At the end of the previous section we introduced the realm of coherent Raman scattering techniques, we will focus now on Coherent Anti-Stoker Raman Scattering (CARS) specifically. It is indeed a powerful technique and the one we will use in our experiments. It uses third-order non-linear processes to excite Raman transitions at frequency $\Omega = \omega_P - \omega_S$, using synchronized pulses at pump ω_P and Stokes ω_S frequencies. When Ω matches the resonance frequency Ω_R of the sample all the molecules in the focal spot will be resonantly excited to a specific vibrational level. Then by using a third beam called probe beam at ω_{Pr}, we can excite the molecules from the vibrational level and measure the anti-Stokes frequency $\omega_{As}$when they relax back emitting photons. So the anti-Stokes frequency will be given by:

$$\omega_{aS} = \omega_P - \omega_S + \omega_{Pr} \tag{2.40}$$

However, often we use the same beam for pump and probe in the so-called degenerate CARS configuration. So $\omega_{Pr} = \omega_P$ and $\omega_{aS} = 2\omega_P - \omega_S$. Note that this configuration is the one depicted in figure 2.9 a).

The expression for the CARS signal can be obtained starting from the four-wave mixing expression (2.39) after a few considerations:

- we will use the continuous wave approximation $\frac{\partial A_i}{\partial t} \approx 0$.
- we impose $\omega_P = \omega_1 = \omega_3, \quad \omega_S = \omega_2, \quad \omega_{aS} = \omega_4$
- we assume small signals, so pump and Stokes envelopes are constant (A_P and A_S are constants)
- we assume not anti-Stokes signal at the sample input ($A_{As}(z = 0) = 0$)

With these considerations, only one equation remains in the four-wave mixing system: $\frac{\partial A_{as}}{\partial z} = -i\alpha_{as}\chi^{(3)}A_P^2A_S^*e^{i\Delta kz}$. The CARS intensity will be proportional to the square modulus of the integral of this last expression, so:

$$I_{CARS} \propto |A_{aS}(z = L)|^2 = -\alpha_{as}^2|\chi^{(3)}|^2I_p^2I_sL^2\text{sinc}^2\left(\frac{\Delta kL}{2}\right) \tag{2.41}$$

where $A_{as}(z = L)$ was obtained by integrating the remaining expression obtained from the four-wave mixing system.

It is worth mentioning a few aspects by looking at equation (2.41):

- The expression represents the intensity of the CARS signal coming out of a medium with width L.
- Since the signal scales quadratically with the pump intensity, but linearly with the Stokes one, it is better to increase the pump to increase the signal.
- The signal also scales quadratically with the width of the medium L, therefore thin samples will inherently produce weaker signals and will be more difficult to deal with.
- Finally the signal scales quadratically with $|\chi^{(3)}|$ which is connected to the number of scatterers.
- To maximise the intensity, besides the other factors mentioned above, the phase matching condition $\Delta k \simeq 0$ should be respected.

Focusing on the last observation, the phase matching condition can be written as: $\Delta k = 2k_P - k_S - k_{AS} \approx 0$ where $k_P = (n_P\omega_P)/c$, $k_S = (n_S\omega_S)/c$ and $k_{As} = (n_{As}\omega_{As})/c$. In general operating conditions tough n_P, n_S and n_{As} are different due to material dispersion. However, in microscopy we are in a situation of tight focusing where ΔKL is approximately zero, therefore the sinc function becomes one and the CARS intensity expression can be written as:

$$I_{CARS} \propto |A_{as}(z = L)|^2 = -\alpha_{as}^2 |\chi^{(3)}|^2 I_p^2 I_s L^2 \tag{2.42}$$

2.2.1. Resonant and Non-Resonant Contribution

The CARS signal we described in the previous section suffers from the presence of a non-resonant background (NRB). In this section, we will distinguish between the resonant and non-resonant parts of the signal in the context of degenerate CARS. As we can see from the Jablonski diagrams presented in figure 2.9 the resonant CARS signal is produced in two steps. In the first, the pump beam excites a molecule to a virtual level and the Stokes beam excites the vibrational coherence. In the second another interaction with the pump (which acts as probe) excites the molecule from the vibrational level to a virtual level from which it relaxes emitting the anti-Stokes signal.
In the non-resonant scenario instead, there is not any vibrational resonance. The molecules just interact twice with the pump beam and then the interaction with the Stokes brings the molecule to a lower virtual state from which it relaxes again emitting the anti-stoke

signal. This second scenario is the result of the immediate electronic response of the medium.

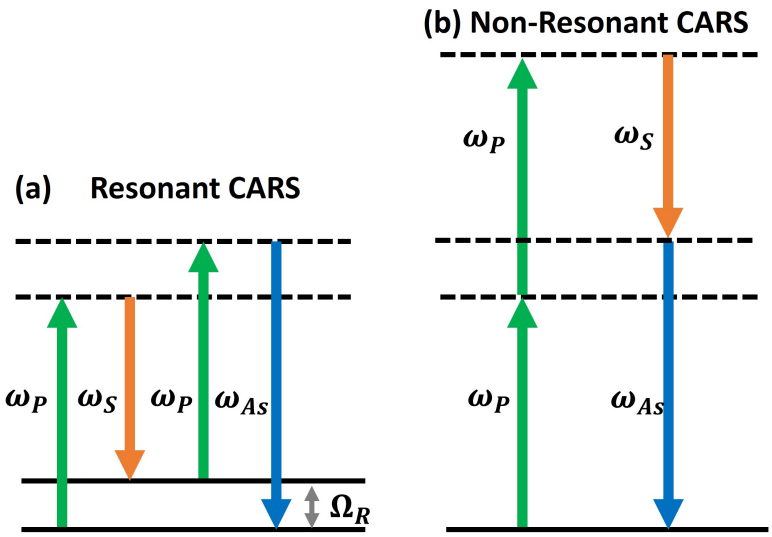

Figure 2.9: Jablonski diagrams of resonant (a) and non-resonant (b) CARS.

The distinction between the two phenomena is also reflected in the expression of the third-order susceptibility:

$$\chi^{(3)} = \chi^{(3)}_{NR} + \chi^{(3)}_{R} \tag{2.43}$$

Where the resonant susceptibility is given only by the molecules which satisfy the resonant condition while the non-resonant susceptibility is given by the whole medium, including the molecules that satisfy the resonant condition.
The resonant susceptibility is a complex number with a Lorentian imaginary part and a dispersive real part, while the non-resonant susceptibility is a a real and constant value, as we can see in figure 2.10.

Let's now focus on the dependence of the CARS intensity from $|\chi^{(3)}|^2$ starting by writing explicitly the resonant and non-resonant contributions:

$$I_{\text{CARS}} \propto |\chi^{(3)}|^2 = |\chi^{(3)}_R + \chi^{(3)}_{NR}|^2 = |\chi^{(3)}_R|^2 + |\chi^{(3)}_{NR}|^2 + 2\chi^{(3)}_{NR}\Re\{n\chi^{(3)}_R\} \tag{2.44}$$

In the equation above we can notice the presence of three contributions:

- The first one is the resonant contribution $|\chi^{(3)}_R|^2$ which contains the vibrational information of the analyzed system. This also means that the CARS signal will

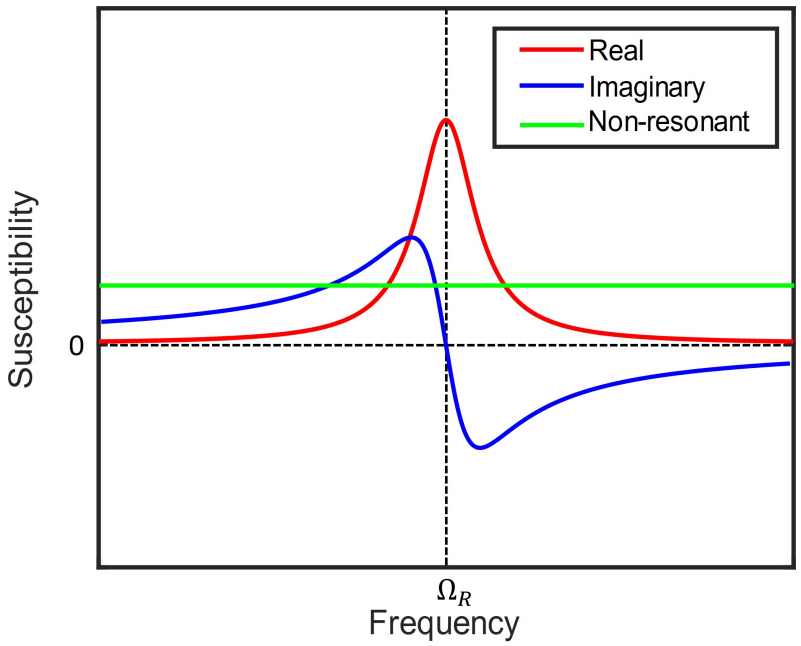

Figure 2.10: Plot representing the resonant susceptibility (real and imaginary parts) alongside the non-resonant susceptibility (which is only real).

exhibit a quadratic dependence on the molecular concentrations, so less abundant species in a sample will be more difficult to detect.

- The second one is the non-resonant contribution $|\chi^{(3)}_{NR}|^2$. This term constitutes a frequency-independent contribution to the signal unless it is close to electronic resonances.
- The third and final term is $2\chi^{(3)}_{NR}\Re\{n\chi^{(3)}_R\}$ which originates from the interference between the two other contributions and gives rise to the dispersive signal distorting the lineshape.

The second and third contributions together create the so-called non-resonant background (NRB). The NRB however is not a completely undesired process as it has a dual effect one harmful and the other useful. The harmful effect is the deformation of the Lorentian shape of the peaks caused by the introduced dispersive component (the third term). However is also useful as it enhances the signal intensity by producing a frequency-independent offset (the second term).

Therefore, since we saw that only the resonant term contains information about the vibrational modes, it is also the only relevant one for spectroscopic applications and it is often required to eliminate the NRB. There are several methods developed in this sense, some optical using polarization CARS [27], time-delayed CARS [28] [29] or Furoier

transform CARS [30] [20]. Other methods instead rely on post-processing using different numerical methods like Time-domain Kramers-Kronig [31] or Maximum-Entropy-Method [32] or even deep learning algorithms [33]. In our experiments, we adopted mainly post-processing with the Kramers-Kronig algorithm, but we also explored time-delay CARS as we will see in the next chapters.

2.2.2. Broadband CARS

In the previous sections, we introduced CARS as a CRS technique that could overcome the limitations of SR in terms of signal-to-noise ratio and acquisition speed. However, we only considered narrowband picosecond pump and Stokes beams. This is called a "single-frequency regime" and it allows for extremely fast acquisition speeds at the cost of limited information content compared to SR. Indeed in this regime, the narrowband pulses allow to probe a single vibrational transition.

Broadband CARS (B-CARS) on the other hand is a trade-off between SR and single frequency CARS, combining fast acquisition speeds with an information content comparable with SR 2.11.

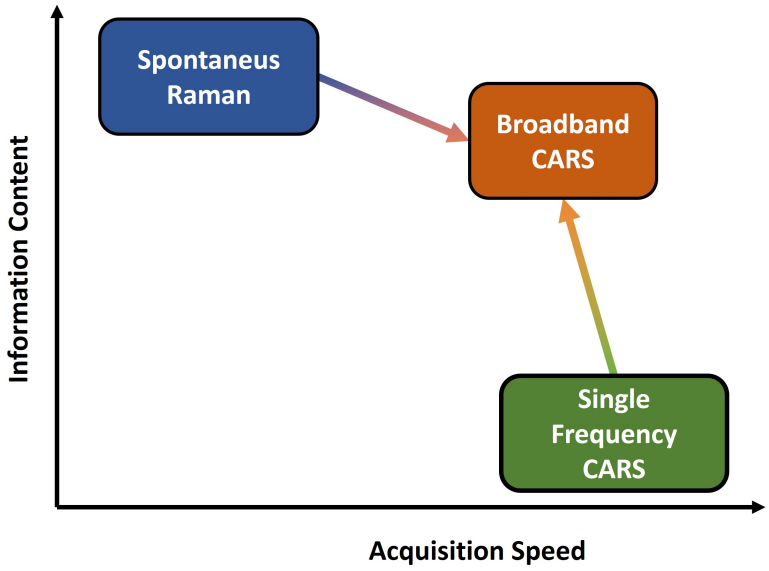

Figure 2.11: Intuitive comparison between spontaneous Raman, single frequency CARS and broadband CARS.

B-CARS however is also a more challenging technique, which requires more sophisticated technical implementations both for generating the necessary optical pulses and for the detection the broadband signal. Depending on how the anti-Stokes spectrum is generated we can distinguish two approaches to implement B-CARS: hyperspectral CARS and

multiplex CARS.

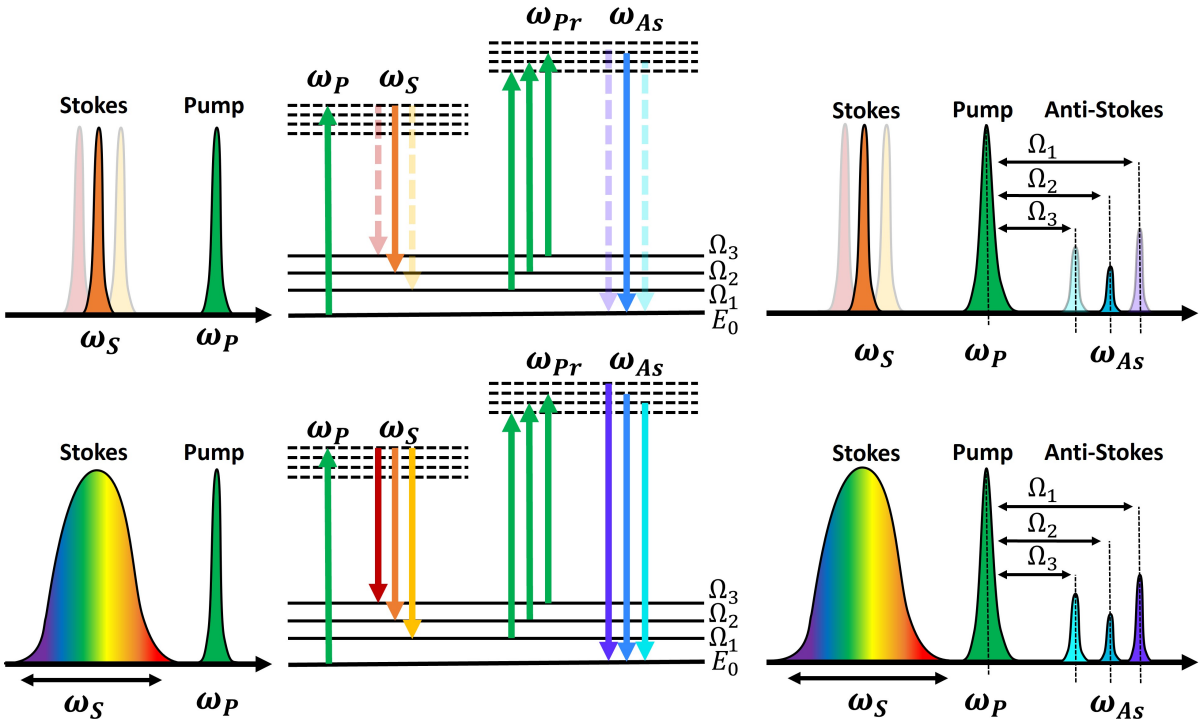

Figure 2.12: Jablonski diagram for hyperspectral CARS (top) and multiplex CARS (bottom).

As we can see from figure 2.12 hyperspectral CARS employs two narrowband picosecond beams, pump and Stokes. The Stokes beam is then rapidly detuned to match the different Raman shifts generating different anti-Stokes components.
Multiplex CARS instead uses a broadband Stokes beam and a narrowband pump beam to generate the anti-Stokes components, this allows probing the different Raman modes simultaneously.

Our experiments employed the multiplex CARS technique. Although there are several implementations of this technique, especially regarding the methods to generate the broadband pulses and detect the CARS spectrum. For the pulse generation some methods use a single ultra-broadband laser to produce both the pump and Stokes frequencies [34] [35], while others obtain the broadband Stokes pulses with supercontinuum generation in a tapered fibre [36] or in photonic crystal fibres (PCF) [37]. Light detection instead can be done using a spectrometer, frequency combs [30] or using a time-domain Fourier transform approach [38] [20].

Our setup in particular generates the broadband Stokes pulses with white light continuum generation in a crystal (YAG or KTP), and the CARS signal obtained overlapping the

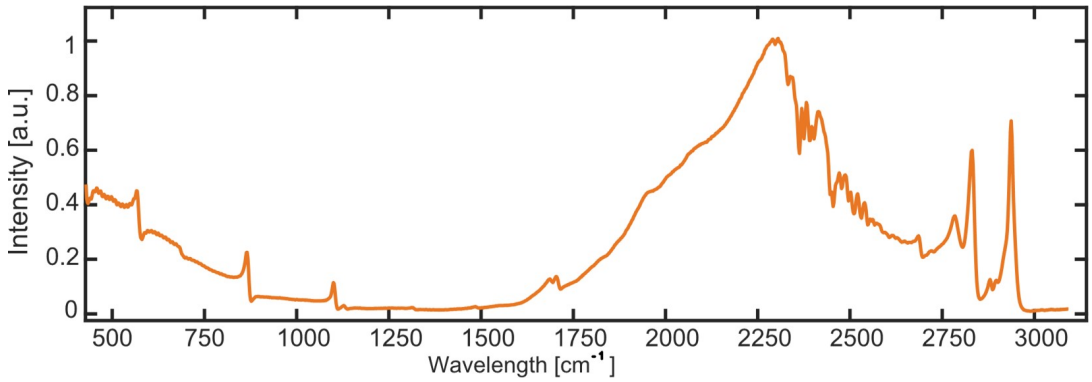

Figure 2.13: Example of experimental B-CARS spectrum obtained from Toluene from $500cm^{-1}$ to $3100cm^{-1}$

narrowband pump with the broadband Stokes is detected with a low-noise high-speed camera for spectroscopy. Note that with this approach several vibrational modes are simultaneously excited obtaining an ultrabroad CARS spectrum covering both the fingerprint and C-H stretching regions as we can see from figure 2.13. it is worth mentioning also that the spectrum obtained will be distorted and amplified by NRB and to retrieve Lorentian peaks it will be necessary to undergo a post-processing procedure that we will treat in the next chapters 4.

2.2.3. 2-Colour and 3-Colour CARS

In the previous section, we introduced different broadband B-CARS techniques focusing on hyperspectral CARS, which was described using its Jablonski diagram in figure 2.12.However, to be more precise B-CARS can be split into two processes depending on the order of interactions with pump and Stokes pulses.
These two processes are called two-colour and three-colour CARS and are represented in figure 2.14.

In the two-colour process, the first interaction occurs with a pump photon which promotes the molecule to a virtual state. Then the same molecule stimulated by the Stokes photon decays reaching a vibrational level. In B-CARS a broadband Stokes pulse is used so multiple levels are reached.
After reaching a virtually excited level another pump photon, acting as the probe, excites the molecule to other virtual levels from which it can finally decay emitting an anti-Stokes photon which constitutes the CARS signal.

In the three-colour process, the first interaction instead is with a Stokes photon acting as the pump. This interaction like before excites the molecule to a virtual level from which

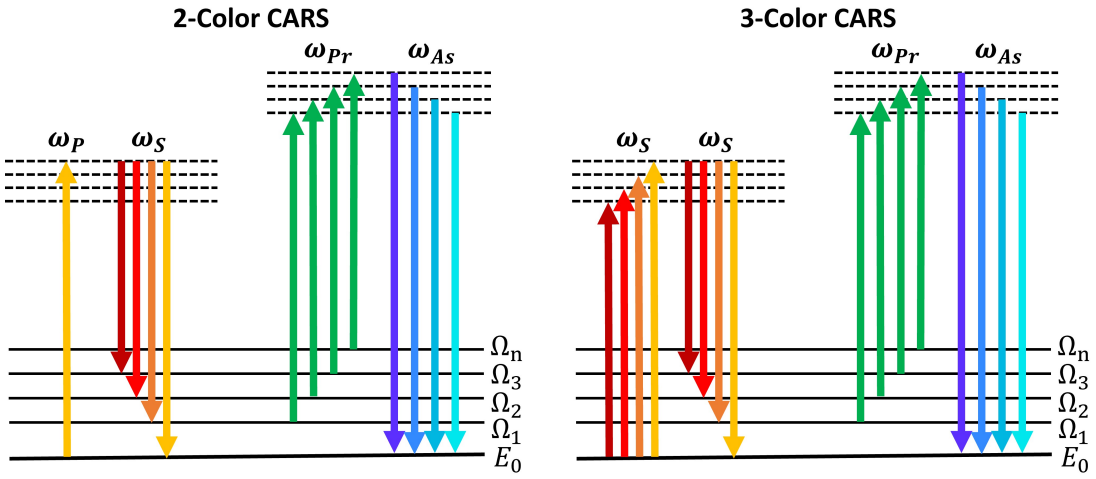

Figure 2.14: Jablonski diagram of two-color and three-color CARS.

it will decay to a vibrational level due to the following interaction with the probe. The rest of the process is similar to what we saw before.

it is important to notice that the source of the first two excitations for three-colour CARS is the same pulse, the Stokes pulse. Therefore for this process to work the Stokes pulse must be broadband and the different colours must arrive almost simultaneously to allow for the two interactions to occurr. This process indeed is called "intra-pulse excitation". Using only one pulse also means that the excitation profile depends on the number of permutations of available frequencies of light, which increases for closely spaced frequencies. Therefore since the excitation profile increases with decreasing wavenumbers [39], this process is ideal to stimulate transitions in the fingerprint region.

2.2.4. Time-Delayed CARS

Time-Delayed CARS (TD-CARS) is a technique that exploits the different origins between resonant and non-resonant CARS signals. Indeed, the coherence generated in the medium by resonant CARS has a duration in the order of picoseconds. Contrarily, the NRB has much shorter lifetimes, with the biggest contribution lasting only as long as the excitation pulse [40].

Therefore thanks to the shorter lifetime of the non-resonant contribution it is possible to isolate it from the resonant one by adjusting the arrival time of the third field, which acts as a probe field 2.15.

Note that only three-color CARS is suitable for this technique. In two-colour CARS indeed, introducing a delay between pump and stokes would not allow to excite the

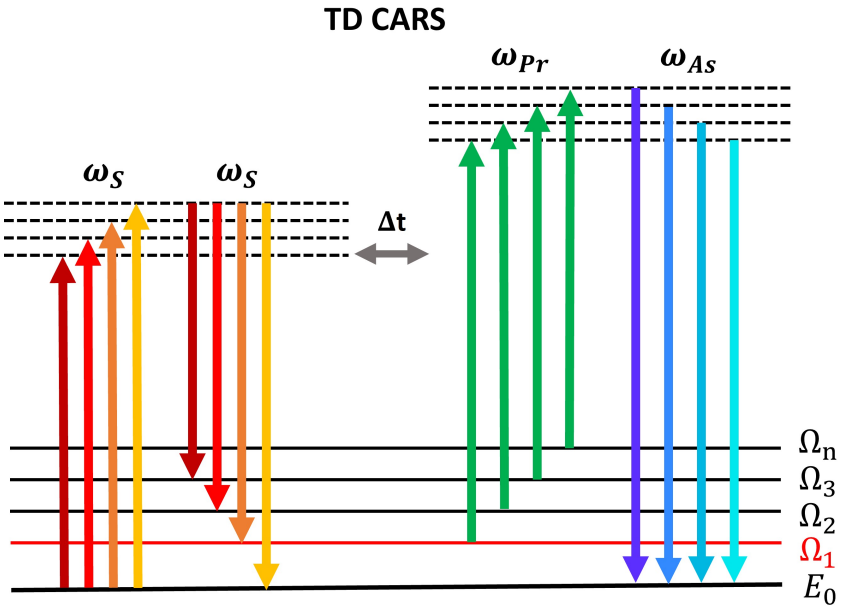

Figure 2.15: Jablonski diagram of TD-CARS. After pump and Stokes beams arrive, the third beam which acts as probe arrives with a delay Δt waiting for the decay of the NRB. If this delay is sufficiently large (more than one pulse duration is enough) to suppress the NRB, the measured anti-Stokes component will be free of NRB. TD-CARS therefore enables experimental NRB suppression

vibrational modes. Indeed, there must be two interactions with the pump beam, to excite and probe the vibrational modes, so it is impossible to introduce a time delay between pump and stokes. Instead with the three-colour mechanism the Stokes beam excites the vibrational modes acting both as pump and Stokes, while the pump acts just as probe. This allows to delay the pump suppressing the NRB contribution.

TD-CARS main perk is the optical suppression of NRB without the need for further post-processing. On the other hand naturally, the main disadvantage is the loss of the the amplification provided to the CARS signal by the NRB. Removing the NRB therefore will lead to a lower sensitivity and lower signal-to-noise ratio. This problem can be solved with longer integration times, which means that TD-CARS is a technique more suitable for spectroscopic applications than microscopic applications.

3 | Experimental Setup

In this section, we will focus on describing the working principles and design decisions behind the setup we used for all the experiments exposed in chapter 5. The system is quite elaborate, therefore we will divide it into three key parts according to their purpose:

- Light generation: as the name suggests it consists of all the components starting from the laser used that are necessary to produce the pump and Stokes pulses before they enter the microscope.
- Microscope: it includes the objectives and stage to focus the pulses on the sample, but it also includes the necessary components for brightfield illumination from the light source to the camera.
- Signal detection: it is the last part of the setup and its purpose is collecting the CARS signal with a camera and photomultiplier tube as well as synchronizing the whole acquisition via a data acquisition system (DAQ) and Matlab.

It is worth mentioning that my thesis and work involved both application and setup development, and my contribution to the setup mainly included adding the PMT acquisition and DAQ to synchronize the multiple channels, developing the code for the z-stack acquisition, adding and testing a different crystal for white light generation and writing the necessary code to generate acquire and stitch multiple BF images.
In the following sections, we will analyze in detail these components as well as the rest of the setup. In figure 3.1 we can see a schematic representation of the whole setup from which we can follow the description of each element.

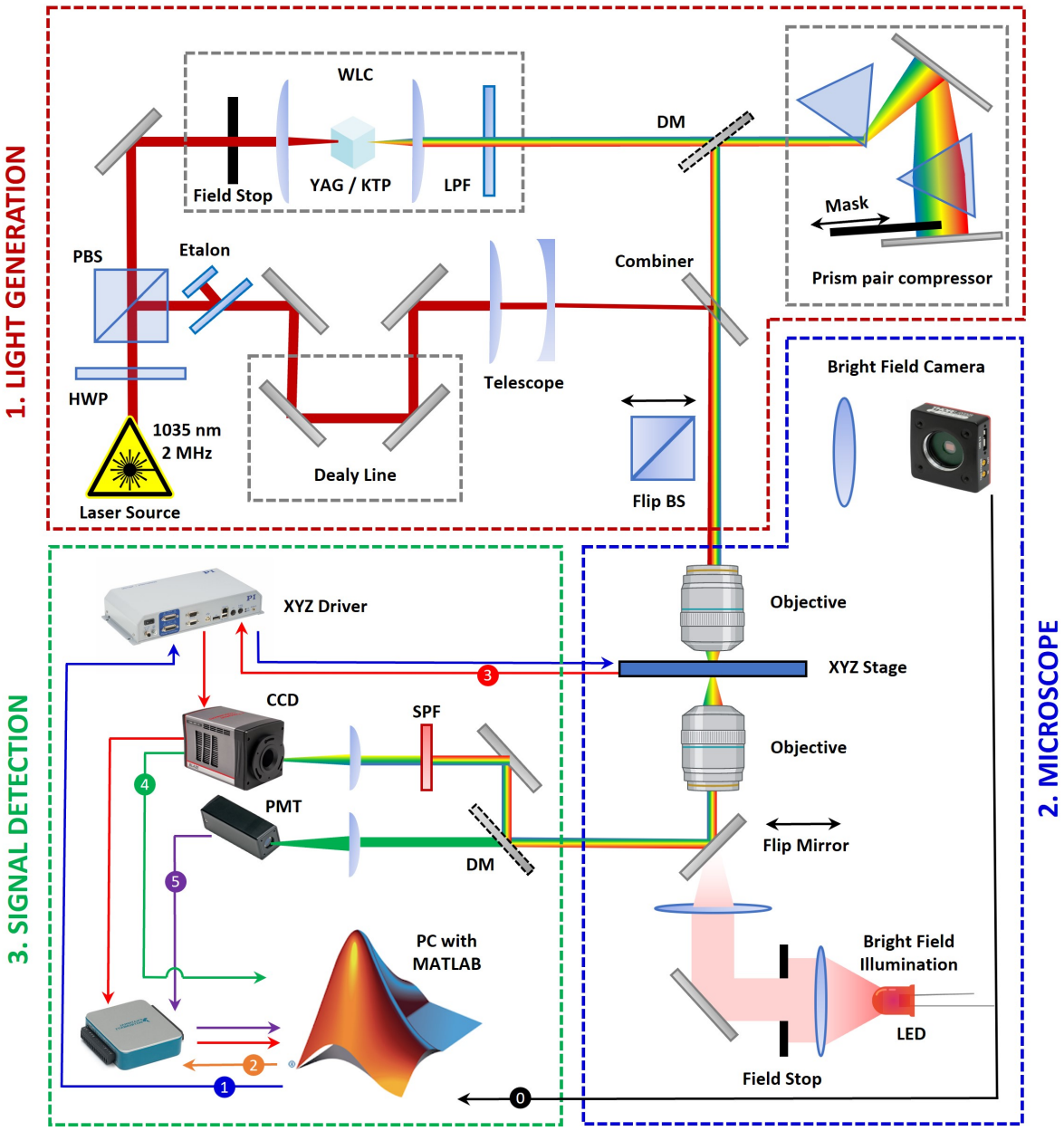

Figure 3.1: Simplified but complete representation of the experimental setup. Note that the propagation of the laser beam starts in red and remains red for the Pump while the Stokes is represented with multiple colours as the pulse gets broadband. I also reported the components that would be flipped for Brightfield (BF) acquisition but the BF light here is interrupted by the flip mirror. We'll focus on this part more in detail in section 3.2 and from image 3.3 we can see how the setup works with the correct components flipped and the BF light not blocked. Additionally, at the bottom of the image, we can see the cables connecting each peripheral to the computer running Matlab where each step where data is transferred from or to a component is represented with a different colour. We'll focus more on this part in the last section of the chapter.

3.1. Light Generation

We will describe this and the next parts of the setup following the direction of the laser beam from its optical source, following one optical path at a time.

Our system begins with a commercially available fibre-based ytterbium laser system (Monaco 1035, Coherent), which delivers pulses of approximately 270 femtoseconds duration. These pulses have a spectral bandwidth of 10 nm, duration of $270fs$ and are centred at a wavelength of $\lambda_0 = 1035nm$. The laser system offers adjustable repetition rates from 1 to 50 MHz and a maximum average power of 60 W. For our experiment, we set the repetition rate at 2 MHz and the average power at approximately 6 W.

The laser output is divided into two branches, with their power controlled using a combination of a half-wave plate (HWP) and polarizing beam splitter (PBS). The first beam replica, with an average power of approximately 2 W, passes through a high-finesse Fabry–Perot etalon (air-space etalon, SLS Optics). This etalon narrows down the spectral bandwidth, resulting in the generation of narrowband pump pulses. The result is a narrowband pump beam with FWHM around $0.9nm$ that corresponds to a wavenumber around or inferior to $9cm^{-1}$ for $\lambda = 1035nm$. These pulses are crucial for achieving the desired spectral resolution in the CARS spectra, matching the typical line widths of vibrational Lorentzian peaks in condensed media [41].

The second beam replica, with an average power of approximately 4 W, is used to generate a White-Light Continuum (WLC) in a 10 mm YAG (or KTP) crystal as we can see in figure 3.2. To achieve WLC, the replica beam passes through another HWP-PBS system, enabling fine-tuning of the intensity incident on the crystal. An iris is utilized to control the beam's divergence, after which it is focused by a 75 mm lens onto the 10-mm-thick YAG (or KTP) crystal. The crystal is mounted on a single-axis translational stage. Subsequently, a second 75 mm lens collimates the beam without altering the spot size.

To select the red-shifted lobe of the Supercontinuum (SC) (ranging from 1050nm to 1600nm) while filtering out the fundamental beam and the blue-shifted components, a long-pass filter (LP1050, Thorlabs) is employed. The chirp of the broadband beam induced by its propagation through the optical path and the objectives is compensated by an SF11 prism pair compressor with an apex-to-apex distance of 60 cm. To finely adjust the bandwidth of the Stokes beam, a homemade mask is placed after the second prism of the compressor, allowing all colours to propagate in parallel.

The generated Stokes pulses exhibit a sub-20 femtosecond pulse duration at the sample plane, after passing through the illumination objective, and possess a bandwidth spanning

from 1200nm to 1600nm, adjustable depending on the desired excitation mechanism and application. The spatiotemporal overlap between the two pulse trains is achieved by finely adjusting a dichroic mirror (Di02-R1064-25x36, Semrock) and employing a manual delay line mounted on the pump beam path.

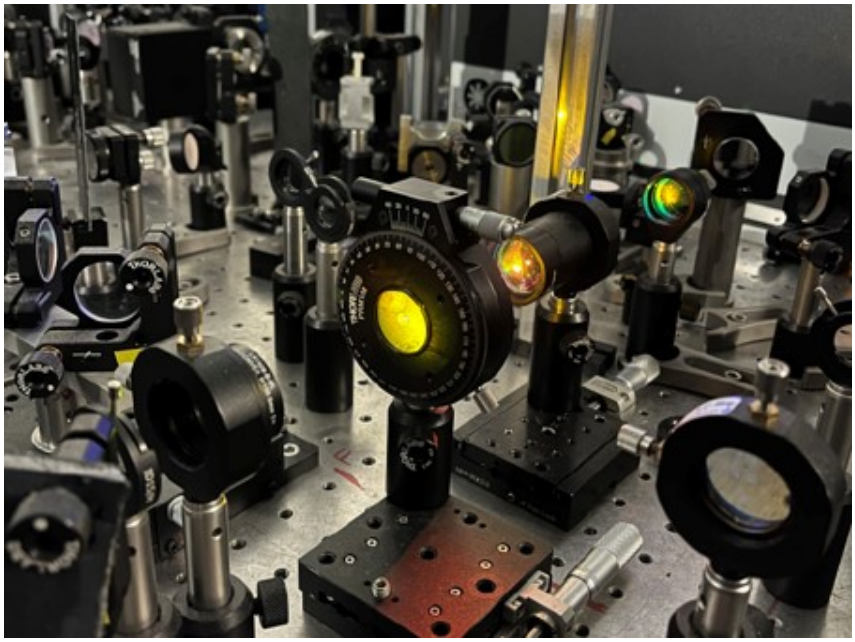

Figure 3.2: Picture of the WLC stage.

3.2. Microscope

Following the generation module, our experimental setup utilizes an upright confocal microscope configuration. This microscope, a custom design, allows two beams to enter the system. These beams are merged using a dichroic mirror (Di02-R1064-25x36, Semrock). We use a pair of 100x air objectives with a high Numerical Aperture (NA) (Olympus LCPLN100XIR, NA=0.85) to focus the two beams collinearly onto the sample plane and to collimate the transmitted BCARS beam. These objectives are mounted on individual XYZ manual stages for precise positioning.

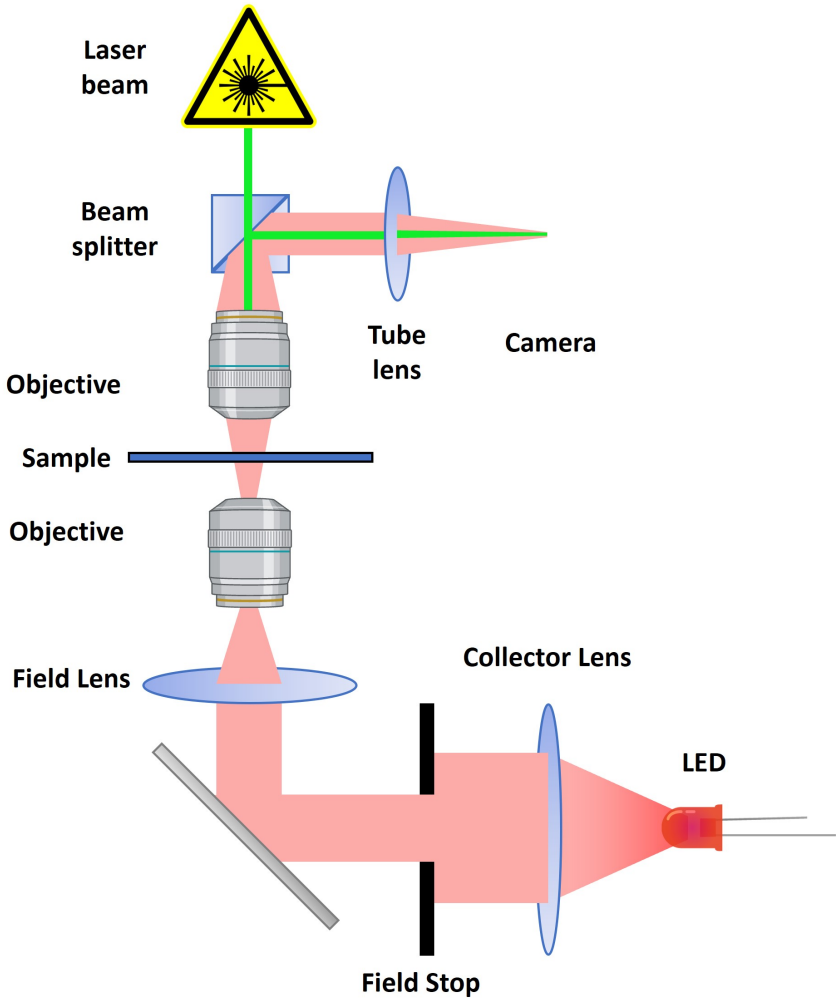

Figure 3.3: In-depth scheme of just the microscope and the pseudo-Kohler illumination configuration implemented. The LED light providing the brightfield illumination is represented here in red, while the green light represents the laser beam coming from the light generation module.

To ensure a proper match between the spot sizes of the two beams and the size of the

back aperture of the illumination objective, we employ a telescope configuration. This is vital to prevent power loss before the beams reach the sample and to avoid reducing the effective NA of the objective in use, which could compromise the spatial resolution of the images acquired. The telescope minimizes the beam size of the pump beam, which slightly diverges after propagating over several meters on the optical table.

We accomplish sample scanning using two translational stages: the PI-nano XYZ stage (P-545.3R8S, Physik Instrumente) and an XY motorized translation stage (U-780.DNS, Physik Instrumente), stacked one on top of the other. The former allows for fine adjustment of the sample position in the X, Y, and Z directions, enabling movement over a range of 200 µm along all three axes. The latter is used for raster scanning of the sample over larger areas, up to approximately 2x2 cm2 (limited by the presence of the collection objectives that may collide with the stage). By combining these two translation stages, we can acquire the sample image using a raster scanning approach.

Additionally, the microscope is equipped with a bright-field microscopy system to visualize the field of view that needs to be imaged using BCARS. A LED serves as the light source, and a lens configuration, consisting of two objectives and another lens, creates a pseudo-Kohler illumination system. Finally, a camera (Thorcam, Thorlabs), positioned in the image plane, allows us to capture wide-field images of the sample. The schematic representation of the pseudo-Kohler illumination configuration is shown in Figure 3.3

3.3. Signal Detection

After the BCARS signal passes through the microscope, it enters the final section of the setup responsible for the synchronous data acquisition of the B-CARS signal via the CCD and PMT. A 35 mm focusing lens (Acton SP2150p, Princeton Instruments) focuses the signal onto the detection system, specifically the slit aperture of the spectrometer, ensuring proper collection of the anti-Stokes light directed towards the spectrometer.

The collimated beam carrying the B-CARS signal passes through a long-pass dichroic mirror (FF757-DI01). The light transmitted by the dichroic then passes through a short-pass filter (SP1000, Thorlabs). This filter selectively transmits wavelengths below 1000 nm, effectively blocking the pump and Stokes pulses while allowing the BCARS signal, centred at shorter wavelengths, to pass through.

The detection module comprises two elements: A spectrometer and CCD camera combination for one acquisition channel and a PMT for the other channel. The spectrometer of the first channel is equipped with 600 grooves/mm grating (AC-TON SP2150, Princeton Instruments), which effectively separates the different wavelengths of the BCARS signal. Accompanying the spectrometer is a back-illuminated deep depletion CCD camera (BLAZE100HR, Princeton Instruments), facilitating the achievement of a spectral resolution of 0.47 nm, corresponding to 5.8 cm^{-1}. The Photomultiplier Tube Module of the second channel (PMT, H10721-110, Hamamatsu) instead is paired with a transimpedance to convert and amplify the detected signal.

Both channels are synchronized with the XYZ scanning stage through an ad-hoc MATLAB interface, enabling the real-time monitoring of both channels. The whole system is handled via Matlab in conjunction with a Data Acquisition (DAQ) system (NI USB-6341) to achieve simultaneous acquisition.

After the BCARS signal passes through the microscope, it enters the final section of the setup responsible for the synchronous data acquisition of the B-CARS signal via the CCD and PMT. Initially, a 35 mm focusing lens (Acton SP2150p, Princeton Instruments) focuses the signal onto the detection system, specifically the slit aperture of the spectrometer, ensuring proper collection of the anti-Stokes light directed towards the spectrometer.

After exiting the bottom objective, the collimated beam carrying the B-CARS signal corresponding to the illuminated pixel, passes through a long-pass dichroic mirror (FF757-DI01). The light transmitted by the dichroic then passes through a short-pass filter (SP1000, Thorlabs). This filter selectively transmits wavelengths below 1000 nm, effectively blocking the pump and Stokes pulses while allowing the BCARS signal, centred

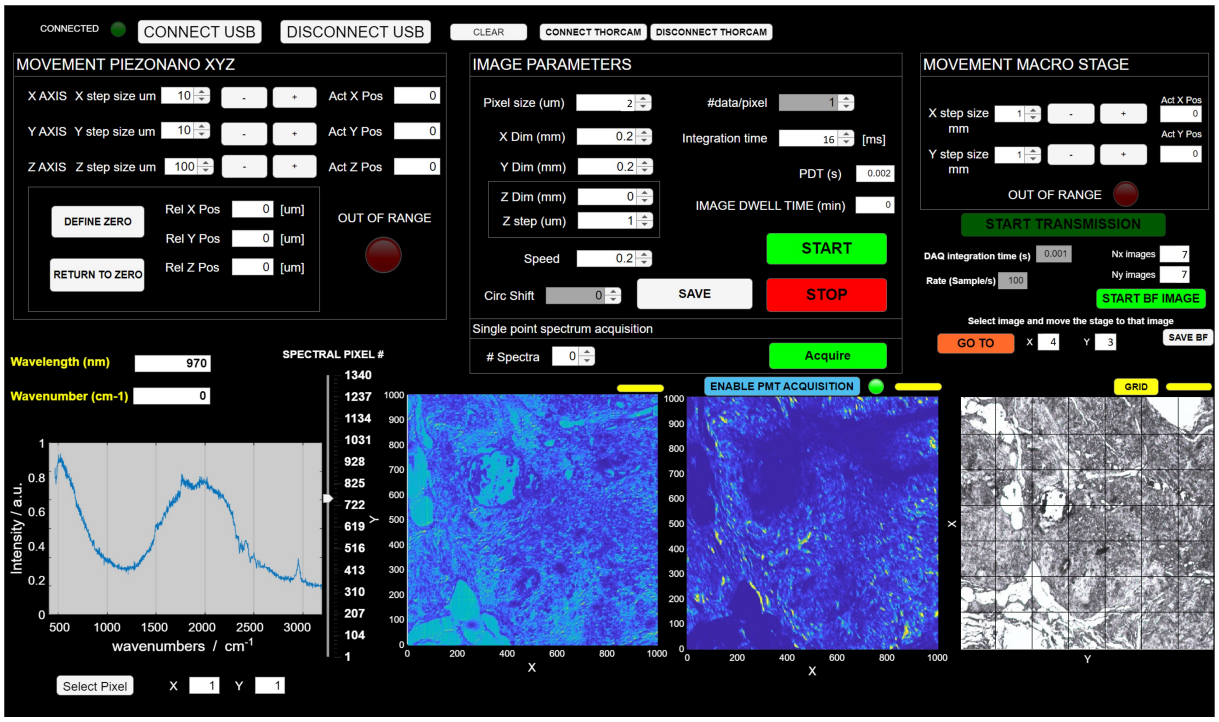

Figure 3.4: Matlab graphical user interface for the acquisition of the CARS images. In the interface, we can see the panels to control the two stages on the top left and right. At the top centre, there is the control panel to set the acquisition parameters. In the bottom part of the image instead, we can see from left to right the different acquired channels: B-CARS spectrum in a pixel, B-CARS image, PMT image (in this case set for 3PEF) and Brightfield stitched image.

at shorter wavelengths, to pass through. This spectral filtering ensures that the desired BCARS signal is isolated for detection. The light reflected by the dichroic will also be filtered according to the process we want to monitor, for SHG we use a short-pass filter that transmits frequencies below $800nm$ for example.

The detection module comprises two elements: A spectrometer and CCD camera combination for one acquisition channel and a PMT for the other channel. The spectrometer of the first channel is equipped with 600 grooves/mm grating (AC-TON SP2150, Princeton Instruments), which effectively separates the different wavelengths of the BCARS signal. Accompanying the spectrometer is a back-illuminated deep depletion CCD camera (BLAZE100HR, Princeton Instruments), facilitating the achievement of a spectral resolution of 0.47 nm, corresponding to 5.8 cm^{-1}. The Photomultiplier Tube Module of the second channel (PMT, H10721-110, Hamamatsu) instead is paired with a transimpedance to convert and amplify the detected signal.

Both channels are synchronized with the XYZ scanning stage through an ad-hoc MATLAB interface reported in figure 3.4, enabling the real-time monitoring of both channels. Note that the interface also includes and controls the "third" channel made by the camera which is used to capture brightfield images.

The whole system is handled via Matlab in conjunction with a Data Acquisition (DAQ) system (NI USB-6341) to achieve simultaneous acquisition. The whole process can be understood following the order of the signal as reported in figure 3.1.

- The first signal to acquire is the BF image to identify an interesting area of the sample. So Matlab will control directly the stage through its driver (signal 1) and measure the BF image (signal 0). It is also possible to automatically acquire multiple images, stitch them together storing the position of each tile, and then move to a specific location.
- Once an interesting location is found we can start measuring simultaneously via the two channels. Just like before Matlab will control directly the stage (signal 1) using its driver to perform raster scanning pixel by pixel, and it will start the acquisition through the DAQ (signal 2).
- Once the stage moves it sends a signal back to the driver (signal 3 part 1) and the driver sends a trigger to the camera (signal 3 part 2) to acquire a spectrum. The instant the camera starts a measure, it sends another trigger to the DAQ (signal 3 part 3) which reads it and sends it to Matlab (signal 3 part 4). These triggers will be used to synchronize the measurements of CCD and PMT.
- The CCD also send the acquired spectra directly to Matlab through a USB interface (signal 4).
- During the whole process the PMT signal was continuously sent to the DAQ (signal 5) which started acquiring and sending the signal to Matlab when it was triggered by signal 2.
- Finally once the measure is completed Matlab uses the recorded triggers from the CCD (signal 3 part 4) to select in the data recorded by the PMT the intervals that coincide with each pixel acquired by the CCD.

Note that the CCD camera acquires a CARS spectrum at each trigger event, utilizing binning over 100 rows and providing 1340 spectral points. This procedure is repeated for multiple pixels, resulting in a hyperspectral image. Each image is represented by a three-dimensional matrix ($N \times M \times 1340$), where the first two dimensions represent the spatial axes, and the third dimension represents the spectral points.

This approach allows the acquisition of images at very high speeds, utilizing the minimum exposure time allowed by the CCD camera which is 0.8 ms. Moreover, each pixel can be associated with a specific spatial position, without encountering any motion artifacts or shifts in the rows of the acquired images.

4 | Acquisition and Data Processing

The following sections will outline the procedure for acquiring and processing BCARS signals. Our raw images are not just standard RGB images where each pixel is associated with a colour indicated by 3 numbers. Instead, each pixel is associated with 1340 numbers representing the spectrum of the pixel. For this reason, the data processing will require both spectroscopic and microscopic analyses. The chapter will be organized into two main parts. The first concerns the acquisition procedure which includes an initial alignment of the experimental setup, preliminary measurements, acquisition of bright-field images and acquisition of B-CARS images. The second concerns all the techniques needed after we acquire all the spectra to clean them from artefacts and retrieve the chemical information. It comprises an initial calibration of the wavenumber axis of the system followed by noise reduction and NRB removal to obtain a clean baseline image. From this image, we can work to retrieve the spectral and chemical information we need using spectral unmixing algorithms.

4.1. Acquisition

4.1.1. Preliminary Measurements and calibration

The base of every successful measurement is a good setup alignment and in our case, it consists of two major components. The first is the spatial and temporal overlap of the Pump and Stokes pulses at the sample plane and the correct alignment of the anti-Stokes component with the spectrometer. The second one is the stability of the broadband source, which depends on the impinging power, iris aperture and crystal position concerning the focal plane. To tune it we need to monitor the spectrum of the broadband Stokes through a NIR spectrometer (Avantes NIR256-1.7-EVO) and measure its RMS fluctuations. Since this last step involves tuning several parameters we made a simple GUI to simplify the process. The program can be seen in figure 4.1, it shows a previously measured spectrum in an optimal configuration and reports live the current one measured by the spectrometer with its RMS fluctuation. This way we can tune the system until we find a configuration as good or better than the recorded one and we can keep monitoring the stability during the whole measure.

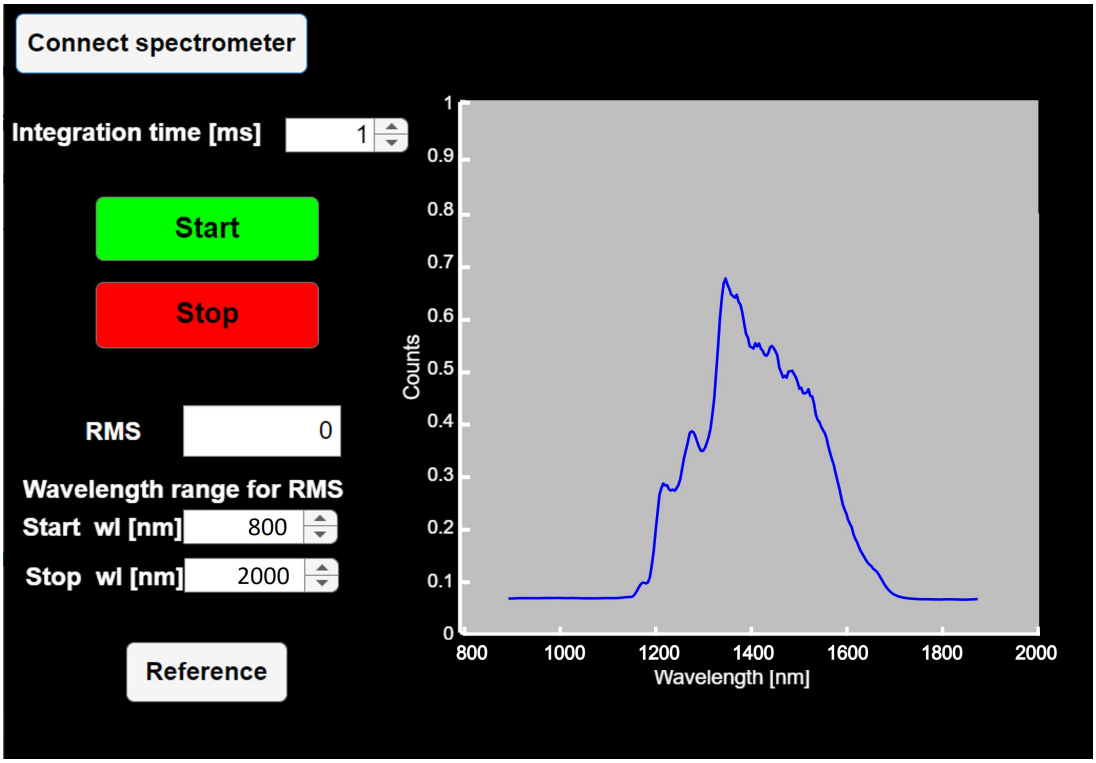

Figure 4.1: Graphical User Interface for fine-tuning and monitoring the white light generation.

Once the setup is aligned correctly, a calibration procedure is required on a daily or weekly

basis. It consists of three measurements:

1. we take 100 spectra of Toluene (other materials with plenty of peaks in the fingerprint and CH-region could work too)
2. we take 100 spectra of NRB (NRB is taken focusing on glass coverslip)
3. we take 100 spectra of just dark blocking the laser beams to later remove the RMS noise due to the dark counts of the CCD.

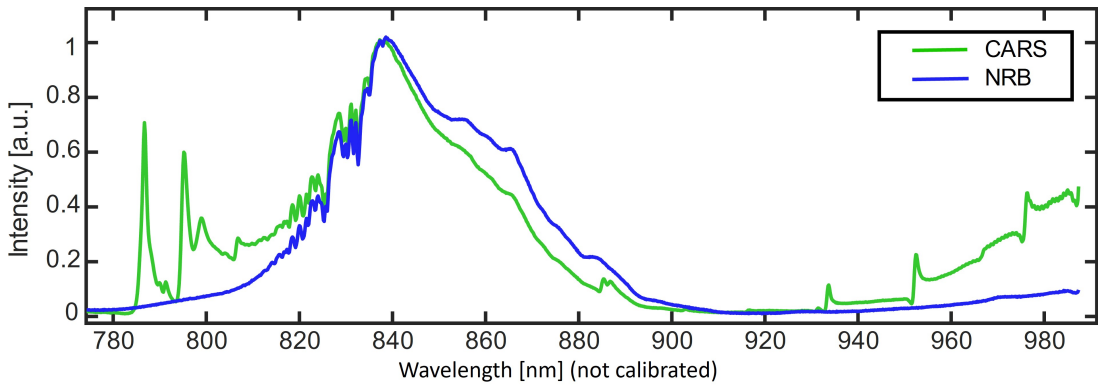

Figure 4.2: Raw CARS spectrum of Toluene and NRB.

As we can see in figure 4.2 the raw data present a strong NRB and the wavelength axis is not calibrated. The preliminary measurements mentioned above are instrumental in fixing these problems.

First and foremost we take the average of each spectrum, subtract the average dark from toluene and NRB and remove the NRB through the time-domain Kramers-Kronig algorithm (NRB removal will be treated in depth in section 4.2.2). Then we can calibrate the wavenumber axis by fitting a third-order polynomial function between the measured and spontaneous Raman peak positions of the main Raman peaks of toluene. We use always the same main 8 peaks of toluene and then evaluate the performance of the procedure by computing the errors between the retrieved and spontaneous Raman peaks positions as can be seen in figure 4.3. The used reference toluene spectrum is obtained by averaging 5 spectra acquired with a custom SR setup present in the laboratory which uses an inverted Olympus microscope paired with a CW laser (Cobolt Flamenco 660 nm 100 mW).

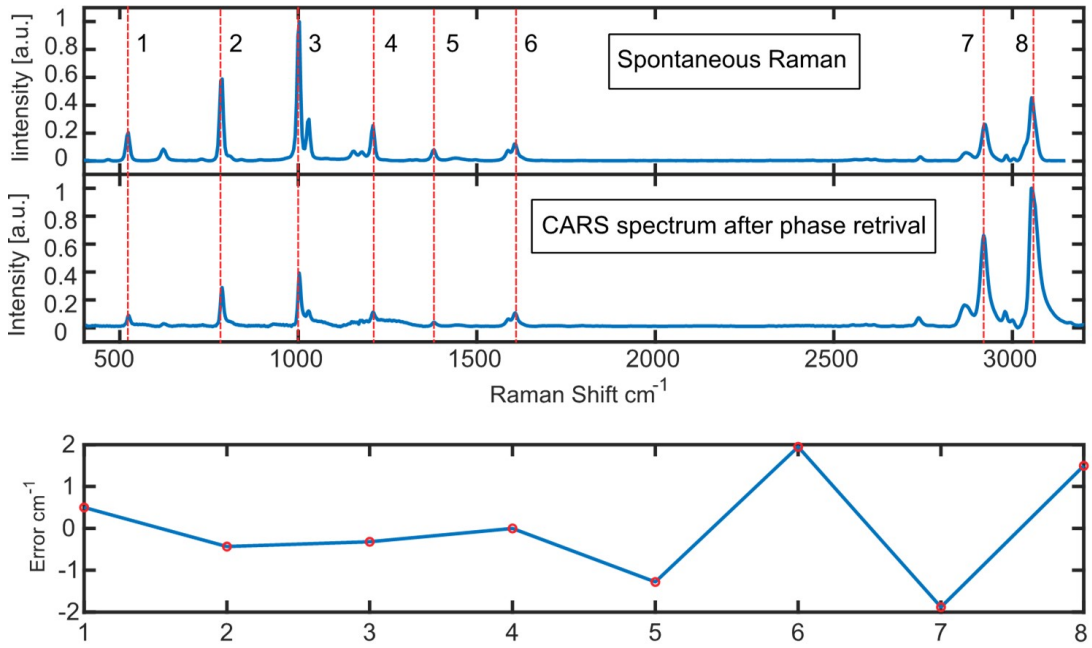

Figure 4.3: 2 colour B-CARS spectrum of the two different chemical species after NRB removal acquired with 1ms integration time.

4.1.2. Bright-field Image

Once we have the wavelength axis calibrated we are ready to find a spot on the sample to collect the CARS signal. To do so we need to visualize the sample (in case we only want to capture the CARS spectrum this step is not necessary) to find the best spot to capture the image and focus the microscope. This is key for two reasons, first in complex biological samples it may be necessary to acquire multiple images and merge them to find the features subject of a particular study. And second, to maximise the CARS signal by focusing the microscope and monitoring the spectrum we need to position the laser beams on a relevant spot in the sample. For example, when measuring test samples made of polymethyl methacrylate (PMMA) beads in dimethyl sulfoxide (DMSO) we want to maximise the weaker signal of the plastic beads, so we will position the laser beam on a bead using the brightfield and then fine-tune the focus to maximise the CARS signal. The same process is used in more complex biological samples when there are specific features we want to analyze. When samples are particularly large however it's time-consuming to manually move the stage monitoring the BF camera, so we implemented in the GUI presented in figure 3.4 the possibility to acquire stitched BF images with the possibility to move to specific areas of the reconstructed image. A simple example of a stitched brightfield image is reported in figure 4.4.

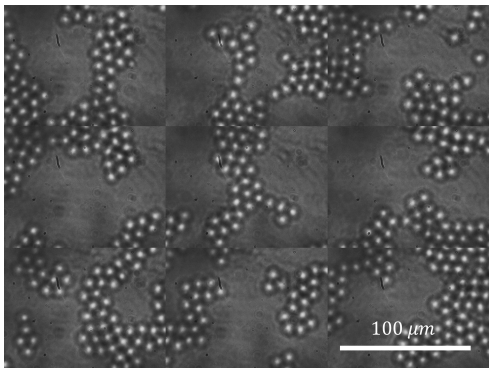

Figure 4.4: Example of a 3x3 tile stitched image of a large test sample made with plastic polymethyl methacrylate (PMMA) bead in dimethyl sulfoxide (DMSO).

4.1.3. Multichannel Acquisiton

After the above-mentioned procedures, measurements with the CCD and PMT can begin. We use the interface presented in figure 3.4 both before and during the measure to monitor the process and perform real-time adjustments to ensure high-quality results. Typical parameters that can be fine-tuned at this stage are the pump and Stokes power and the pixel dwell time to avoid saturating any pixel of the final image. The additional information from CARS can also be used to further check if the area selected is relevant as the bright-field image suggested or if it is necessary to enlarge the field of view, move or use smaller pixel dimensions for higher resolution.

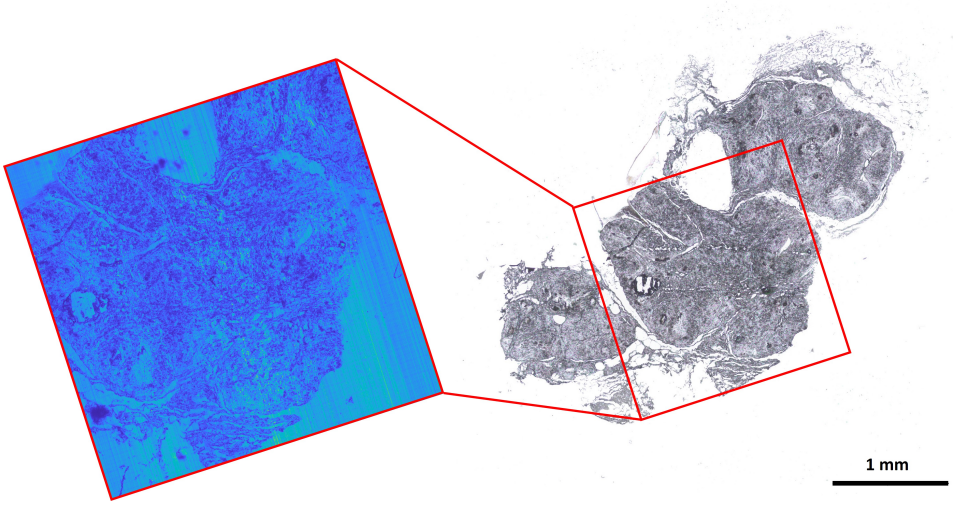

Figure 4.5: On the right we can see a stitched image of breast tissue where in red is highlighted the region of interest where we can find a microcalcification. On the left, we can see the raw CARS data integrated over all Raman shifts concerning the region of interest. These samples will be studied more in detail in Chapter 5.

4.2. Processing

The B-CARS data obtained from the camera is affected by various artefacts such as those caused by the instrumentation, sample characteristics, noise, fluctuations of the laser source and distortion introduced by the NRB. Indeed, from image 4.5 we cannot retrieve much chemical information straight away and applying unmixing algorithms at this point will not be effective. Instead, to ensure accuracy and reliability, another procedure is required to retrieve the pure vibrational information while eliminating unwanted contributions. Only after the signal is improved a spectral unmixing algorithm is used to locate different chemical species in heterogeneous samples. In this section, we describe the procedure and algorithms used to achieve these goals.

4.2.1. Denoising via Singular Value Decomposition (SVD)

Among the different noise sources that could affect our signal, a predominant one is white noise, primarily stemming from the inherent dark noise of the CCD. Consequently, it becomes necessary to eliminate it. To achieve noise reduction in B-CARS hyperspectral data, we can employ singular value decomposition (SVD) on Anscombe-transformed spectra [42, 43].

The SVD technique in particular operates well when the noise follows a normal distribution, also called Gaussian noise. Our signal noise however does not follow a normal distribution, but it contains a combination of Gaussian and Poisson noise. So the Anscombe transform [44] can be applied to the B-CARS hyperspectral data to stabilize the variance, "whitening" the noise. Only at this point the SVD can be applied and then the inverse Anscombe transform will be used to restore the B-CARS spectra with mixed noise.

Now we will focus on the singular value decomposition (SVD) denoiser employed. The B-CARS dataset is initially in a three-dimensional format, with dimensions of $m \cdot n \cdot s$. With, m and n representing the number of spatial pixels along the x-axis and y-axis respectively, and s representing the number of spectral pixels. To apply the SVD algorithm, the dataset will be unfolded into a two-dimensional matrix M. In this matrix, the rows represent the spectral axis with s spectral points, while the columns represent the spatial pixels from both axes. The SVD algorithm decomposes this matrix into three components:

$$M = USV^* \tag{4.1}$$

Where the matrix U is a two-dimensional matrix $(s \cdot s)$ containing the spectral bases,

which are orthonormal eigenvectors. The matrix S is diagonal $(s \cdot s)$ containing the singular values, or eigenvalues, in descending order of magnitude. The matrix V $(p \cdot s)$ describes the spatial distribution of the bases in U (The symbol "*" indicates that it's a conjugate transpose).

So the SVD decomposition can be seen as a decomposition of the original matrix M into a weighted and ordered sum of contributions from most to least important. The first singular values will contain the highest spatial and spectral coherent contributions.
For noise removal then, a straightforward approach is setting an arbitrary cut-off threshold, all the singular values beyond this threshold (C) will be set to zero, effectively making zero part of the higher diagonal elements of S. Then the denoised hyperspectral data matrix can be reconstructed using the following procedure (where $\hat{S} = S\{1 : C\}$):

$$\hat{M} = U\hat{S}V^* \tag{3.2}$$

Note that the procedure is exactly the inverse of the initial decomposition but now we used the new diagonal matrix with part of the diagonal elements set to zero. This denoising approach works by taking advantage of the fact that noise is typically random in space and exhibits high frequencies in spectra [45].

Note that to achieve good results with this method it is extremely important to select appropriate singular values for the reconstruction of the hyperspectral data. Indeed, selecting too few will not succeed in removing noise, but selecting too many will delete also valuable information. We must find a tradeoff, ideally with a more accurate method than directly choosing an arbitrary threshold.

In this regard, the method we choose to select singular values is indeed more elaborated than those described until now. To determine the suitable singular values, we transform the absolute values of the spatial components for each singular value $(|V|)$ using a two-dimensional Fourier transform. In the Fourier domain, a rectangular boundary is applied to separate the high-frequency components (mostly noise) from the low-frequency components (mostly signal). The high-frequency components outside the boundary primarily consist of noise, while the low-frequency components inside the boundary predominantly contain the signal.

Then we introduce a new quantity called "spatial signal ratio" (SSR), which quantifies the relationship between pixel intensities within and outside a designated boundary in the Fourier transform components. It is computed as the sum of pixel intensities inside the boundary, represented by the complex modulus of the Fourier transform components,

divided by the sum of pixel intensities outside the boundary. This ratio is then scaled by the respective number of pixels within and outside the boundary.

The purpose of this procedure is to only consider singular values that exhibit high SSR and contain relevant signal information. The cut-off value, that discriminates the high and low SSR, is given by a multiple of σ, where σ is the standard deviation calculated from the SSR of the highest singular values.

4.2.2. Non-Resonant Background (NRB) Removal

After the initial denoising mentioned in the previous section and a quality check of the results obtained thus far the next fundamental step is NRB removal. The raw spectrum of each pixel is deformed exactly in the same way as the calibration spectrum reported in figure 4.2. So as we did with the calibration spectrum we need to remove the NRB to restore the traditional lineshape of the signal too. This is instrumental for the unmixing procedure that will occur later but also to help us identify relevant features in the spectrum.

Note that the NRB arises from the combined effects of resonant and non-resonant susceptibility, leading to spectral distortions as seen in section 2.2.1. However, the NRB amplifies the faint Raman signals, enabling high-sensitivity detection even in the fingerprint region where signals tend to have low intensity [39] [46]. For this reason for imaging applications, we avoid optical methods to suppress NRB because they would also lead to weaker CARS signals and longer acquisition times. We will briefly treat one of those methods for spectroscopic applications in section 5.4.

Therefore now we will focus on numerical methods to manage the NRB distortion which utilize phase-retrieval techniques, leveraging the inherent heterodyne nature of the CARS signal. These methods can be divided into two classes, the first class involves maximizing entropy through the Maximum Entropy method (MEM) [32], while the second class exploits phase retrieval using the time-domain Kramers-Kronig (KK) relations [47]. It is worth noting that these techniques are functionally equivalent [31] and have been successfully applied to various sample types, including materials [46] [48] and biological samples [49] [50].

In section 2.2, it has been shown that the intensity of the CARS scales with the square of the modulus of the third-order nonlinear susceptibility $\chi^(3)_{VIB}$ which is obtained by combining the resonant and non-resonant contributions $\chi^{(3)}_{VIB} = \chi^{(3)}_R + \chi^{(3)}_{NR}$ so:

$$I_{CARS} \propto \left|\chi^{(3)}\right|^2 = \left|\chi_R^{(3)} + \chi_{NR}^{(3)}\right|^2 = \left|\chi_R^{(3)}\right|^2 + \left|\chi_{NR}^{(3)}\right|^2 + 2\chi_{NR}^{(3)}\mathrm{Re}\left(\chi_R^{(3)}\right) \tag{4.2}$$

Where the resonant susceptibility $\chi_R^{(3)}$ is a complex number, with the real part exhibiting a dispersive shape and the imaginary part demonstrating a Lorentzian shape. On the other hand, the non-resonant susceptibility $\chi_{NR}^{(3)}$ is real when it is sufficiently far from electronic resonances. So MEM and KK methods can exploit these differences to retrieve the phase $\phi(\omega)$ of $\chi^{(3)}$ to isolate the imaginary Raman resonant component $\mathrm{Im}[\chi_R^{(3)}]$ from the overall nonlinear susceptibility.

Let's now focus on the Kramers-Kronig method specifically, which was the one used in all our experiments.

We can start by writing the CARS signal in terms of electric field instead of pump and probe as usual:

$$I_{CARS}(\omega) = \left|\{[E_s(\omega) \otimes E_p(\omega)]\chi^{(3)}(\omega)\} * E_p(\omega)\right|^2 \triangleq \left|\tilde{C}_{st}\right|^2 \left\|\tilde{\chi}^{(3)}\right\|^2 \tag{4.3}$$

Where E_S and e_P are the electric fields of the Stokes and pump beams, $\otimes$ indicates the cross-correlation operators, and $*$ is the convolution operator. $\tilde{C}_{st}$ is the coherent stimulation profile and it corresponds to the correlation between pump and probe fields:

$$C_{st} = E_s(\omega) \otimes E_p(\omega) \tag{4.4}$$

If we assume a spectrally narrow pump beam, we can introduce an effective stimulation profile $\tilde{C}_{st}$ and the effective nonlinear susceptibility $\tilde{\chi}^{(3)}(\omega)$ as:

$$\tilde{C}_{st} = \frac{E_s(\omega) \otimes E_p(\omega)}{\int E_p} \tag{4.5}$$

$$\tilde{\chi}^{(3)}(\omega) = \chi^{(3)}(\omega) * E_p(\omega) \tag{4.6}$$

The time domain Kramers-Kronig relations establish an explicit connection between the real and imaginary components of a function, denoted as $f(\omega)$. In the context of CARS, neither the real nor imaginary part of the third-order susceptibility, $\chi^{(3)}$, can be directly observed. Furthermore, when the function is square integrable, its complex norm and phase are intricately related.

$$n\left(|f(\omega)|\right) = -\hat{\mathscr{H}}(\phi(\omega)) \tag{4.7}$$

$$\phi(\omega) = \hat{\mathscr{H}}\left(\ln\left(|f(\omega)|\right)\right) \tag{4.8}$$

Where $\hat{\mathscr{H}}$ is the Hilbert transform. In principle, to apply these formulas, the complex modulus or the phase of the function over an infinite range of frequencies must be known. However, the CARS spectrum is limited in frequency; we measure only a portion of the spectrum. Thus, a "windowed Hilbert transform" $\hat{\mathscr{H}_w}$, limited between frequency ω_a and ω_b, is required. It is defined as follows:

$$\hat{\mathscr{H}_w}\left(f(x); \omega_a, \omega_b\right) = \frac{\mathscr{P}}{\pi} \int_{\omega_a}^{\omega_b} \frac{f(x')}{x - x'}\, dx' \tag{4.9}$$

Where $\mathscr{P}$ is the Cauchy principal value. These formulas hold under the following two conditions:

- The Raman peaks that are contained inside the spectral window are not affected by those outside of the window.
- We are far from any electronic resonances, as is typically the case with infrared pumps and Stokes.

The windowed and analytic Hilbert transform are related by the following relationship:

$$\hat{\mathscr{H}_w}\{\frac{1}{2}\ln(\left|\tilde{\chi}^{(3)2}\right|)\} \approx \hat{\mathscr{H}}\{\frac{1}{2}\ln\left(\tilde{\chi}^{(3)2}\right)\} + \epsilon(\omega) \tag{4.10}$$

Where $\epsilon(\omega)$ is an additive term introduced using the windowed version of the Hilbert transform. Applying the windowed Hilbert transform (3.10) to the logarithm of the CARS signal intensity (3.7) and considering the properties (3.9) and (3.11), we can obtain the retrieved phase from the raw CARS spectrum, ϕ_{CARS}:

$$\begin{aligned}
\phi_{\mathrm{CARS}}(\omega) &= \hat{\mathscr{H}_w}\left\{\frac{1}{2}\ln\left(I_{CARS}(\omega)\right)\right\} \\
&\approx \epsilon(\omega) + \hat{\mathscr{H}}\left\{\frac{1}{2}\ln\left|\tilde{\chi}^{(3)2}\right|\right\} + \hat{\mathscr{H}_w}\left\{\frac{1}{2}\ln\left|\tilde{C}_{st}^{2}\right|\right\} \\
&= \epsilon(\omega) + \hat{\mathscr{H}_w}\left\{\frac{1}{2}\ln\left|\tilde{C}_{st}^{2}\right|\right\} + \angle\left[\chi_R(\omega) + \chi_{NR}(\omega)\right]
\end{aligned} \tag{4.11}$$

where Arg represents the phase. In the assumption that we can measure directly the NRB intensity $I_{NRB} = |\tilde{C}_{st}|^2|\tilde{\chi}^{(3)NR}|^2$, without Raman components and that we are far from electronic resonances such that $\chi^{(3)NR}$ is almost real, we could apply the windowed Hilbert transforms to the ratio $\frac{I_{CARS}}{I_{NRB}}$.

$$\begin{aligned}
\phi_{CARS/NRB}(\omega) &= \hat{\mathscr{H}}_w\left\{\ln\left(\frac{I_{CARS}(\omega)}{I+NRB(\omega)}\right)\right\} \\
&\approx \epsilon(\omega) + \hat{\mathscr{H}}_w\left\{\frac{1}{2}\ln\left|\tilde{C}_{st}^2\right|\right\}+ \\
&-\left[\epsilon(\omega) + \hat{\mathscr{H}}_w\left\{\frac{1}{2}\ln\left|\tilde{C}_{st}^2\right|\right\}\right] \\
&+\angle\Big[\chi_R(\omega)+\chi_{NR}(\omega)\Big] - \angle\chi_{NR}(\omega) \\
&\approx \angle\Big[\chi_R(\omega)+\chi_{NR}(\omega)\Big]
\end{aligned} \tag{4.12}$$

Using the ratio $\frac{I_{CARS}}{I_{NRB}}$ as our signal, the complex spectrum can be written as:

$$I_{CARS/NRB} = \sqrt{\frac{I_{CARS}(\omega)}{I_{NRB}(\omega)}}e^{i\phi_{\mathrm{CARS}/NRB}} \approx \frac{|\tilde{\chi}^{(3)}|}{|\tilde{\chi}^{(3)}_{NR}|}e^{i\angle[\chi^{(3)}_R+\chi^{(3)}_{NR}]} \tag{4.13}$$

The Raman spectrum I_{retr} can be extracted as the imaginary part of $I_{CARS/NRB}$:

$$I_{RL}(\omega) = Im\left\{I_{CARS/NRB}(\omega)\right\} \approx \frac{Im\{\chi^{(3)}_R(\omega)\}}{|\chi^{(3)}_{NR}|} \tag{4.14}$$

The imaginary part of the resonant third-order non-linear susceptibility carries the vibrational information. To a first degree of approximation [51] the spontaneous Raman spectrum is proportional to the imaginary part of the resonant susceptibility. Thus, the Raman-like spectrum is proportional to the spontaneous Raman spectrum scaled by the non-resonant component. The above method allows the extraction of the chemically-specific Raman signal from the NRB but it requires an accurate measurement of the NRB. In real-world conditions, the pure NRB of the sample cannot be measured directly. To overcome this problem the NRB is measured from a reference material with no Raman peaks, such as glass or water. So instead of the pure NRB measurement, we consider a reference measurement I_{ref}. By using the reference measurement, we introduce a multiplicative error such that $I_{ref}(\omega) = \zeta(\omega)I_{NRB}(\omega)$, where $\zeta(\omega)$ is assumed to be real and positive. Let us calculate the phase of the ratio $I_{CARS/ref}$, similarly to what we did previously with I_{NRB}:

$$\phi_{CARS/ref}(\omega) = \hat{\mathscr{H}_w}\left\{\frac{1}{2}\left(\ln\frac{I_{CARS}(\omega)}{\zeta(\omega)I_{ref}(\omega)}\right)\right\} \approx \phi_{CARS/NRB} + \hat{\mathscr{H}_w}\left\{\frac{1}{2}\ln\left(\frac{1}{\zeta(\omega)}\right)\right\} \quad (4.15)$$

where the last term is the phase error introduced $\phi_{err}(\omega)$. Then, the Raman-like spectrum is the imaginary part of the spectrum obtained as the ratio $I_{CARS/ref} = \frac{I_{CARS}}{I_{ref}}$, where we use I_{ref} instead of I_{NRB}:

$$Im\left\{I_{CARS/ref}(\omega)\right\} \approx \sqrt{\frac{1}{\zeta(\omega)}}\sqrt{\frac{I_{CARS}(\omega)}{I_{NRB}(\omega)}}\sin(\phi_{CARS/NRB} + \phi_{err}) \quad (4.16)$$

So, by using a reference NRB we get an amplitude error $A_{err} = \sqrt{\frac{1}{\zeta(\omega)}}$ and a phase error $\phi_{err} = \hat{\mathscr{H}_w}\left\{\frac{1}{2}\ln\frac{1}{\zeta(\omega)}\right\}$ that are connected by the Kramers-Kronig relation:

$$\ln(A_{err}) = -\hat{\mathscr{H}}\left\{\phi_{err}(\omega)\right\} \quad (4.17)$$

$$\phi_{err}(\omega) = \hat{\mathscr{H}}\left\{\ln(A_{err}(\omega))\right\} \quad (4.18)$$

However, a scaling error may be present. Since the Hilbert transform of a constant is equal to zero, then $\zeta(\omega)$ is multiplied by a constant α, and the phase error remains the same.

$$\phi_{err}(\omega) = \hat{\mathscr{H}_w}\left\{\ln\left(\frac{1}{\alpha\zeta(\omega)}\right)\right\} = \hat{\mathscr{H}_w}\left\{\ln\left(\frac{1}{\zeta(\omega)}\right)\right\} \quad (4.19)$$

To correct the phase and amplitude errors one can use the following steps:

- Remove phase error via detrending $\phi_{CARS/ref}(\omega)$ and correct part of the amplitude error exploiting the Kramers-Kronig relationship.
- Correct for scaling errors, related to the constant α, and for the use of the windowed version of the Hilbert transform in the previous step, ϵ_{err} via unity-centring the real component of the phase-corrected spectrum [42].

The phase $\phi_{CARS/ref}$ is qualitatively similar to a Raman-like spectrum in which the spectral peaks extend positively from a zero baseline. Slowly varying deviation from the zero baselines is caused by a slowly varying phase error ϕ_{err}. Thus, one can use traditional baseline detrending methods to find ϕ_{err} from $\phi_{CARS/ref}$ and remove it. Then, from ϕ_{err}, one

can retrieve part of the amplitude error and correct it. Finally, to get the phase-corrected spectrum I_{pc}, the retrieved spectrum $I_{CARS/ref}$ is multiplied by a complex phase-correction multiplier that takes into account the two corrections. The phase-corrected spectrum is as follows:

$$\begin{aligned} I_{pc} &= I_{CARS/ref}\left\{\frac{1}{e^{-\hat{\mathscr{H}}_w\{\phi_{err}(\omega)\}}}e^{-i\phi_{err}(\omega)}\right\} \\ &= \sqrt{\frac{I_{CARS}(\omega)}{I_{ref}(\omega)}}e^{i\phi_{CARS/ref}}\left\{\frac{1}{e^{-\hat{\mathscr{H}}_w\{\phi_{err}(\omega)\}}}e^{-i\phi_{err}(\omega)}\right\} \end{aligned} \tag{4.20}$$

Let's now consider the amplitude correction. We saw that retrieving A_{err} from ϕ_{err} leads to an ambiguity related to the scaling constant α. Furthermore, we are exploiting a window Hilbert transform instead of the analytical ones so window-effect error $\epsilon_{err}(\omega)$ is present:

$$\hat{\mathscr{H}}_w\{\phi_{err}(\omega)\} = \hat{\mathscr{H}}_w\{\phi_{err}(\omega)\} + \epsilon_{err} \tag{4.21}$$

To complete the error correction the ambiguity of A_{err} and $\epsilon_{err}(\omega)$ must be taken into account. Both quantities can be found by looking at the real component of the phase-corrected spectrum in (4.20). Since the real component of (4.15) is unitarily centred, which means that $\left\langle \frac{|\tilde{\chi}^{(3)}|}{|\tilde{\chi}^{(3)}_{NR}|}\cos(\phi_{CARS/NRB})\right\rangle = 1$, the existence of a scaling factor α will alter the mean. So, one can measure this mean and normalize I_{pc} by this value. On the other hand, the mean can have a frequency dependence due to ϵ_{err}. Using numerical means, though, one can find a slowly varying centerline and normalize the phase-corrected spectrum, thus removing α and ϵ_{err} in one step. Finally, the rescaled and phase-corrected spectrum $I_{pc,sc}$ may be calculated as:

$$I_{pc,sc} = \frac{I_{pc}(\omega)}{Re\{Ipc(\omega)\}} = \frac{|\tilde{\chi}^{(3)}|}{|\tilde{\chi}^{(3)}_{NR}|}e^{i\phi_{CARS/NRB}} \tag{4.22}$$

In conclusion, the Kramers-Kroning algorithm allows removing the NRB from the raw spectrum even with a measurement of a reference NRB spectra and extrapolating the pure vibrational information.

4.2.3. Directional Denoising Using Fourier Spectrum Cloning

At this point the white noise has been dealt with using singular value decomposition and the overall spectrum profile of each pixel has been adjusted removing the NRB contribution. However, the hyperspectral images still present a directional noise, mainly in the shape of horizontal or vertical stripes that can be seen in the whole image and especially in the background. In the top part of figure 4.6 we can see these stripes and how they get removed after the denoising algorithm is applied.
The stripes are typically caused by laser fluctuation or instrumental factors like the raster scanning detection employed during the image acquisition. To remove this kind of artefact a denoising method based on the Fourier Transform of the image is used.

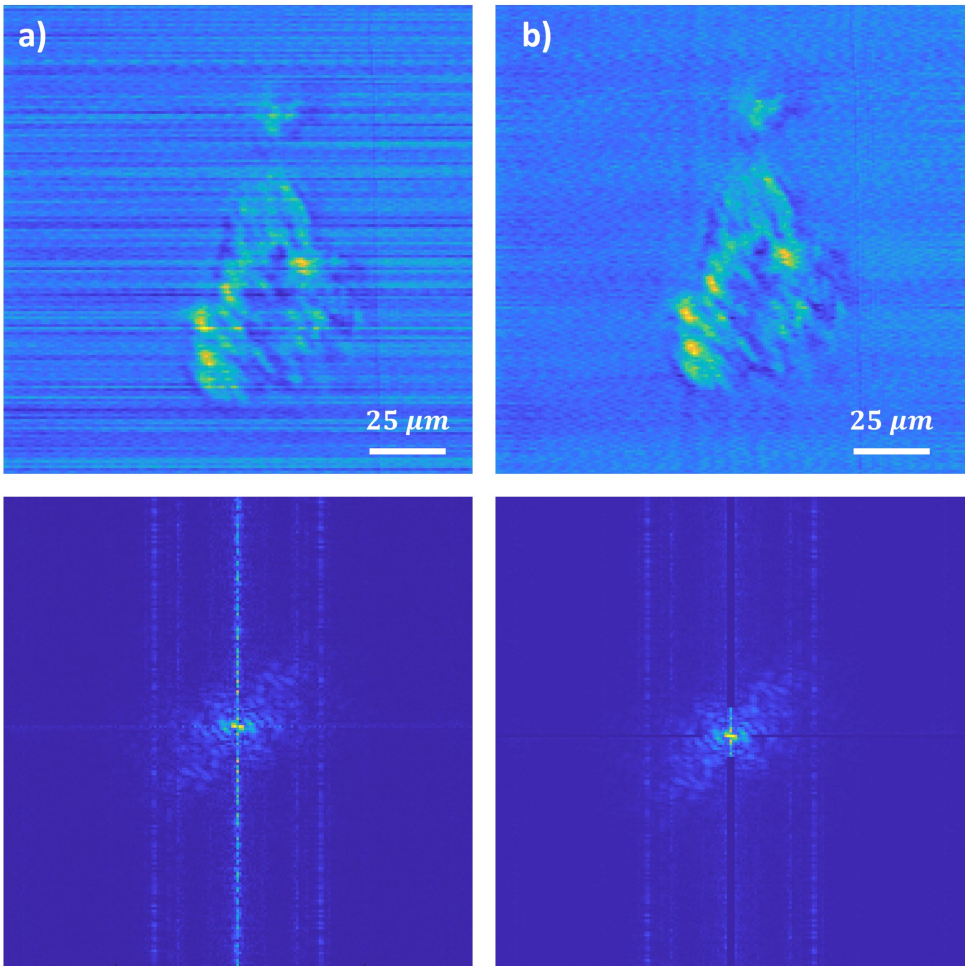

Figure 4.6: Example of directional denoising applied on integrated B-CARS data of spheroids before (a) and after (b) denoising. Under each B-CARS image the Fourier transform image can be seen. Note that in this case the masked region is put to zero to better highlight the masks, but usually we substitute the masked area with the mean of the adjacent pixels.

We developed a selective removal process to minimize this kind of noise while retaining the information about the sample. As we mentioned previously, the information about the sample is located at the centre of the Fourier-transformed image at each Raman shift, therefore it will be important to store $10\% - 30\%$ of the centre of the image before proceeding. The method then consists of masking specific regions in the Fourier space, typically a narrow vertical line or horizontal line, and substituting the values of the masked pixels with the mean values of the adjacent ones. In the bottom part of figure 4.6, we can see the images in the Fourier space and the masked areas. Note that the masked areas below image b) do not reach the centre of the image. Indeed after masking and before reconstructing the image we substitute the original $10\% - 30\%$ of data from the central area which was previously stored to avoid information loss.

4.2.4. Spectral Unmixing

After the denoising procedure described in the previous sections, we can proceed with the unmixing of chemical components of the heterogeneous sample. This process is particularly relevant for microscopic applications and indeed all the previous data processing had also the purpose of facilitating the identification of the different chemical components. Spectral unmixing in general works identifying distinct spectral features associated with the analytes under investigation and producing both a spectrum and an image for each component identified. Then it is up to the researchers to match the spectrum and morphological features in the sample to specific chemical components.

Going back to the unmixing procedure, there is not just one algorithm but several for different purposes and applications. For broadband CARS imaging specifically, we can classify the algorithms used into two categories. The first category is factorisation-based methods like the N-FINDR algorithm we already encountered, while the second is clustering algorithms such as K-MEANS analysis.

Factorization methods work by decomposing the hyperspectral dataset D into two simpler meaningful components, a matrix S for spectra and C for concentrations. This is done in a way such that $D = CS^* + \epsilon$, with ϵ representing the minimized error in the algorithm's iterative process. When dealing with factorization methods each pixel spectrum within an image can be conceptualized as a linear amalgamation of the spectral components identified by the algorithm. The coefficients of this linear amalgamation correspond to the concentrations of specific species present in the sample.
In practical terms when applying the N-FINDR algorithm to our hyperspectral matrixes, we decide how many species we expect to find, let's call this number N. Then the

algorithm will try to divide the image into N areas where each one has the same color but different brightness. Each area has also an associated spectrum, which is a real spectrum found in the image that approximates the spectrum of the whole area. Note also that in this case if a pixel belongs to a group it is not precluded to belong to others too.

In contrast, clusterization methods like K-means work by identifying two or more groups of pixels with shared spectral attributes within hyperspectral images. Here the spectrum affiliated with a given cluster serves as a representative for all pixels within that cluster and it is an average of each pixel in that cluster not necessarily a real spectrum found in the image. Unlike before with clusterization pixels only belong to one group.
In practice when using factorization we can fine-tune the intensity threshold to better identify the components in the image while with clusterization we may need to identify more clusters to perform a similar fine-tuning.

In the subsequent sections, we will further explore these methods, including their underlying principles and mathematical formulations.

N-FINDR Algorithm

The N-FINDR algorithm [52] as briefly mentioned before, is a factorization method that allows us to reduce the dimensionality of the hyperspectral data by finding the combination of spectra, called endmembers, which best represents the whole image. In particular, if we call the dataset D and the matrix of spectra S, then we will also have a matrix of concentrations C such that $D = CS^* + \epsilon$, where ϵ is simply the error we would like to minimize in the iterative process.

The algorithm works by maximizing a quantity proportional to the determinant of an augmented endmember matrix (E), which is constructed by appending a row of ones and the endmembers themselves, defining the i-th endmember as e_i as follows:

$$E = \begin{bmatrix} 1 & 1 & \cdots & 1 \\ e_1 & e_2 & \cdots & e_m \end{bmatrix} \tag{4.23}$$

So the volume, $V(E)$, is defined as:

$$V(E) = \frac{1}{(m-1)!} \cdot |E| \tag{3.25}$$

where m is the number of endmembers.

The algorithm starts with a random set of vectors and proceeds by evaluating each pixel's likelihood of being a pure or nearly pure pixel. This evaluation consists of calculating the volume using each pixel as a replacement for each endmember. If the replacement results in an increase in volume, the pixel replaces the corresponding endmember. The process continues until no more replacements are found, resulting in the identification of the endmembers.

Once the endmembers are found, the spectra serve as the new basis for projecting the initial image using a non-negatively constrained least squares algorithm. This final step allows for the determination of abundance or concentration maps in the reduced dataset. In figure 4.7 we can appreciate the algorithm at work on images with and without directional denoising.

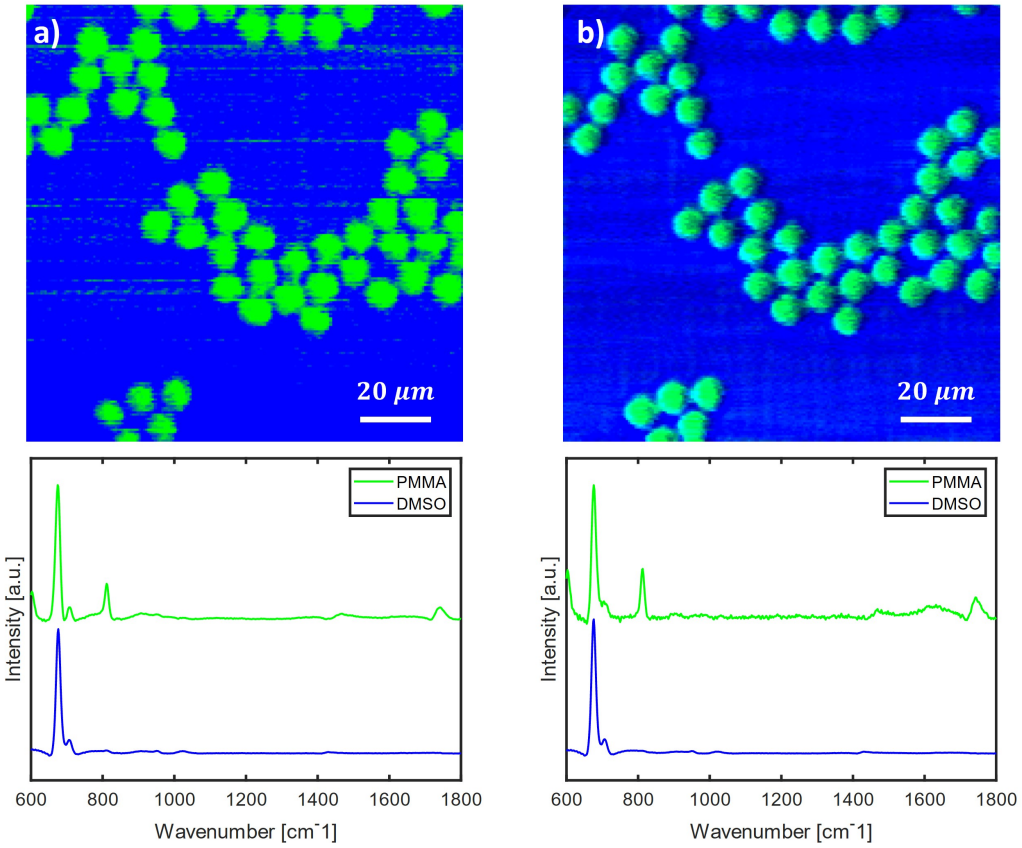

Figure 4.7: False colour image and spectrum achieved using N-FINDR algorithm applied to the B-CARS data with (b) and without (a) directional denoising. The image represents a test sample of polymethyl methacrylate (PMMA) in dimethyl sulfoxide (DMSO).

Going back to the previous section we can notice how the directional denoising improves the quality of the false-colour image as it did with the raw B-CARS data presented in figure 4.6, and how it does not alter the spectra identified by the N-FINDR algorithm.

K-MEANS Algorithm

K-means cluster analysis (KMCA) is a clusterization algorithm used for spectral unmixing. Clustering means partitioning the original dataset into k subsets called clusters [53] [54] where the number k of clusters is arbitrarily selected through an initial guess. The k-means algorithm, in particular, starts by randomly distributing the k-clusters. Then it assesses the distance of all spectra of the dataset to the mean cluster spectrum. Finally, it assigns each spectral trace to the cluster with the closest mean spectrum.

Note that iterating the previous steps provides optimized results [53]. The main goal of the KMCA is to minimize the distances between the data within each cluster and to maximize the distances between different clusters according to some well-defined distance metric. This way we aim to achieve both homogenous spectra in a given cluster but also meaningfully different clusters. The most employed clustering criterion for this purpose is the sum of the squared Euclidean distances between each instance x_i (a pixel spectrum) and the centroid m_J (cluster centre spectrum) of the subset. This distance is known as clustering error [54]

$$E(m_1, \ldots, m_k) = \sum_{i=1}^{N} \sum_{j=1}^{k} \left(I(x_i \in C_j) |x_i - m_j|^2 \right) \tag{4.24}$$

where C_j denotes the j-th cluster and I is a function whose value is 1 when the i-th instance belongs to the cluster C_j or 0 when such instance belongs to another cluster.

In figure 4.8 we can see the algorithm applied to the same starting image used in figure 4.7 b) for the N-FINDR algorithm. Note how with k-means in this case we analyzed the image twice to achieve similar performance to N-FINDR and we saw that trying to find three components instead of two better isolate the beads from the background.

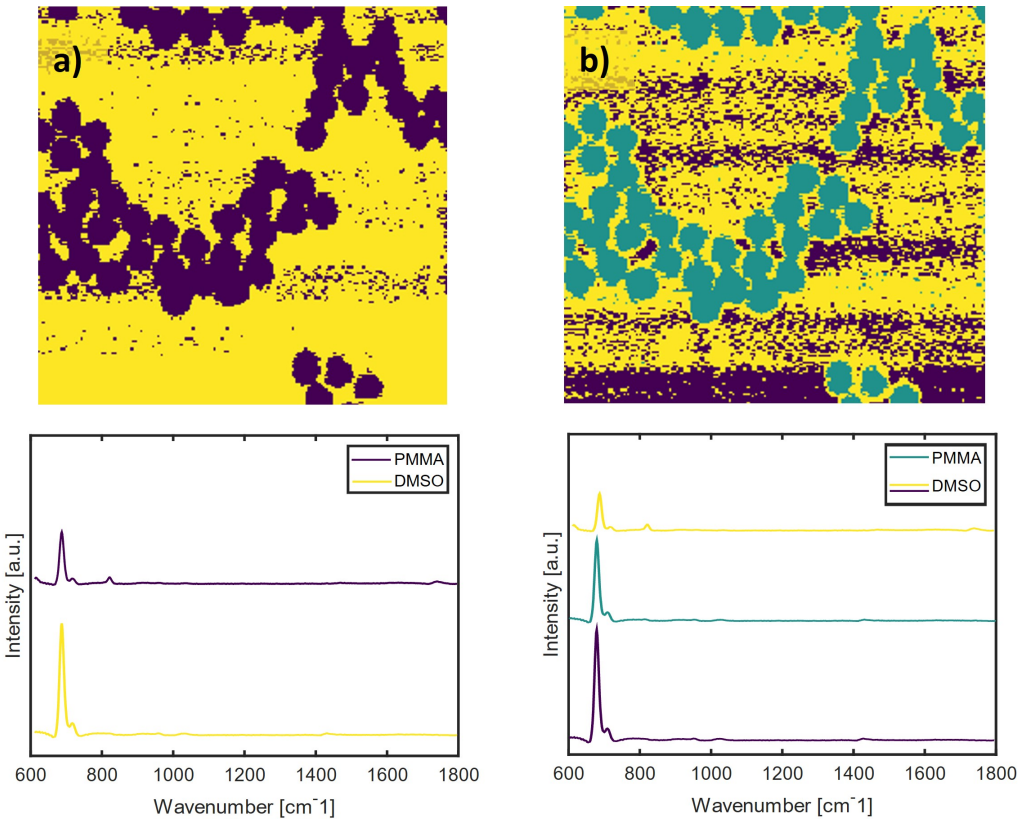

Figure 4.8: False colour image and spectra found using K-means algorithm applied to the B-CARS (with directional denoising) trying to find two (a) or three (b) components. The images represent the same test sample of polymethyl methacrylate (PMMA) in dimethyl sulfoxide (DMSO) analyzed in 4.7.

5 | Experiments and Results

In the following chapter, we will illustrate the various experiments and results obtained using B-CARS microscopy, SHG and 3PEF microscopy, and time-delay CARS spectroscopy.

5.1. Broadband CARS Microscopy on test samples

To evaluate the performance of the system and further develop the procedure for processing data, I needed to acquire hyperspectral images of a test sample. The chosen sample was a mixture of $8\mu m$ polymethylmethacrylate (PMMA) and $10\mu m$ polystyrene beads immersed in dimethyl sulfoxide (DMSO) and sandwiched between two $170\mu m$ coverslips.

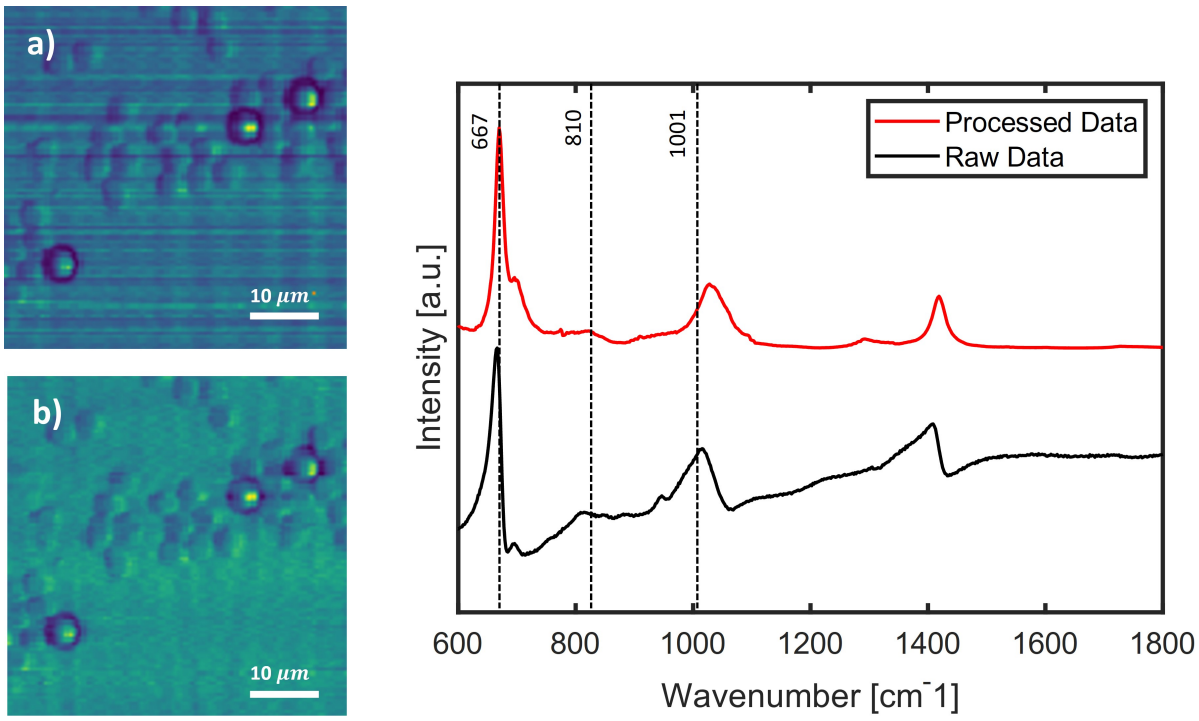

Figure 5.1: 2-color B-CARS integrated image before (a) and after (b) the denoising procedure and mean spectrum in the fingerprint region before and after the denoising procedure with highlighted relevant Raman shifts for the chemical composition of the sample. The image was acquired with 1 ms integration time and $1\mu m$ pixel size.

Figure 5.1 a) shows the raw B-CARS image integrated over all the Raman shifts where we can already distinguish each component of the sample. Before proceeding with the denoising though, we can also check the mean spectrum for the presence of peaks at specific Raman shifts to see if we can already distinguish some expected peaks specific to species present in the sample. As we can see from the spectrum reported in the same figure, even before denoising and removing the NRB, we can already see the peak of DMSO at $667cm^{-1}$ and of PS at $1001cm^{/1}$. We expect to see a peak around $810cm^{-1}$ too for PMMA, but at this stage, it is not as clearly visible as the others.

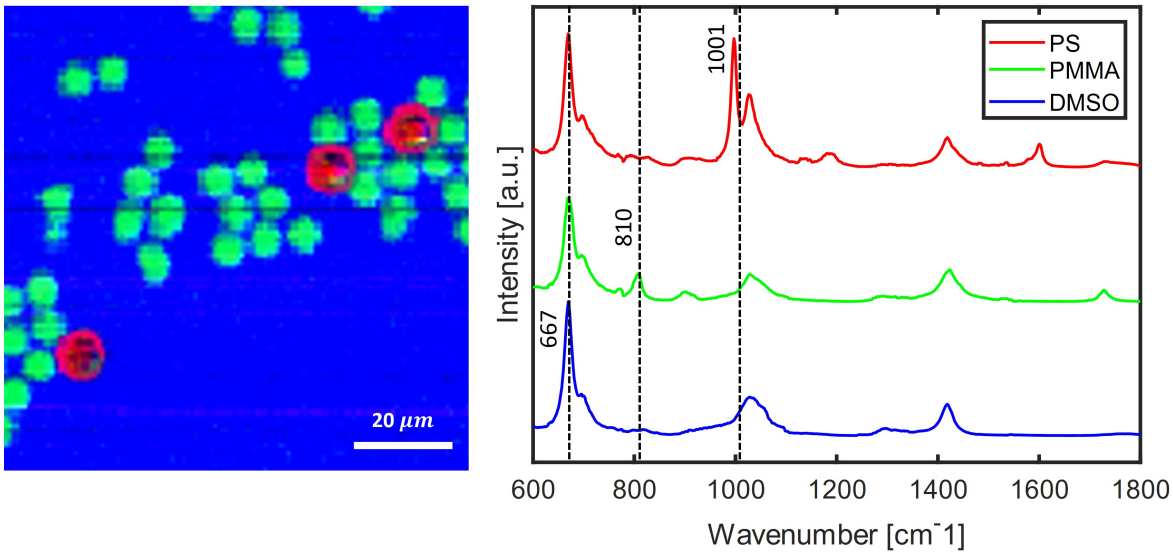

Figure 5.2: 2 colour B-CARS spectrum of the two different chemical species after NRB removal acquired with 1ms integration time.

After white noise reduction with singular value decomposition (SVD), NRB removal with the Kramers-Kronig algorithm, and directional denoising using Fourier spectrum cloning, we proceeded with the spectral unmixing. We used the N-FINDR algorithm to distinguish the chemical constituents, and in figure 5.2 we saw the reconstructed false-color image that successfully identified the different components. We can also further check our results by looking at the spectrum identified by the spectral unmixing algorithm for each endmember in the same figure. Unlike before with the mean spectrum, now each one of the relevant peaks can be clearly distinguished. Note however how the DMSO signal is present for all endmembers. This behaviour is to be expected as the beads are immersed in DMSO and then sandwiched between glass coverslips, therefore their signal will be always partially mixed with the one from the solvent. The image indeed allows us to confirm that the endmembers identified are indeed DMSO, PS and PMMA.

5.2. Spheroids Imaging and 3D Sectoning

In this section, we will continue to show the system capabilities using spheroids instead of the simpler test samples studied before. Spheroids in biology, are three-dimensional cell models that mimic the characteristics of cell aggregates such as microtumors. They are formed by culturing cells in a non-adherent environment, which allows them to aggregate and form a spherical shape [55]. They are used to identify cancer therapeutics and study cell behaviour in a three-dimensional environment. Spheroids importance in biological studies resides in the capability to mimic tumour behaviour more effectively than regular two-dimensional cell cultures [56] because they contain both surface-exposed and deeply buried cells resulting in a hypoxic centre with a well-oxygenated outer layer of cells.

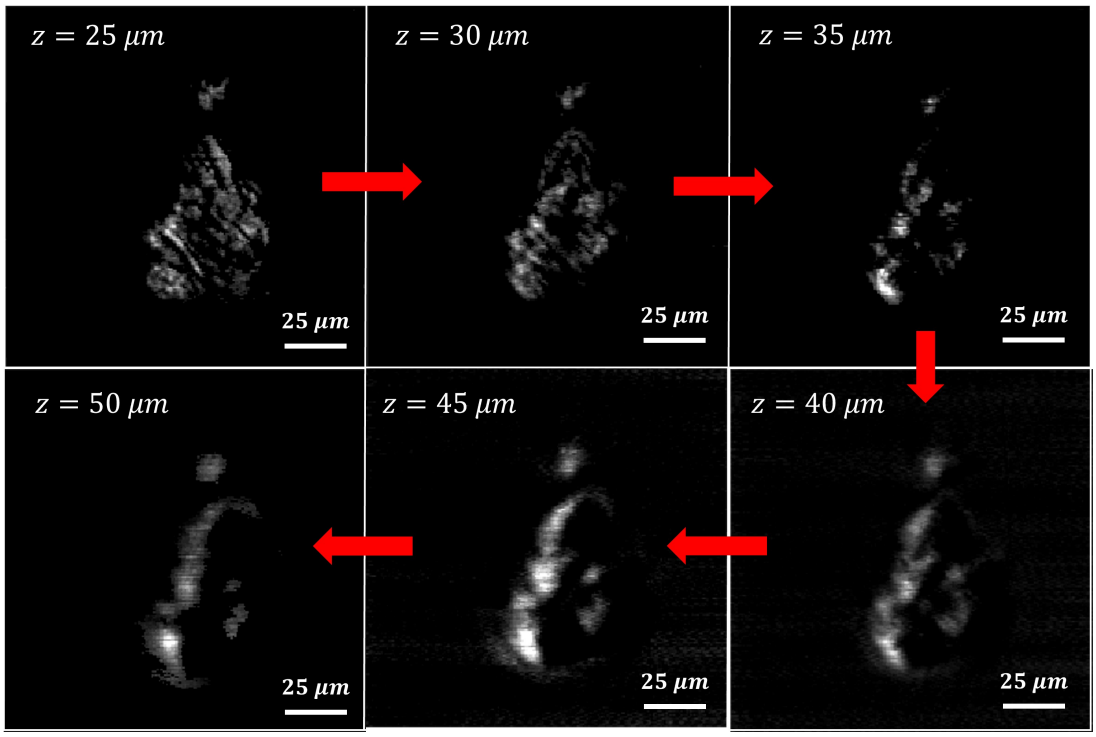

Figure 5.3: B-CARS data of TPC1 spheroids after denoising procedure with monochrome colourmap. Images are $100\mu m$ with $500nm$ pixel size, $1ms$ pixel exposure time and $5\mu m$ z-step.

Our purpose is dual, on one side we want to assess if we can study these structures and accurately individuate different chemical species, while on the other we want to test the 3D sectioning capabilities of CARS microscopy. CARS indeed, like all CRS techniques, provide intrinsic 3D sectioning capabilities without the need for a confocal aperture. This technique is ideal for studying spheroids as they are 3D structures and developing it could be even more relevant for the study of organoids or other complex 3D structures.

Organoids indeed are more complex structures compared to spheroids, they are three-dimensional stem cell structures that organize into *ex vivo* mini organs. They are key to overcoming the challenge of ethically studying *in vivo* human organs [57]. it is clear at this point why it is relevant to develop a reliable technique able to gather information about the chemical and morphological structure of these samples in three dimensions.

In our studies on spheroids, we focused on distinguishing the main constituents to have a simple and reliable parameter to monitor on different focal planes. The constituents also needed to be in precise areas of the sample in order to test the 3d sectioning, so we chose to monitor the lipid-rich cytoplasm which should be in the outer layers of the spheroids and the protein-rich nuclei which should be in the inner layers. We started with measures on one focal plane and then we took successive images at adjacent focal planes distant $5\mu m$. The acquired hyperspectral images were then processed using the denoising procedure described in chapter 4.

To assess the 3d sectioning capabilities of CARS we can start by looking at the B-CARS data after the denoising procedure but before any spectral unmixing. From figure 5.3 indeed, we can already guess that what we are imaging are indeed different focal planes. To confirm this intuition we can proceed by analyzing the images produced after the spectral unmixing.

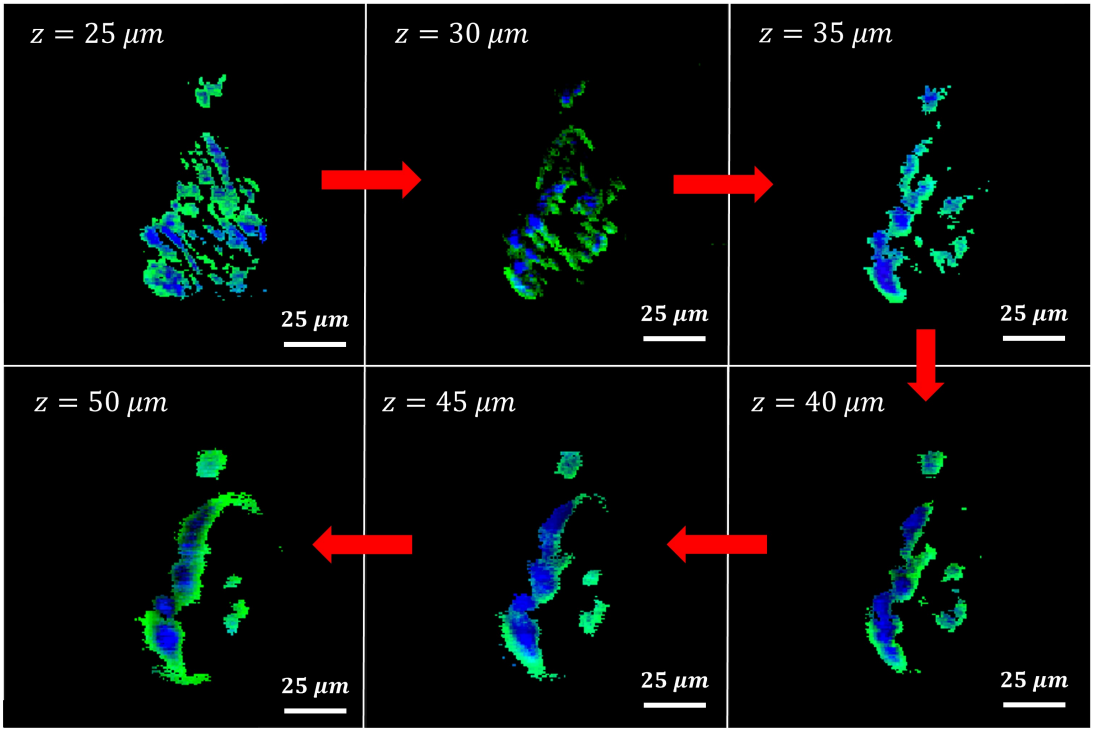

Figure 5.4: False colour image obtained with N-FINDR at different focal planes.

In figure 5.4 we can see the false colour image obtained using the N-FINDR algorithm. The green endmember consistently highlights the outside of the spheroid while the blue one is the inside. Therefore we would expect the blue endmember to be mainly proteic as the nuclei compared to the green one which should represent the cytoplasm.

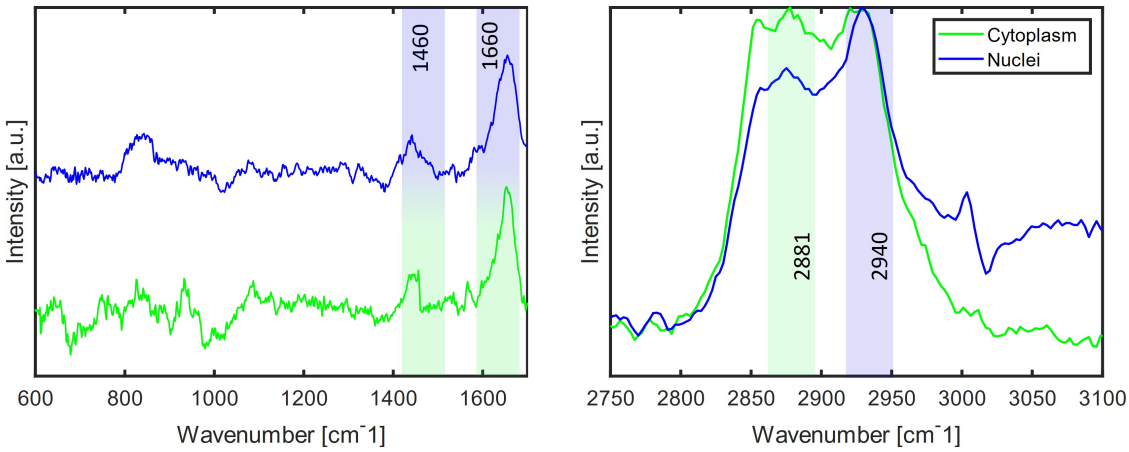

Figure 5.5: False colour image obtained with N-FINDR at different focal planes.

Looking at the spectrum identified by each endmember 5.5 we can notice indeed that the green endmember presents a peak typical of lipids in the CH-stretching region at $2881cm^{-1}$ while the blue endmember presents a peak typical of proteins at $2940cm^{-1}$. However this last peak as well as other protein peaks of the fingerprint region are also present in the green endmember, for example, the amide I and amide III peaks around $1660cm^{-}1$ and $1440cm^{-1}$ respectively.

Since the spectrum from the two endmembers presents many similarities we performed one last analysis to confirm our hypothesis. We plotted the ratio A/B between the two peaks identified in the CH region as they are the most intense peaks that identify the chemical species we want to distinguish. A is the peak at $2881cm^{-1}$ and B is the peak at $2940cm^{-1}$. We also used a double-colour intensity map with colours for minimum and maximum intensity matching the colours of the endmembers identified with N-FINDR. This method will ensure that we obtain images almost equivalent to the ones found with N-FINDR if and only if the two endmembers really represent cytoplasm and nuclei. The results can be seen in figure 5.6 from which we can confirm that the N-FINDR algorithm identified cytoplasm and nuclei in different focal planes.

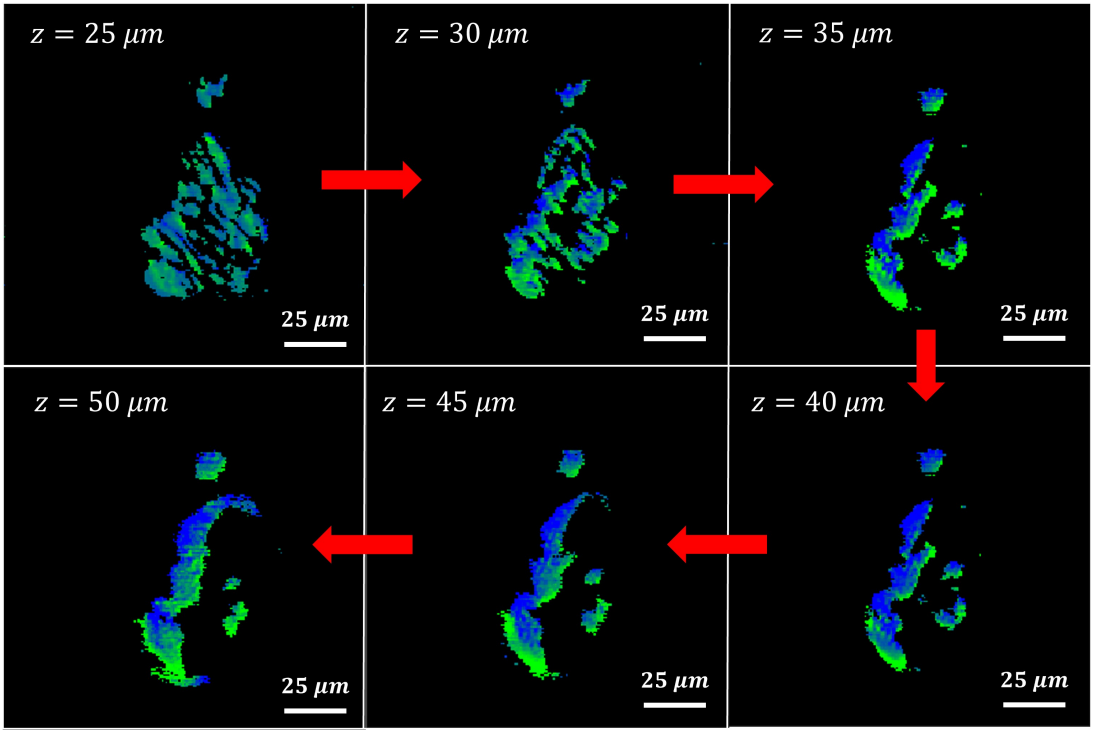

Figure 5.6: Dual colour CARS image of the ratio between peaks A ($2881cm^{-1}$) and B $2940cm^{-1}$.

5.3. CARS and SHG for Microcalcifications

In this section, we will introduce other microscopy techniques that can complement the information we get from B-CARS. We will mainly delve into second harmonic generation microscopy (SHG) but we will also talk about three photo excited fluorescence (3PEF). Both techniques can provide additional information about the sample while still being label-free. Fusing different detection methods therefore will provide a substantial advantage allowing us to retrieve more precise and comprehensive insight about the morphology and chemical properties of the samples.

The samples used for this study were breast tissue containing microcalcifications, as they are complex samples that can take full advantage of the new techniques. Microcalcifications are minuscule mineral deposits, primarily composed of calcium phosphate crystals, that form within breast tissue due to various biological processes [58]. These processes include normal benign phenomena like cellular turnover, which occurs naturally with ageing, but not only. Microcalcifications can also originate from inflammation, such as in instances where the breast tissue has been impacted by an infection or injury. In particular, certain benign breast conditions like fibroadenomas or cysts can result in the formation of microcalcifications. Therefore microcalcifications can be used as an early

indicator of breast cancer. Indeed when abnormal cells, including cancer cells, proliferate within breast tissue, they can trigger the accumulation of calcium in the surrounding tissue, leading to the formation of microcalcifications. Therefore, the detection of microcalcifications is pivotal in the screening and diagnosis of breast cancer.

Normally the primary imaging method to detect them is mammography [59] which generates detailed images of the breast tissue. However, even when doctors can identify abnormal deposits using mammography additional testing may be necessary to discern benign from malign tumors.

Recently B-CARS microscopy was identified as one possible method to perform further assessments and help achieve more accurate diagnosis [60]. B-CARS indeed can quickly produce high-resolution hyperspectral images of biological tissues without the need for labels and without damaging the samples. Therefore, B-CARS microscopy can be employed to detect and characterize microcalcifications in breast tissue with high precision and sensitivity, and it may potentially enhance the early detection and diagnosis of breast cancer.

On the other hand, B-CARS do not provide all the relevant information about the sample. For example, it does not detect anisotropy in tissues, which is relevant as tissues like collagen present strongly anisotropic structures. Second harmonic generation (SHG) microscopy on the other hand is capable of detecting this kind of filamentous structures which are also present in breast tissue and could enhance the image contrast. This shows how multimodal microscopy could provide a significant advantage compared to broadband CARS alone.

5.3.1. Preliminary Results with SHG

The first approach we developed was the most straightforward and cost-effective to evaluate the viability of this technique. We simply took consecutive measurements in the same area of the sample modifying the central wavelength of the spectrometer's grating to detect first B-CARS (central wavelength at $885nm$) and then SHG signals (central wavelength at $500nm$). Note however that since the two measures are not taken simultaneously this method will be significantly slower and the two images produced will not be exactly in the same position due to the finite accuracy of the translational stage.

As anticipated we used this approach on breast tissue containing microcalcifications, specifically samples sandwiched between two $170\mu m$ coverslips. The images produced were of $400\mu m^2$ with $8ms$ and $15ms$ integration times respectively for the two measures. The B-CARS data that satisfied our initial quality assessment was then post-processed

and analyzed using the procedure described in chapter 4. In particular, the spectral unmixing procedure for this kind of sample consisted of two steps. The first step required the k-means algorithm to identify the foreground and substrate as reported in figure 5.7, while the second exploited the N-FINDR algorithm applied to the foreground alone to identify the different chemical species.

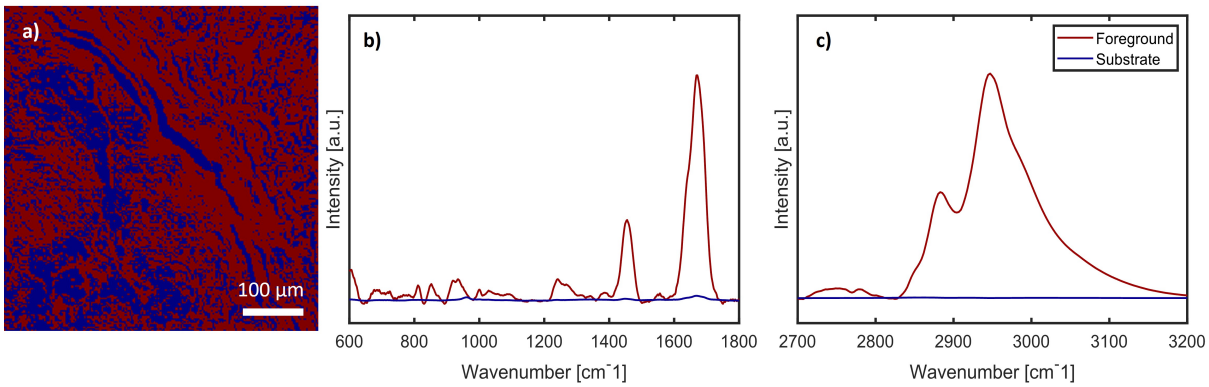

Figure 5.7: Substrate identification image obtained with k-means algorithm (a) and foreground and substrate associated spectrum in the fingerprint region (b) and CH region (c) for the B-CARS signal.

Once the foreground has been identified we can concentrate on the N-FINDR algorithm to identify different chemical species in the sample. For these preliminary measures in particular we didn't focus on the microcalcifications yet but on more macroscopic signals and in validating the SHG measures. Indeed we were able to identify collagen through the SHG signal and confirm our guess using the B-CARS signal from the red endmember.

However, before looking at the false colour image we need to study the identified endmembers spectra reported in figure 5.8 in the fingerprint and CH-stretching regions.

The most prominent signals in the fingerprint region for both spectra are two peaks. The first is around $1660cm^{-1}$ and it is characteristic of the Amide I band in proteins, while the second is around $1460cm^{-1}$ still from proteins but related to CH_2 and CH_3 in plane bendings [61]. As we said previously these are signals present in both spectra so we can use their ratio to determine which endmember can be classified as protein-rich, the red endmember. Then we can confirm this hypothesis by looking at the CH-stretching region where only the red endmember presents a peak around $2940cm^{-1}$ related to CH_3 in-plane bending of proteins and amino acids [61].

For the green endmember instead, we already saw previously that it shows signals typical of proteins but less so compared to other endmember. However, it also contains peaks around $1350cm^{-1}$ in the fingerprint region and around $2853cm^{-1}$ in the CH-stretching

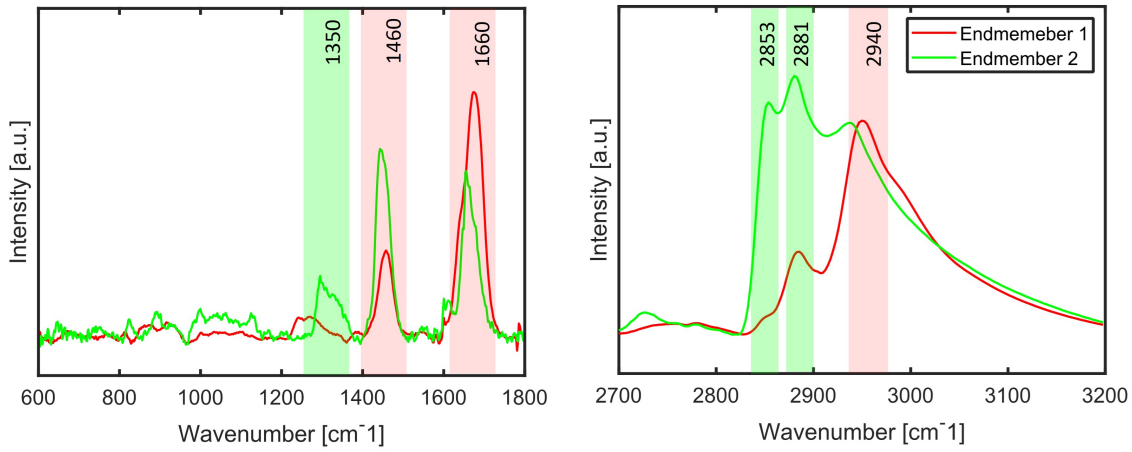

Figure 5.8: Enmembers spectra from fingerprint (left) and CH-stretching (right) regions. Highlighted are peaks associated with proteins or lipids that allow us to interpret the red endmember as protein-rich and the green endmember as lipid-rich. The image corresponding to these endmembers can be found in figure 5.9.

region. Both are characteristic peaks of lipids, the first being due to in-plane twist vibrations and the second one due to CH_2 symmetric stretch of lipids. This second endmember then can be classified as lipid-rich when compared to the other.

Until now we identified the two endmembers as protein-rich and lipid-rich, it is worth mentioning though, that collagen is a protein but we didn't identify any major collagen-specific peaks. However, if we include weaker signals, we can see some collagen peaks around $1270cm^{-1}$ (Amide III) and $858cm^{-1}$ (C-C stretch). Therefore it is reasonable to assume that we would expect the protein-rich endmember to be localized mostly in the same area as the collagen identified by the SHG signal. Indeed if we look at the components of the false colour image and at the reconstructed image in figure 5.9 we can see exactly how the red protein-rich endmember and the blu SHG signal highlight the same area, showing that the multichannel detection worked as expected.

5.3.2. In-Depth Analysis of Microcalcifications

Once the general study was completed we focused on microcalcifications as they are not only relevant for diagnostic purposes but also more difficult to identify. We wanted to see if we could distinguish these tiny mineral deposits from the tissue underneath. Since microcalcifications aren't present everywhere in samples this time we also needed to take multiple brightfield (BF) images to locate them, in BF indeed microcalcifications appear darker due to the reduced transmission as we can see in figure 5.10. The BCARS images

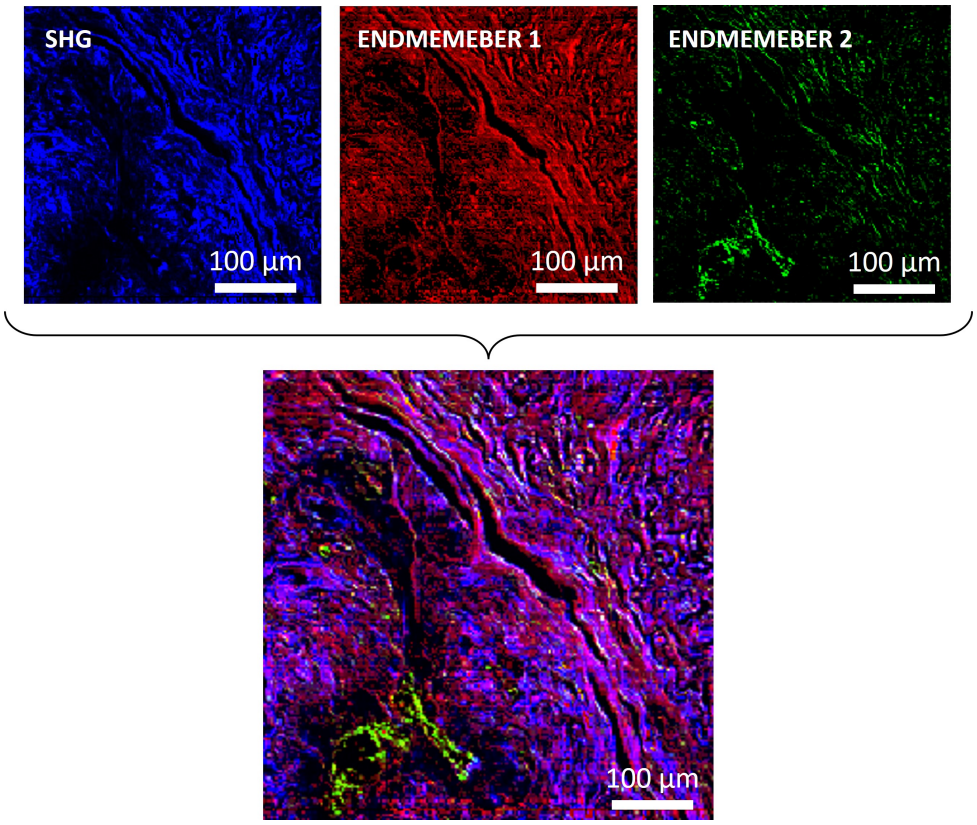

Figure 5.9: False colour image reconstructed from SHG image and from the endmembers images shown above. The endmembers spectra can be found in figure 5.8.

this time were acquired with a $16ms$ integration time to improve the signal-to-noise ratio and with $2\mu m$ pixel size to image an area of $400 \times 400\mu m$. Once the microcalcifications were found we could proceed with the same method used before to acquire the B-CARS signal, process it and produce the false colour image. In figure 5.10 we can see also one of the first false colour images produced. As anticipated here the N-FINDR algorithm was used mainly to distinguish between tissue (red endmember) and microcalcification (green endmember) and the results seemed promising comparing them to the BF image.

Inspecting the spectrum of each endmember revealed that the tissue was identified well, indeed we can see the peaks mentioned before related to proteins as highlighted in figure 5.11. However, the green endmember (representing microcalcifications) fluctuated too much to identify the typical peak at $960cm^{-1}$ that is associated in the literature [62] with the hydroxyapatite found in microcalcifications.

This unexpected behaviour could be explained by how microcalcifications transmit light and how the unmixing algorithms work. Microcalcifications are thicker than the adjacent tissue therefore transmit less light which results in a higher signal-to-noise ratio, for this

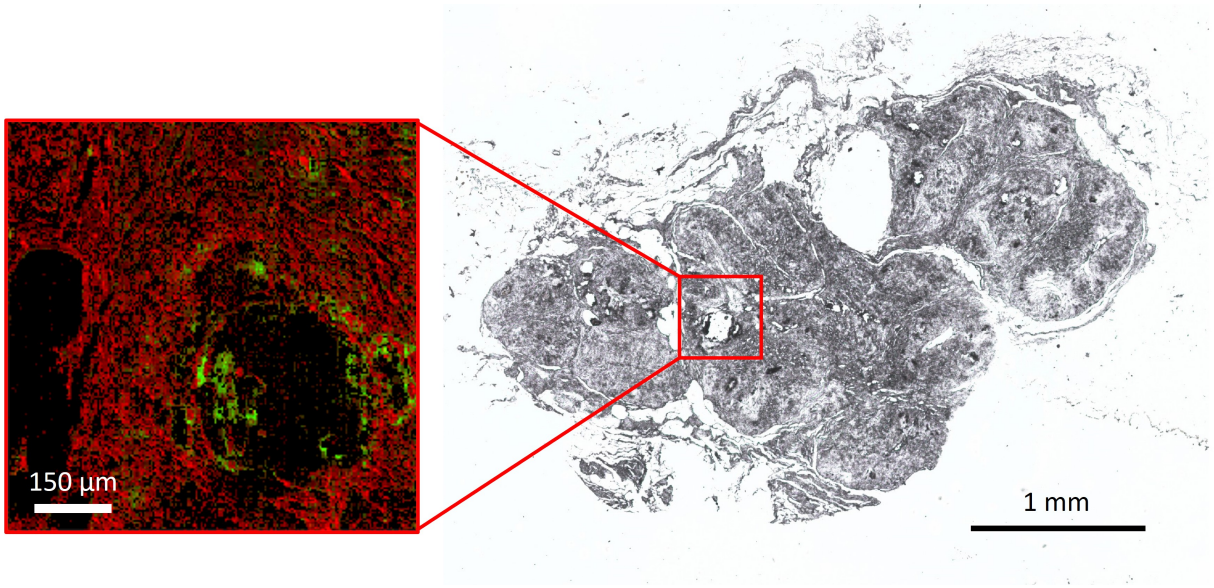

Figure 5.10: Brightfield Image of the whole sample and false colour image of the area of interest presenting microcalcifications.

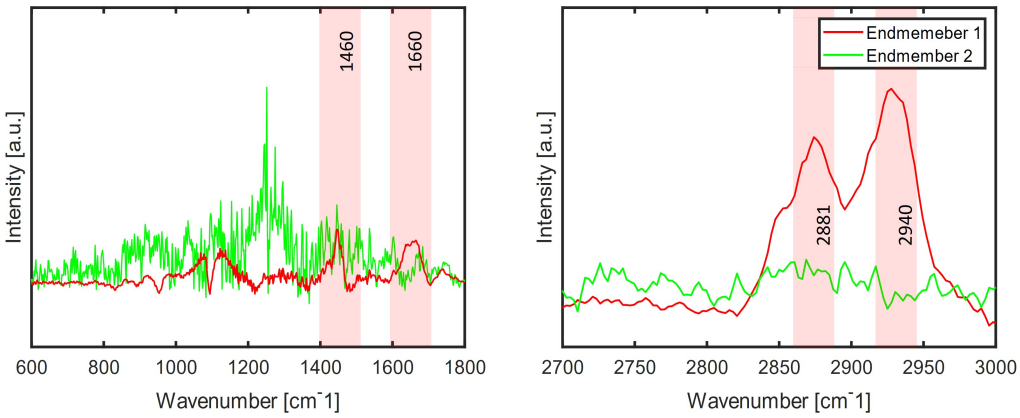

Figure 5.11: Endmemebers spectrum of the false colour image 5.10

reason, the unmixing algorithm was still able to identify them not because they presented a specific peak in the spectrum but because they presented a lower signal than the rest of the sample.

A possible solution we explored for this problem was focusing, during the fine-tuning procedure, directly on a microcalcification. Indeed not only do they transmit less light but they are also thicker than the adjacent tissue and may be on a different focal plane. The resulting image can be seen in figure 5.12 where we can see that this time we were able indeed to see a peak around $960cm^{-1}$.

Further studies could focus on 3D sectioning applied to microcalcifications to confirm if

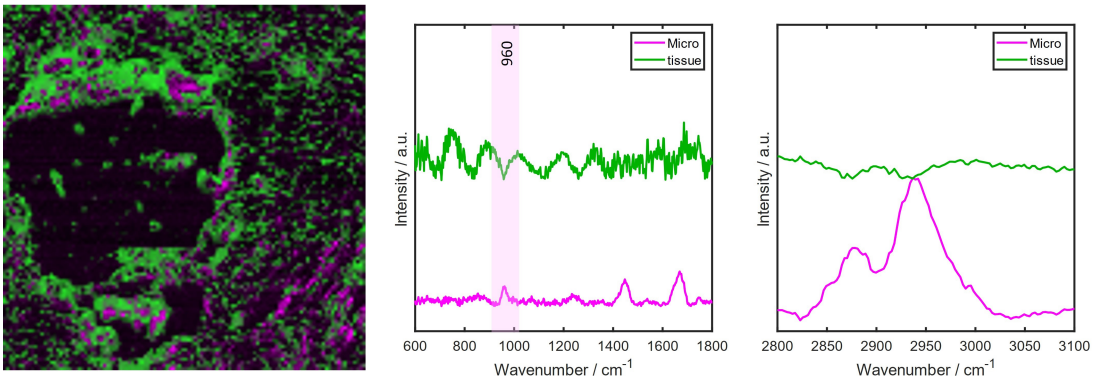

Figure 5.12: False colour image and related spectra obtained after focusing directly on the microcalcification. This image is taken in the same position as 5.11 on an adjacent slice with the same integration time and pixel size. Note the peak at $960cm^{-1}$ associated to hydroxyapatite

they are on a different focal plane compared to the tissue. If so then multiple focal planes can be used to reconstruct the final false-colour image.

5.3.3. Further Developments

After the initial successful measurements, we further developed the acquisition technique to overcome the limitations mentioned at the beginning of the section. We installed a photomultiplier tube (PMT) to acquire the signals simultaneously. Therefore multi-channel measurements can last just as long as single-channel measurements lasted before. Furthermore, the two images are now colocalized, so we can compare the spectrum of the two pixel by pixel. With this configuration, the SHG signal is measured by filtering light not needed for the B-CARS image. However, by using different filters we can explore also other multiphoton techniques such as three-photon excited fluorescence (3PEF).

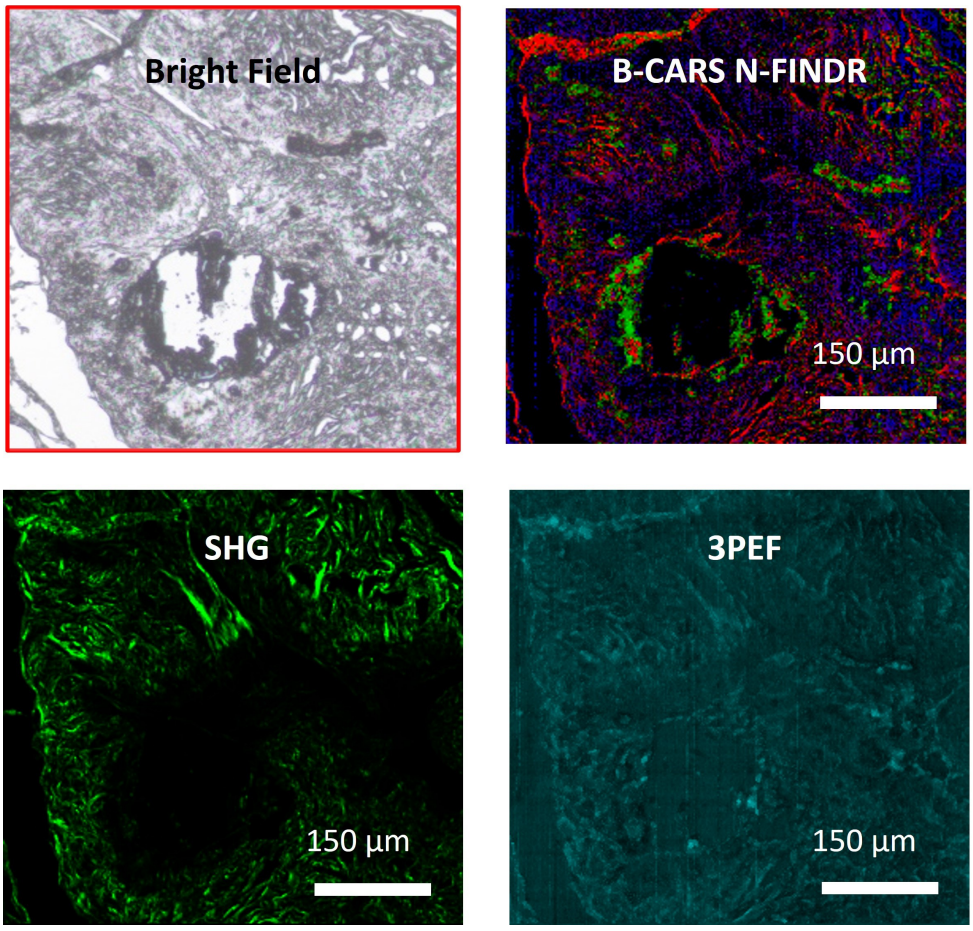

Figure 5.13: Set of images taken with different techniques in the same position as the sample shown in figure 5.12. Note that 3PEF only detect the tissue but not the micro-calcifications as the metabolic cofactors NADH and FAD are only present in cells.

3PEF is a relevant technique in biological imaging as it can effectively monitor nicotinamide adenine dinucleotide plus hydrogen (NADH) and flavine adenine dinucleotide (FAD) thanks to their intrinsic fluorescence [63]. NADH and FAD are relevant chemi-

cal species to monitor as they are metabolic cofactors that can be used to indicate the metabolic state of living tissues [64]. Since NADH and FAD are especially abundant in the mitochondria which are present in all human cells, we could expect the 3PEF image to only identify the tissue and not the calcifications. In figure 5.13 we can see indeed, that comparing the 3PEF signal with the bright field, B-CARS and SHG, the 3PEF identifies the tissue only.
This information can also be used as further proof that the green endmember identified in this B-CARS image is not tissue but microcalcifications. Note however, that in this case the B-CARS signal from the tissue was identified by two endmembers presenting similar signals to what we already saw previously while the microcalcifications were identified due to the reduced transmission.
This experiment evidence even more the potential of multichannel detection not only in conjunction with SHG but also with other multiphoton techniques. Indeed in future studies thanks to this configuration, we could continue to measure the bulk of our information using B-CARS complementing it with different techniques such as SHG or 3PEF.

5.4. Time-Delayed CARS on Crystals

Until now we mainly focused on B-CARS application to microscopy, they aren't however the only possible measure with this setup. In the following section, we will show some results achieved through time delay CARS on crystals.
By examining the spectrum at different time delays we were able to investigate the time dependences of both resonant and NRB components. We focused in particular on glass to investigate the pure non-resonant signal, on diamond to investigate a material with only one distinct sp^3 peak and finally on KTP (potassium titanyl phosphate) to investigate a more complex material with several peaks.

NRB Time Constants: Glass

We used glass due to the absence of specific peaks to retrieve the time constant of pure NRB. We performed a time sweep with $0.33ps$ steps and $1ms$ integration time. This measure will be important later as if the NRB time constants vary for different Raman shifts we could expect similar variations in the time constants of the crystal peaks.

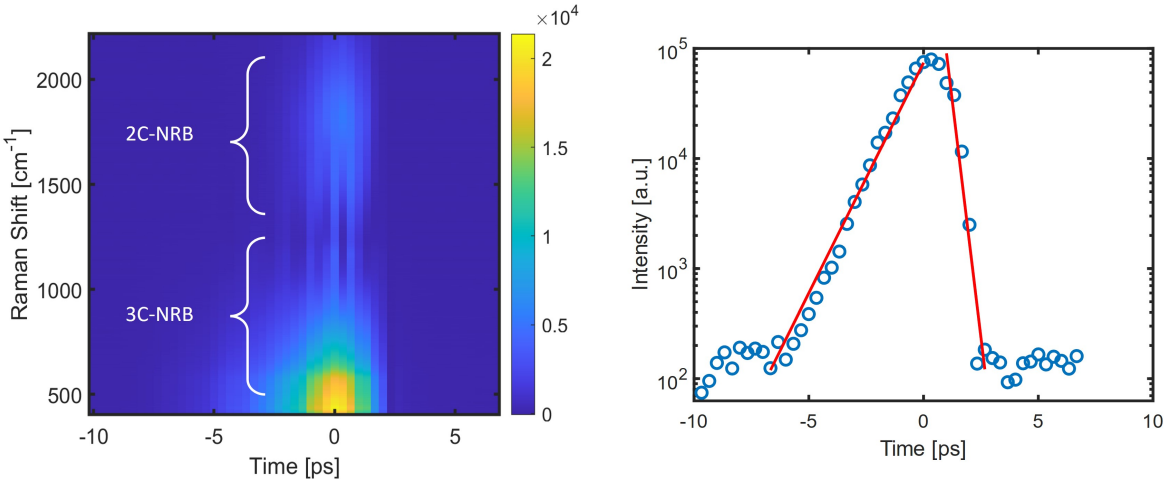

Figure 5.14: left) TD-CARS behaviour of the NRB measured on glass at 1ms integration time, 0.33ps steps, linear scale [a.u.]. right) fitting example around $500cm^{-1}$

The initial result is shown on the left part of figure 5.14 where we can notice the absence of specific peaks, as expected, as well as two distinct intensity regions for 3Color-NRB $< 1300cm^{-1}$ and 2Color-NRB at $1300 - 2500cm^{-1}$. As these two regions do not present any specific peaks, we will not only calculate the time constants for one Raman shift but we will repeat the fitting shown on the right part of figure 5.14 for all Raman shifts.

The result from all the fittings can be seen in figure 5.15. Here we can notice that the

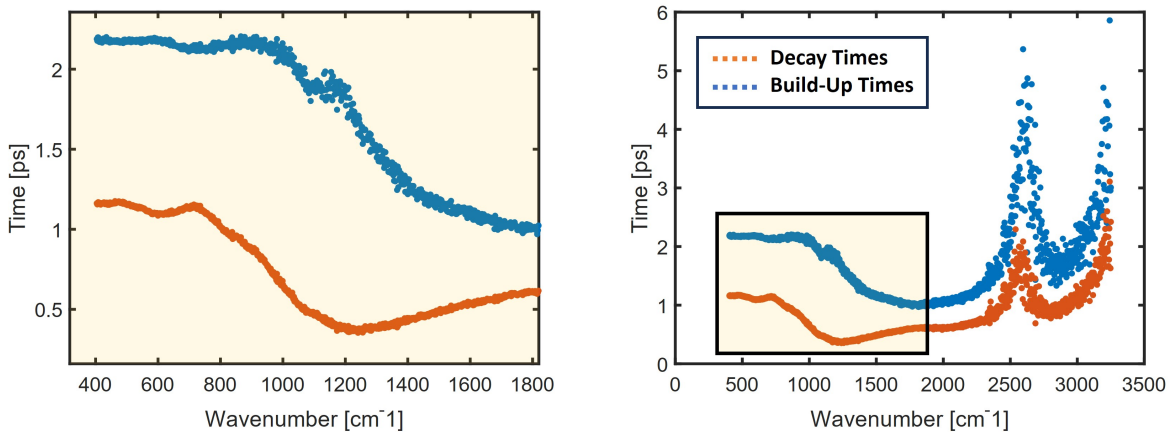

Figure 5.15: Build up and decay time constants for every Raman shift in glass with enlargement of the area of interest for KTP peaks.

decays are consistently faster than the build-ups which is consistent with the previous image that shows a clear difference between the two fitted slopes. We also notice that the time constants vary significantly at different Raman shifts, but they remain more stable in the fingerprint region.

Resonant Decay: Diamond

Once the non-resonant decay was measured we started analyzing some resonant signals. The first and simplest sample is diamond as it should display only one distinct sp^3 peak centred at $1336cm^-1$ as depicted in figure 5.16

For the NRB the sample presents the same behaviour already seen previously, with similar build-up and decay times of $1.06ps$ and $0.48ps$ respectively. Indeed, these results are in line with what was found for the NRB alone with the glass sample, as shown in figure 5.15 looking at the wavenumber around $1336cm^{-1}$. Diamond however presents also another decay due to the presence of the sp^3 peak which is measurable even for $\Delta t > 10ps$. So to reconstruct the diamond phonon's lifetime we can wait until the NRB signal is completely decayed (around $\Delta t = 4ps$) to obtain an NRB-free measurement. For the region after $4ps$ then, the sp^3 peak can be fitted using an exponential decay function:

$$I(\Delta t) = I_0 e^{-2\Delta t/T_{2\nu}} \tag{5.1}$$

Where $I(\Delta t)$ represents the measured intensity for any time delay Δt, I_0 represents the maximum intensity of the second decay region we just identified after $4ps$ and $T_{2\nu}$ represents the dephasing time of the vibrational coherence, which contains contributions from

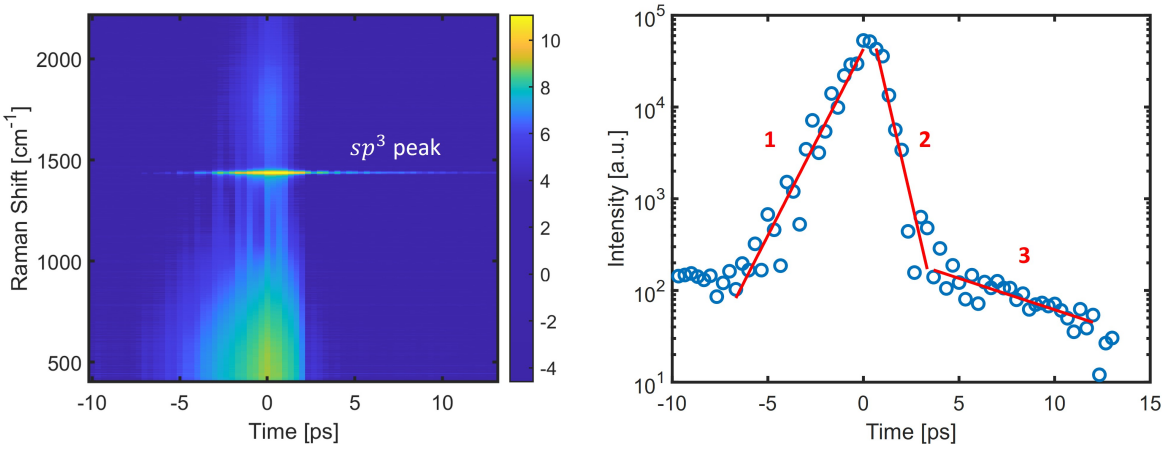

Figure 5.16: left) TD-CARS behaviour of diamond where it is evident the presence of a peak, with 0.33 ps steps, 1ms integration time and log intensity scale in [a.u.]. Right) Fitted exponential at $1336cm^{-1}$ showing both build-up (1) and double decay (2 and 3) of the NRB and sp^3 peak.

the vibrational population decay and the dephasing of the vibrational modes.

Our fitting of the signal at $1336cm^{-}1$ results in $T_{2\nu} = 6.33ps$ which is close to the expected phonon lifetimes found in the literature which range from $5.6ps$ to $6.0ps$ [65–67].

Complex Crystal: KTP

After proving that the TD-CARS measures were valid measuring both NRB and resonant signal decays we moved to a more complex sample to further validate the method. The sample chosen was KTP which, unlike diamond, presents several peaks as shown in figure 5.17

Even if these peaks are not as prominent as the one in diamond, they are still distinguishable as bright lines in figure 5.17 with $500ms$ integration time and averaging over 100 spectra. Therefore we performed the same exponential fitting mentioned before for each of these peaks. From the fittings, we found the usual $T_{2\nu}$ for build-up and decay of the NRB which shows that the procedure is consistent, as well as values for $T_{2\nu}$ of the resonant peaks with values ranging from $2.34ps$ to $6.54ps$ as presented in table 5.1. This variation can be attributed to specific properties of the sample as well as the effect induced by the experimental setup.

The results are also coherent with the ones found for pure NRB in glass and are consistent within an order of magnitude with the reported lifetimes from literature [68]. Regarding the difference between these reported lifetimes and our results, it is important to note that

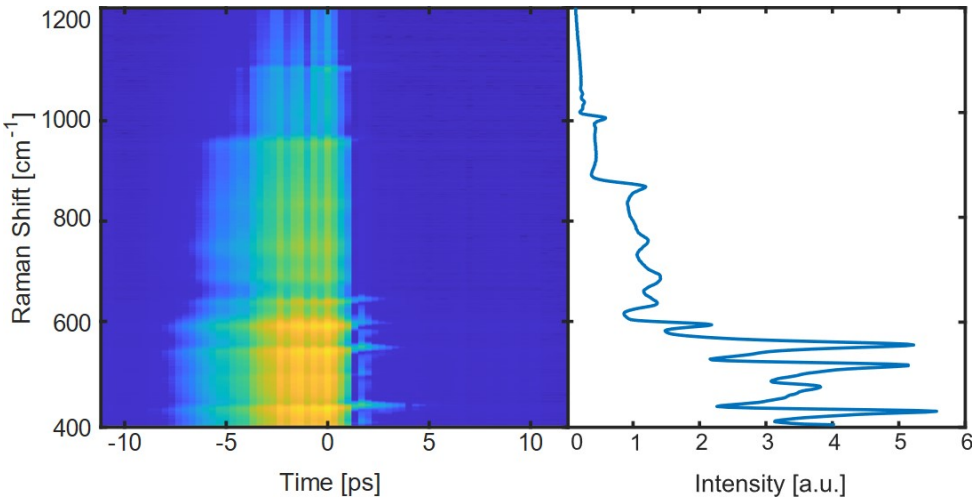

Figure 5.17: left) TD-CARS behaviour of KTP where we notice the presence of multiple peaks, with 0.33ps steps, 1ms integration time and log intensity scale in [a.u.]. Right) Spectrum at zero time delay to better distinguish the different peaks.

Raman Shift (cm^{-1})	**NRB Build-Up (ps)**	**NRB-Decay (ps)**	**Reported Peak-Decay (ps)**	**Measured Peak-Decay (ps)**
469	1.63	0.94		6.54
496	1.61	0.51		2.91
544	1.61	0.79	(1.95 ∓ 0.05)	4.96
583	1.62	0.59		2.87
614	1.57	0.74		2.34
655	1.63	0.52		5.86
680	1.66	0.49	(0.475 ∓ 0.004)	6.11
824	1.66	0.40	(1.64 ∓ 0.06)	6.71
917	1.71	0.36		7.01
104	1.62	0.76	(2.15 ∓ 0.07)	3.01

Table 5.1: Build-Up and Decay of NRB and resonant peaks calculated at the most relevant Raman shifts for KTP

the experimental setups used are different. In reported results were obtained from single-frequency measurements with $150fs$ pulses, allowing for a higher temporal resolution compared to the $3.8ps$ pump pulses utilized here. On the other hand, our setup allows for simultaneous measurement of the whole spectral range.

A further development of this study could consider for example how the presence and abundance of defects affect lifetimes, exploring if higher purity samples show extended lifetimes and thus larger dephasing times.

6 | Conclusions and Future Developments

The focus of this master thesis has been dual, further developing the experimental setup and at the same time exploring numerous applications of broadband coherent anti-Stokes Raman scattering. B-CARS indeed has demonstrated to be a powerful technique capable of going beyond the shortcomings of other more affirmed microscopy methods. I indeed tested how the system can reveal the chemical composition of a sample without the need for long preparations with markers that can also alter the results. Not only can we save time avoiding the preparation necessary with markers but we can also capture each spectrum more rapidly compared to other label-free techniques such as Spontaneous Raman. CARS, unlike SR, can also be used to image sections of a sample due to its 3D sectioning capabilities. These advantages make CARS a particularly promising tool for biomedical imaging and to complement this technique we choose to explore other label-free techniques that allow for fast imaging and could be used in parallel. Indeed we added a second channel to the setup, mainly exploring the integration of CARS and SHG and briefly of 3PEF. These techniques are ideal for our implementation because they require similar exposure times as CARS, allowing for parallel detection. They are also specialized in detecting specific features of biological samples that cannot be detected with CARS. For example, CARS does not provide information about the anisotropy of biological structures but SHG does.

The thesis started in Chapter 1 with an introduction to the most promising and affirmed techniques for biological imaging and their strength and weaknesses. This naturally led to the introduction of vibrational microscopy techniques and a brief overview of their capabilities and advantages.
In chapter 2 therefore I focused on these techniques to further understand the physical processes regulating them and how to overcome their limitations for imaging applications. This led to studying B-CARS in-depth as it was the best tool for high-speed vibrational imaging.
In chapter 3 I presented the experimental setup that used this technique. I divided the

setup into three main parts according to their different purposes. The first part is dedicated to pulse generation where the light from the laser beam is split into two paths to generate the narrowband pump pulses and the broadband Stokes pulses and accurately overlap them. The second part is the microscope where the overlapped pulses are focused onto the sample moved by a stage for raster scanning acquisition. Finally, the third part comprehends the detection system which saw the major changes during my thesis. In addition to the existing CCD camera, I added a PMT as a second channel and a DAQ to handle the signals and enable concurrent acquisition from both channels.
In Chapter 4 I went through the acquisition procedure which consisted mainly of calibration, denoising and spectral unmixing. I focused in particular on the denoising procedure whose purpose initially was just removing the NRB using a Kramers-Kronig algorithm. I added a singular value decomposition denoising before the NRB to remove the white noise too, and a directional denoising algorithm after the Kramers-Kronig to remove artefacts coming from laser fluctuations.
Finally, in Chapter 5 I showcased the experimental results obtained demonstrating the system's capabilities. I started with simple measurements of test samples made of plastic beads (PMMA and PS) immersed in a solvent (DMSO) which are especially good for testing imaging and spectroscopic capabilities. Then I moved on to more complex measures using biological samples. The first experiment aimed to test the 3D sectioning capabilities of B-CARS on spheroids and I was able to distinguish cytoplasm and nuclei at different focal planes every $5\mu m$. I first identified the two components using spectral unmixing algorithms and then I checked the results plotting just the ratio between two relevant peaks of each pixel confirming the previous result. Then I moved on to study breast tissue containing microcalcifications which I used initially to test second harmonic generation in conjunction with CARS before implementing the second channel for simultaneous acquisition. Once I saw that the results were promising I implemented and tested the PMT as a second channel and tested it with SHG and 3PEF measurements. For these second measurements we also focused on microcalcifications and the results were as expected. CARS distinguished the tissue from the microcalcifications using the characteristic peak of hydroxyapatite which is present in the calcifications. SHG identified the collagen which was rightfully located where CARS identified protein-rich tissue. 3PEF finally highlighted everything except the calcifications as the metabolic cofactors identified by this technique are only present in cells. The two added techniques therefore worked well to complement CARS and confirm our diagnosis. After the biological experiments, I also wanted to show how CARS is not only suitable for bio applications and imaging, so I performed some spectroscopy time-delay measurements on Glass, Diamond and KTP. This experiment aimed to retrieve the decay times of resonant peaks in solid-state materials fitting the

signal behaviour at different Raman shifts. I used glass to take a preliminary measure of the build-up and decay of the NRB alone which then was consistent throughout the other experiments. Then I used Diamond and KTP to measure a simple and more complex material using the same technique and obtaining results in line with reported lifetimes in the literature.

In conclusion, CARS has been demonstrated to be a powerful technique for biomedical imaging and cancer research, providing a label-free and non-invasive way to probe the molecular details of living tissues. CARS technology is constantly improving and becoming more widely adopted, making it a vital tool for biomedical researchers and clinicians, who can gain a deeper insight into biological processes and disease mechanisms. Looking into the future many exciting paths can be followed, one could be to focus on the capabilities of the setup and further improve it. For example, to achieve even faster imaging speeds line scanning or wide-field illumination could be implemented and to gain more information multichannel detection could be further explored. Another path could pursue the addition of user-friendly features designed to simplify the operation of the setup and increase reliability for the potential commercialization of the instrument that will make CARS accessible and applicable in clinical settings where it can be used to identify and characterize tumours and other complex biological structures.

Bibliography

[1] James Pawley. *Handbook of biological confocal microscopy*, volume 236. Springer Science & Business Media, 2006.

[2] Roger Y Tsien. The green fluorescent protein. *Annual review of biochemistry*, 67(1): 509–544, 1998.

[3] AP Alivisatos. Semiconductor nanocrystals as fluorescent biological labels. In *Abstracts of Papers of the American Chemical Society*, volume 218, pages U296–U296. AMER CHEMICAL SOC 1155 16TH ST, NW, WASHINGTON, DC 20036 USA, 1999.

[4] Kevin M Dean and Amy E Palmer. Advances in fluorescence labeling strategies for dynamic cellular imaging. *Nature chemical biology*, 10(7):512–523, 2014.

[5] Lu Wei, Zhixing Chen, Lixue Shi, Rong Long, Andrew V Anzalone, Luyuan Zhang, Fanghao Hu, Rafael Yuste, Virginia W Cornish, and Wei Min. Super-multiplex vibrational imaging. *Nature*, 544(7651):465–470, 2017.

[6] Thomas Niehörster, Anna Löschberger, Ingo Gregor, Benedikt Krämer, Hans-Jürgen Rahn, Matthias Patting, Felix Koberling, Jörg Enderlein, and Markus Sauer. Multi-target spectrally resolved fluorescence lifetime imaging microscopy. *Nature methods*, 13(3):257–262, 2016.

[7] Rohit Bhargava. Infrared spectroscopic imaging: the next generation. *Applied spectroscopy*, 66(10):1091–1120, 2012.

[8] Mahmoud Ghomi. *Applications of Raman spectroscopy to biology: from basic studies to disease diagnosis*, volume 5. IOS press, 2012.

[9] GJ Puppels, FFM De Mul, Cornelis Otto, J Greve, M Robert-Nicoud, DJ Arndt-Jovin, and TM Jovin. Studying single living cells and chromosomes by confocal raman microspectroscopy. *Nature*, 347(6290):301–303, 1990.

[10] Paola Piredda, Manuel Berning, Petra Boukamp, and Andreas Volkmer. Subcellular raman microspectroscopy imaging of nucleic acids and tryptophan for distinction of

normal human skin cells and tumorigenic keratinocytes. *Analytical chemistry*, 87 (13):6778–6785, 2015.

[11] U Neugebauer, Thomas Bocklitz, JH Clement, C Krafft, and J Popp. Towards detection and identification of circulating tumour cells using raman spectroscopy. *Analyst*, 135(12):3178–3182, 2010.

[12] Conor L Evans and X Sunney Xie. Coherent anti-stokes raman scattering microscopy: chemical imaging for biology and medicine. *Annu. Rev. Anal. Chem.*, 1:883–909, 2008.

[13] Ji-Xin Cheng and Xiaoliang Sunney Xie. *Coherent Raman scattering microscopy*. CRC press, 2016.

[14] GL Eesley. Coherent raman spectroscopy. *Journal of Quantitative Spectroscopy and Radiative Transfer*, 22(6):507–576, 1979.

[15] Theodore H Maiman et al. Stimulated optical radiation in ruby. 1960.

[16] Yanping Li, Binglin Shen, Shaowei Li, Yihua Zhao, Junle Qu, and Liwei Liu. Review of stimulated raman scattering microscopy techniques and applications in the biosciences. *Advanced Biology*, 5(1):2000184, 2021.

[17] Christian W Freudiger, Wei Min, Brian G Saar, Sijia Lu, Gary R Holtom, Chengwei He, Jason C Tsai, Jing X Kang, and X Sunney Xie. Label-free biomedical imaging with high sensitivity by stimulated raman scattering microscopy. *Science*, 322(5909): 1857–1861, 2008.

[18] Evelyn Ploetz, Stefan Laimgruber, Stefan Berner, Wolfgang Zinth, and Peter Gilch. Femtosecond stimulated raman microscopy. *Applied Physics B*, 87:389–393, 2007.

[19] P Nandakumar, A Kovalev, and A Volkmer. Vibrational imaging based on stimulated raman scattering microscopy. *New journal of physics*, 11(3):033026, 2009.

[20] Kazuki Hashimoto, Megumi Takahashi, Takuro Ideguchi, and Keisuke Goda. Broadband coherent raman spectroscopy running at 24,000 spectra per second. *Scientific reports*, 6(1):21036, 2016.

[21] Michael D Duncan, J Reintjes, and TJ Manuccia. Scanning coherent anti-stokes raman microscope. *Optics letters*, 7(8):350–352, 1982.

[22] Andreas Zumbusch, Gary R Holtom, and X Sunney Xie. Three-dimensional vibrational imaging by coherent anti-stokes raman scattering. *Physical review letters*, 82 (20):4142, 1999.

[23] Renzo Vanna, Alejandro De la Cadena, Benedetta Talone, Cristian Manzoni, Marco Marangoni, Dario Polli, and Giulio Cerullo. Vibrational imaging for label-free cancer diagnosis and classification. *La Rivista del Nuovo Cimento*, 45(2):107–187, 2022.

[24] Ji-Xin Cheng, Wei Min, Yasuyuki Ozeki, and Dario Polli. *Stimulated Raman scattering microscopy: Techniques and applications*. Elsevier, 2021.

[25] Hervé Rigneault. Coherent raman scattering processes. In *Stimulated Raman Scattering Microscopy*, pages 3–20. Elsevier, 2022.

[26] Robert W Boyd. Wave-equation description of nonlinear optical interactions. *Nonlinear optics*, pages 69–133, 2008.

[27] Ji-Xin Cheng, Lewis D Book, and X Sunney Xie. Polarization coherent anti-stokes raman scattering microscopy. *Optics letters*, 26(17):1341–1343, 2001.

[28] Paul J Wrzesinski, Hans U Stauffer, Waruna D Kulatilaka, James R Gord, and Sukesh Roy. Time-resolved femtosecond cars from 10 to 50 bar: collisional sensitivity. *Journal of Raman Spectroscopy*, 44(10):1344–1348, 2013.

[29] Andreas Volkmer, Lewis D Book, and X Sunney Xie. Time-resolved coherent anti-stokes raman scattering microscopy: Imaging based on raman free induction decay. *Applied Physics Letters*, 80(9):1505–1507, 2002.

[30] Miu Tamamitsu, Yusuke Sakaki, Tasuku Nakamura, G Krishna Podagatlapalli, Takuro Ideguchi, and Keisuke Goda. Ultrafast broadband fourier-transform cars spectroscopy at 50,000 spectra/s enabled by a scanning fourier-domain delay line. *Vibrational Spectroscopy*, 91:163–169, 2017.

[31] Marcus T Cicerone, Khaled A Aamer, Young Jong Lee, and Erik Vartiainen. Maximum entropy and time-domain kramers–kronig phase retrieval approaches are functionally equivalent for cars microspectroscopy. *Journal of Raman Spectroscopy*, 43 (5):637–643, 2012.

[32] Erik M Vartiainen. Phase retrieval approach for coherent anti-stokes raman scattering spectrum analysis. *JOSA B*, 9(8):1209–1214, 1992.

[33] Carlo M Valensise, Alessandro Giuseppi, Federico Vernuccio, Alejandro De la Cadena, Giulio Cerullo, and Dario Polli. Removing non-resonant background from cars spectra via deep learning. *APL Photonics*, 5(6), 2020.

[34] Keisuke Isobe, Akira Suda, Masahiro Tanaka, Hiroshi Hashimoto, Fumihiko Kannari, Hiroyuki Kawano, Hideaki Mizuno, Atsushi Miyawaki, and Katsumi Midorikawa.

Single-pulse coherent anti-stokes raman scattering microscopy employing an octave spanning pulse. *Optics Express*, 17(14):11259–11266, 2009.

[35] Wolfgang Langbein, Israel Rocha-Mendoza, and Paola Borri. Single source coherent anti-stokes raman microspectroscopy using spectral focusing. *Applied Physics Letters*, 95(8), 2009.

[36] Tak W Kee and Marcus T Cicerone. Simple approach to one-laser, broadband coherent anti-stokes raman scattering microscopy. *Optics letters*, 29(23):2701–2703, 2004.

[37] Jingjiang Xu, Baoshan Guo, Kenneth KY Wong, and Kevin K Tsia. Broadband hyperspectral coherent anti-stokes raman scattering microscopy for stain-free histological imaging with principal component analysis. In *Multiphoton Microscopy in the Biomedical Sciences XIV*, volume 8948, pages 62–67. SPIE, 2014.

[38] Takuro Ideguchi, Simon Holzner, Birgitta Bernhardt, Guy Guelachvili, Nathalie Picqué, and Theodor W Hänsch. Coherent raman spectro-imaging with laser frequency combs. *Nature*, 502(7471):355–358, 2013.

[39] Charles H Camp Jr, Young Jong Lee, John M Heddleston, Christopher M Hartshorn, Angela R Hight Walker, Jeremy N Rich, Justin D Lathia, and Marcus T Cicerone. High-speed coherent raman fingerprint imaging of biological tissues. *Nature photonics*, 8(8):627–634, 2014.

[40] Jennifer P Ogilvie, Meng Cui, Dmitry Pestov, Alexei V Sokolov, and Marlan O Scully. Time-delayed coherent raman spectroscopy. *Molecular Physics*, 106(2-4): 587–594, 2008.

[41] Ji-Xin CHENG, Andreas VOLKMER, Lewis D BOOK, and X Sunney XIE. An epi-detected coherent anti-stokes raman scattering (e-cars) microscope with high spectral resolution and high sensitivity. *SPIE milestone series*, 175:105–108, 2003.

[42] Charles H Camp Jr, Young Jong Lee, and Marcus T Cicerone. Quantitative, comparable coherent anti-stokes raman scattering (cars) spectroscopy: correcting errors in phase retrieval. *Journal of Raman Spectroscopy*, 47(4):408–415, 2016.

[43] Francesco Masia, Adam Glen, Phil Stephens, Paola Borri, and Wolfgang Langbein. Quantitative chemical imaging and unsupervised analysis using hyperspectral coherent anti-stokes raman scattering microscopy. *Analytical Chemistry*, 85(22):10820–10828, 2013.

[44] Markku Makitalo and Alessandro Foi. Optimal inversion of the anscombe transforma-

tion in low-count poisson image denoising. *IEEE transactions on Image Processing*, 20(1):99–109, 2010.

[45] Charles H Camp Jr, John S Bender, and Young Jong Lee. Real-time and high-throughput raman signal extraction and processing in cars hyperspectral imaging. *Optics express*, 28(14):20422–20437, 2020.

[46] Young Jong Lee, Doyoung Moon, Kalman B Migler, and Marcus T Cicerone. Quantitative image analysis of broadband cars hyperspectral images of polymer blends. *Analytical chemistry*, 83(7):2733–2739, 2011.

[47] Yuexin Liu, Young Jong Lee, and Marcus T Cicerone. Broadband cars spectral phase retrieval using a time-domain kramers–kronig transform. *Optics letters*, 34(9): 1363–1365, 2009.

[48] Tommaso Baldacchini, Maxwell Zimmerley, Chun-Hung Kuo, Eric O Potma, and Ruben Zadoyan. Characterization of microstructures fabricated by two-photon polymerization using coherent anti-stokes raman scattering microscopy. *The Journal of Physical Chemistry B*, 113(38):12663–12668, 2009.

[49] Hilde A Rinia, Mischa Bonn, Michiel Müller, and Erik M Vartiainen. Quantitative cars spectroscopy using the maximum entropy method: the main lipid phase transition. *ChemPhysChem*, 8(2):279–287, 2007.

[50] Sapun H Parekh, Young Jong Lee, Khaled A Aamer, and Marcus T Cicerone. Label-free cellular imaging by broadband coherent anti-stokes raman scattering microscopy. *Biophysical journal*, 99(8):2695–2704, 2010.

[51] William M Tolles, Joseph W Nibler, JR McDonald, and Albert B Harvey. A review of the theory and application of coherent anti-stokes raman spectroscopy (cars). *Applied Spectroscopy*, 31(4):253–271, 1977.

[52] Michael E Winter. A proof of the n-findr algorithm for the automated detection of endmembers in a hyperspectral image. *Algorithms and Technologies for Multispectral, Hyperspectral, and Ultraspectral Imagery X*, 5425:31–41, 2004.

[53] Miloš Miljković, Tatyana Chernenko, Melissa J Romeo, Benjamin Bird, Christian Matthäus, and Max Diem. Label-free imaging of human cells: algorithms for image reconstruction of raman hyperspectral datasets. *Analyst*, 135(8):2002–2013, 2010.

[54] Ya-Juan Liu, Michelle Kyne, Cheng Wang, and Xi-Yong Yu. Data mining in raman imaging in a cellular biological system. *Computational and Structural Biotechnology Journal*, 18:2920–2930, 2020.

[55] Kamila Białkowska, Piotr Komorowski, Maria Bryszewska, and Katarzyna Miłowska. Spheroids as a type of three-dimensional cell cultures—examples of methods of preparation and the most important application. *International journal of molecular sciences*, 21(17):6225, 2020.

[56] Ilaria Giusti, Giuseppina Poppa, Sandra D'Ascenzo, Letizia Esposito, Anna Rita Vitale, Giuseppe Calvisi, and Vincenza Dolo. Cancer three-dimensional spheroids mimic in vivo tumor features, displaying "inner" extracellular vesicles and vasculogenic mimicry. *International Journal of Molecular Sciences*, 23(19):11782, 2022.

[57] Siqi Yang, Haijie Hu, Hengchung Kung, Ruiqi Zou, Yushi Dai, Yafei Hu, Tiantian Wang, Tianrun Lv, Jun Yu, and Fuyu Li. Organoids: The current status and biomedical applications. *MedComm*, 4(3):e274, 2023.

[58] Barbara S Monsees. Evaluation of breast microcalcifications. *Radiologic Clinics of North America*, 33(6):1109–1121, 1995.

[59] Woo Kyung Moon, Jung-Gi Im, Young Hwan Koh, Dong-Young Noh, and In Ae Park. Us of mammographically detected clustered microcalcifications. *Radiology*, 217(3):849–854, 2000.

[60] Georgi I Petrov, Rajan Arora, and Vladoslav V Yakovlev. Coherent anti-stokes raman scattering imaging of microcalcifications associated with breast cancer. *Analyst*, 146 (4):1253–1259, 2021.

[61] Felicia S Manciu, John D Ciubuc, Karla Parra, Marian Manciu, Kevin E Bennet, Paloma Valenzuela, Emma M Sundin, William G Durrer, Luis Reza, and Giulio Francia. Label-free raman imaging to monitor breast tumor signatures. *Technology in cancer research & treatment*, 16(4):461–469, 2017.

[62] Renzo Vanna, Carlo Morasso, Beatrice Marcinnò, Francesca Piccotti, Emanuele Torti, Davide Altamura, Sara Albasini, Manuela Agozzino, Laura Villani, Luca Sorrentino, et al. Raman spectroscopy reveals that biochemical composition of breast microcalcifications correlates with histopathologic features. *Cancer research*, 80(8): 1762–1772, 2020.

[63] M Skala and N Ramanujam. Multiphoton redox ratio imaging for metabolic monitoring in vivo advanced protocols in oxidative stress ii ed d armstrong, 2010.

[64] Melissa C Skala, Kristin M Riching, Annette Gendron-Fitzpatrick, Jens Eickhoff, Kevin W Eliceiri, John G White, and Nirmala Ramanujam. In vivo multiphoton microscopy of nadh and fad redox states, fluorescence lifetimes, and cellular mor-

phology in precancerous epithelia. *Proceedings of the National Academy of Sciences*, 104(49):19494–19499, 2007.

[65] Filomeno S de Aguiar Júnior, Marcelo F Santos, Carlos H Monken, and Ado Jorio. Lifetime and polarization for real and virtual correlated stokes-anti-stokes raman scattering in diamond. *Physical Review Research*, 2(1):013084, 2020.

[66] KC Lee, Benjamin J Sussman, J Nunn, VO Lorenz, K Reim, D Jaksch, IA Walmsley, P Spizzirri, and S Prawer. Comparing phonon dephasing lifetimes in diamond using transient coherent ultrafast phonon spectroscopy. *Diamond and related materials*, 19 (10):1289–1295, 2010.

[67] Kazutaka G Nakamura, Kazuma Ohya, Hiroshi Takahashi, Tetsuya Tsuruta, Hiroya Sasaki, Shin-ichi Uozumi, Katsura Norimatsu, Masahiro Kitajima, Yutaka Shikano, and Yosuke Kayanuma. Spectrally resolved detection in transient-reflectivity measurements of coherent optical phonons in diamond. *Physical Review B*, 94(2):024303, 2016.

[68] HAS Singhapurage, DM Senarathna, and F Ganikhanov. Decay of raman active vibrations within oxide groups of potassium titanyl phosphate. *Optical Materials*, 137:113526, 2023.

List of Figures